ANL-05/08

YUCCA Mountain Project

FY 2004 Annual Report for Waste Form Testing Activities

Chemical Engineering Division
Argonne National Laboratory

ARGONNE IS OPERATED BY THE UNIVERSITY OF CHICAGO FOR THE U.S. DEPARTMENT OF ENERGY OFFICE OF SCIENCE

About Argonne National Laboratory

Argonne is operated by The University of Chicago for the U.S. Department of Energy Office of Science, under contract W-31-109-Eng-38. The Laboratory's main facility is outside Chicago, at 9700 South Cass Avenue, Argonne, Illinois 60439. For information about Argonne and its pioneering science and technology programs, see www.anl.gov.

Availability of This Report

This report is available, at no cost, at http://www.osti.gov/bridge. It is also available on paper to U.S. Department of Energy and its contractors, for a processing fee, from:

U.S. Department of Energy
Office of Scientific and Technical Information
P.O. Box 62
Oak Ridge, TN 37831-0062
phone (865) 576-8401
fax (865) 576-5728
reports@adonis.osti.gov

ANL-05/08

Argonne National Laboratory
9700 S. Cass Ave.
Argonne, IL 60439

YUCCA MOUNTAIN PROJECT

FY 2004 Annual Report for Waste Form Testing Activities

by

W.L. Ebert, J.A. Fortner, R.J. Finch,
J.L. Jerden, Jr., and J.C. Cunnane

Chemical Engineering Division

March 2005

Conducted under
MPO No. B004210CM3X

INTENTIONALLY LEFT BLANK

CONTENTS

Page

Executive Summary xiii

INTRODUCTION (J. Cunnane) 1-1

2.0 EXAMINATION OF CORRODED CSNF (J. Fortner) 2-1
- 2.1 BACKGROUND 2-1
- 2.2 PROCEDURES 2-2
  - 2.2.1 Test Materials 2-2
  - 2.2.2 Solids Analysis Methods 2-2
- 2.3 RESULTS 2-4
  - 2.3.1 Alteration Phase Characteristics – Visible Light Microscopy 2-4
  - 2.3.2 SEM and TEM Results 2-5
  - 2.3.3 X-Ray Absorption Results 2-7
- 2.4 DISCUSSION 2-24
- 2.5 REFERENCES 2-24

3.0 DISSOLVED CONCENTRATION TESTING (J. Jerden and R. Finch) 3-1
- 3.1 BACKGROUND 3-1
- 3.2 PROCEDURES 3-8
  - 3.2.1 Data Analysis 3-9
  - 3.2.2 Accuracy and Precision 3-10
- 3.3 RESULTS 3-10
- 3.4 DISCUSSION 3-21
- 3.5 REFERENCES 3-22

4.0 HLW GLASS TESTING (W. Ebert) 4-1
- 4.1 BACKGROUND 4-1
  - 4.1.1 Tests with SRL 202U Glass at 40ºC 4-3
  - 4.1.2 Tests with Hanford-H Glass 4-4
- 4.2 PROCEDURES 4-4
  - 4.2.1 MCC-1 Static Leach Test Method 4-4
  - 4.2.2 Product Consistency Test Method 4-6
  - 4.2.3 Vapor Hydration Test Method 4-7
  - 4.2.4 SRL 202G and Hanford-H Glasses 4-9
  - 4.2.5 Leachant Solutions 4-10
- 4.3 RESULTS 4-11
  - 4.3.1 Results of MCC-1 Tests with SRL 202G Glass 4-11
  - 4.3.2 Results of MCC-1 Tests with Hanford-H Glass 4-14
  - 4.3.3 Results of Product Consistency Tests with Hanford-H Glass 4-16
  - 4.3.4 Results of Vapor Hydration Tests with Hanford-H Glass 4-16
  - 4.3.5 Results of Measured Layer Thickness for Standard VHTs and Excess-Water VHTs with Hanford-H Glass 4-16

CONTENTS
(Continued)

Page

4.3.6 Results of Solution Analyses for Excess-Water VHTs with Hanford-H Glass 4-18
4.4 DISCUSSION 4-33
4.4.1 Consistency of MCC-1 Tests with SRL 202G Glass with the pH and Temperature Dependencies in the Defense HLW Glass Degradation Model 4-33
4.4.2 Comparison of MCC-1 Tests Results with Hanford-H Glass with the pH and Temperature Dependence in the Defense HLW Glass Degradation Model 4-36
4.4.3 Dissolution of Hanford-H Glass in Brine Solutions 4-37
4.4.4 Comparison of PCT Results with Defense HLW Glass Degradation Model 4-37
4.4.5 Comparison of Excess-Water VHT Results with Temperature Dependence in the Defense HLW Glass Degradation Model 4-38
4.4.6 Summary of Test Results and Comparison with Defense HLW Glass Degradation Model 4-39
4.5 REFERENCES 4-43

5.0 DELIQUESCENCE ASSOCIATED WITH GLASS CORROSION (W. Ebert) 5-1
5.1 BACKGROUND 5-1
5.2 PROCEDURES 5-1
5.2.1 Isopiestic Test Method 5-1
5.2.2 Test Specimens 5-3
5.3 RESULTS 5-4
5.3.1 Results of Isopiestic Tests with PCT Solutions 5-4
5.3.2 Results of Isopiestic Tests with Evaporated PCT Salts 5-5
5.3.3 Results of Isopiestic Tests with Vapor-Hydrated Glasses 5-6
5.4 DISCUSSION 5-11
5.5 REFERENCES 5-12

ACKNOWLEDGEMENTS 5-13

FIGURES

Page

2-1a. ATM-103 Fuel Fragments from Vapor Test 2-13
2-1b. ATM-103 Fuel Fragments from Low Drip Rate Test 2-13
2-1c. ATM-103 Fuel Fragments from High Drip Rate Test 2-13
2-1d. ATM-106 Fuel Fragments from Vapor Test 2-13
2-1e. ATM-106 Fuel Fragments from Low Drip Rate Test 2-13
2-1f. ATM-106 Fuel Fragments from High Drip Rate Test 2-13
2-1g. ATM-109B Fuel Fragments from Vapor Test 2-14
2-1h. ATM-109A Fuel Fragments from Vapor Test 2-14
2-1i. ATM-109C Fuel Fragments from High Drip Rate Test 2-14
2-1j. ATM-109C Fuel Fragments from Vapor Test 2-14
2-1k. ATM-109C Fuel Fragments from High Drip Rate Test 2-14
2-2. Cross-Sectioned Fragment of ATM-103 Fuel Tested 10 Years under Low Drip Rate Conditions 2-15
2-3a. Detail of Cross-Sectioned Fragment of ATM-103 from Low Drip Rate Test of 10 Years 2-15
2-3b. Cross-Sectioned Fragments of ATM-106 from High Drip Rate Test of 10 Years 2-16
2-3c. Detail of Cross-Sectioned Fragment of ATM-106 from a High Drip Rate Test of 10 Years 2-15
2-4. SEM Micrograph of Material Taken from Test S62J-92 2-17
2-5. TEM Micrograph of Crystallites from the S62J-92 Sample 2-17
2-6. Electron Diffraction Patterns from Platy Uranium Phase from Test Sample S62J-92 2-18
2-7. TEM Micrograph of the Plutonium-Enriched Material with Epsilon Phase and Fuel Fragments 2-19
2.8. Image-filtered TEM Micrograph of the Field of View in Figure 2.7 2-19
2.9. Electron Energy Loss Spectrum Showing Plutonium and Americium Enrichment 2-20
2-10. Electron Energy Loss Spectrum Showing Presence of Molybdenum and Ruthenium from Epsilon Particles 2-20
2-11. Bent-Laue X-ray Energy Analyzer 2-20
2-12. Schematic of How a Bent-Laue Analyzer Functions 2-20
2-13. SEM Micrograph Showing Anomalous Clustering of Epsilon Particles on Surface of Pitted Fuel Grain and Acicular Uranyl Alteration Products from High Drip Rate Unsaturated Test of ATM-106 Sampled at 104 Months 2-21
2-14. Neptunium L_3 edge XAS from Unaltered ATM-103, without Background Correction 2-22
2-15. Plutonium L_3 edge XAS from Unaltered ATM-103 2-22
2-16. Molybdenum K-edge XAS from ATM-103 CSNF Using Bent-Laue Analyzer Detection at the APS 2-22

FIGURES
(Continued)

Page

2-17. EXAFS Measurements from Molybdenum in Bulk, Unaltered ATM-103 Fuel Compared with That from Molybdenum and Technetium in Epsilon Particles That Segregated During ATM-106 Fuel Corrosion 2-22
2-18. Uranium XAS Map of S62J-104 Specimen 2-23
2-19. Line Scans Showing Total Uranium Intensity and Ratio of Neptunium to Uranium Signal 2-23

3-1. Dissolved Concentrations After Precipitation Plotted as a Function of Measured Final pH for (a) U, (b) Np, and (c) Ni 3-19
3-2. Percent Uptake After Precipitation Plotted as a Function of the Measured Final pH for (a) U, (b) Np, and (c) Ni 3-20

4-1. Results of MCC-1 Tests Conducted with SRL 202G Glass in pH Buffers 4-29
4-2. Results of MCC-1 Tests Conducted with Hanford-H Glass in pH Buffers 4-30
4-3. Photomicrograph of Cross-Section of Sample H44 from Test VHanH(150)-2 4-31
4-4. Measured Layer Thicknesses for Samples from Standard VHTs Conducted at 150 and 200ºC 4-31
4-5. Degradation of Hanford-H Glass in Excess-Water VHTs 4-32
4-6. Measured Rates for SRL 202G Glass vs. Modeled Rates 4-41
4-7. Comparison of Tests in Leachants without Added Salt and with Added Salt 4-42

5-1. Water Loss from PCT Solutions in Isopiestic Tests with Saturated Solutions of KCl and KNO_3 and with Demineralized Water 5-9
5.2. Water Uptake Rates for Salts from Evaporated PCT Solutions at Various Humidities 5-10
5-3. Water Uptake Rates for Vapor-Hydrated Glass at Various Relative Humidities for SRL 202U Glass and SRL 131U Glass 5-11

TABLES

		Page
2-1.	Characteristics of the Spent Fuels Tested	2-4
2-2.	Electron Diffraction Data from S62J-92 Solids	2-11
2-3.	Comparison of d-spacings from Na/K Boltwoodite and Observed in S62J-92	2-12
3-1.	ICP-MS Data and Dilutions for Test Solutions Prior to Precipitation	3-13
3-2.	ICP-MS Data and Dilutions for Test Solutions After Precipitation	3-15
3-3.	Results of Coprecipitation Tests	3-17
4-1.	Matrix of Tests	4-21
4-2.	Glass Compositions	4-22
4-3.	Nominal Buffer Compositions and pH Values	4-23
4-4.	Measured Boron Concentrations and NL(B) for Tests with SRL 202G Glass at 40ºC	4-24
4-5.	Summary of Rates Regressed from Tests at 40ºC with SRL 202G Glass	4-25
4-6.	Boron Concentrations and NL(B) for MCC-1 Tests and PCTs with Hanford-H Glass	4-25
4-7.	Layer Thicknesses for VHT Samples of Hanford-H Glass	4-26
4-8.	B and Si Concentrations and Calculated NL(i) for Excess-Water VHTs with Hanford-H Glass	4-27
4-9.	Summary of Degradation Rates for Hanford-H Glass Based on NL(B)	4-28
5-1.	Matrix for Tests Used to Generate Test Samples for Isopiestic Tests	5-7
5-2.	PCT Solutions Used in Isopiestic Tests	5-7
5-3.	Mass Changes of PCT Solutions	5-7
5-4.	Water Uptake by PCT Salts	5-8
5-5.	Water Uptake by VHT Samples	5-9

ACRONYMS

ANL	Argonne National Laboratory
APS	Advanced Photon Source
ASTM	American Society for Testing and Materials
ATM	approved test material
BSC	Bechtel SAIC Company, LLC
BWR	boiling water reactor
CSNF	commercial spent nuclear fuel
DWPF	Defense Waste Processing Facility
DIW	deionized water
EDS	energy dispersive x-ray spectroscopy
EELS	electron energy loss spectrometry
EXAFS	extended x-ray absorption fine structure
FY	fiscal year
HA	humid air
HDR	high drip rate
HLW	high-level waste
ICP-AES	inductively coupled plasma – atomic emission spectrometry
ICP-MS	inductively coupled plasma – mass spectrometry
LDR	low drip rate
MCC-1	Materials Characterization Center – Test Method 1
MPO	Memorandum Purchase Order
MR-CAT	Materials Research – Collaborative Access Team
MWd/kgU	Megawatt days per kilogram of Uranium
NEA	Nuclear Energy Agency
NIST	National Institute of Standards and Technology
NL(i)	normalized mass loss (based on element i)
NRC	Nuclear Regulatory Commission
PA	performance assessment
PCT	product consistency test
PNNL	Pacific Northwest National Laboratory
PWR	pressurized water reactor
QA	Quality Assurance

ACRONYMS
(Continued)

RCRA	Resource Conservation and Recovery Act
RH	relative humidity
RIT	Repository Integration Team
SEM	scanning electron microscopy
SITP	scientific investigation test plan
S/V	surface area-to-volume (ratio)
TBD	technical basis document
TEM	transmission electron microscopy
TSPA	total system performance assessment
VHT	vapor hydration test
WF	waste form
XAS	x-ray absorption spectroscopy
XANES	x-ray absorption near-edge spectroscopy
XRD	x-ray diffraction
YMP	Yucca Mountain Project

EXECUTIVE SUMMARY
(J. Cunnane)

This report describes the experimental work performed at Argonne National Laboratory (ANL) during fiscal year 2004 (FY 04) under the Bechtel SAIC Company, LLC (BSC) Memorandum Purchase Order (MPO), contract number B004210CM3X. Important results related to the technical bases, uncertainties, validation, and conservatism in current source term models are summarized below.

An examination of specimens of commercial spent nuclear fuel (CSNF) that had been subjected to corrosion testing for up to 10 years under hydrologically unsaturated conditions was undertaken to elucidate radionuclide release pathways and mechanisms. Significant results from this work include the following:

- It was observed that neptunium and plutonium in CSNF samples remained in close proximity to the corroding surface during corrosion and were not retained in the alteration rind. (In seeming contrast, separate studies that focused on coprecipitation of neptunium in uranyl alteration phases showed significant retention of neptunium in these phases.) These experimental observations are consistent with the hypothesis that Np is not oxidized to the soluble Np(V) oxidation state as the fuel corrodes because the potential needed to affect this oxidation is higher than the corrosion potential of the CSNF matrix that hosts the neptunium in the Np(IV) oxidation state. This may explain the apparent discrepancy between reported association of neptunium with uranyl phases in direct synthesis experiments and the very low (to absent) levels of neptunium observed in uranyl alteration phases derived from corroded CSNF. It is consistent with the hypothesis that the CSNF-derived uranyl phases are relatively depleted in neptunium because neptunium has resisted oxidation and is thus not available in the solution from which uranyl phases are precipitated. Confirmation of this hypothesis would support replacement of the conservative assumption that Np_2O_5 controls Np solubility with an NpO_2-controlled model. Demonstration that the solubility of neptunium is controlled by the quadravalent rather than pentavalent oxidation state could result in a significantly less conservative Total System Performance Assessment (TSPA) model. Coprecipitation models (where neptunium is sequestered in precipitated uranyl phases) are not precluded by this observation, although uranyl/neptunyl-phase paragenesis may be more complex than currently anticipated.

- The CSNF samples were observed to corrode in a “general corrosion” manner manifested by fairly uniform corrosion at the fuel’s peripheral surfaces, rather than via widespread grain boundary attack. This could indicate that current estimates of the uncertainties in the effective surface area of corroding CSNF are conservative and could be relaxed if these observations were quantified and verified.

- Significant partitioning of technetium and molybdenum was observed between the fuel matrix and relatively stable noble metallic ("epsilon") particles, which survived intact after 10 years of oxidative corrosion. Substantial retention of technetium by these stable metal particles could indicate that the current TSPA model assumption of prompt release of technetium upon oxidation, or oxidative dissolution, of CSNF is very conservative.

Results obtained from experimental investigation of the coprecipitation of Np(V) with uranyl [i.e., U(VI)] phases are consistent with the hypothesis that neptunium may be incorporated into uranyl oxide hydrate precipitates if sodium is present to provide charge balance in the precipitating phase.

Results from waste glass corrosion testing showed that the current model's temperature dependence for acidic and alkaline conditions is valid down to 40°C and that the model's parameter values are applicable to Hanford high-level waste (HLW) glass compositions.

Isopiestic tests conducted on glass corrosion "rind" produced by vapor hydration tests (VHTs) and on the evaporated salt residue from Product Consistency Test (PCT) solutions showed that:

- Deliquescence is an important process for water accumulation on corroding waste glass exposed to humid air.

- The rate of water accumulation is dependent on relative humidity (RH) and may represent an important process for water accumulation and radionuclide transport out of codisposal waste packages exposed to humid air.

1.0 INTRODUCTION
(J. Cunnane)

This report describes the experimental work performed at Argonne National Laboratory (ANL) during fiscal year 2004 (FY 04) under the Bechtel SAIC Company, LLC (BSC) Memorandum Purchase Order (MPO), contract number B004210CM3X. Technical support activities performed under this contract in FY 04 are not described. Those activities included supporting the Repository Integration Team (RIT) revision of the waste form modeling reports, supporting the Total System Performance Assessment (TSPA) Validation Team review of TSPA models, preparation of the technical basis document (TBD), and participating in the Nuclear Regulatory Commission (NRC) review of the commercial spent nuclear fuel (CSNF) modeling report.

The report is organized into four major sections corresponding to the experimental activities into which the FY 04 work was organized. This work was conducted under the current revision of the quality assurance (QA) plan entitled "Quality Assurance Plan for Technical Activities in Support of the Yucca Mountain Project (ANL QA Document No. YMP-02-001, Rev. 5).

2. EXAMINATION OF CORRODED CSNF
(J. Fortner)

2.1 BACKGROUND

The quantity and chemical speciation of radionuclides available for release and mobilization from breached waste packages at Yucca Mountain, Nevada, will be determined, in part, by the mechanisms, rate, and time of waste form (WF) degradation. The WF models are almost exclusively developed based on solution results from WF or simulant testing; they include only anecdotal evidence of WF evolution and radionuclide release mechanisms gleaned directly from examination of the solid WF and alteration product materials themselves.

As part of the WF degradation testing, ANL performed unsaturated tests on approved test material (ATM) CSNF fragments for up to 10 years under the test plan, SITP-02-WF-001, Rev. 00, to supply WF degradation data for development of source term model reports. These tests were stopped at the end of fiscal year 2003 (FY 03). To improve the technical bases and reduce uncertainties in the model reports, ANL began detailed microscopy and spectroscopy studies on selected corroded fuel specimens from these unsaturated tests in FY 04. These analyses are designed to elucidate key processes that have large uncertainties in the current models, as described in the test plan "Test Plan for Analysis of Solids from Unsaturated Testing of Spent Nuclear Fuel," ANL-TP-04-001, Rev. 00, under which the solids analysis work is being performed.

The waste form model reports are based on data from experimental WF testing and analysis programs. Test results were used to identify and characterize many of the separate processes and products involved with the WF degradation. Starting with uncorroded spent fuel, the release of radionuclides requires wetting the fuel surface, oxidation of the fuel's solid phases, and solubilization of the radionuclides from their host solid matrix. Subsequent radionuclide mobilization away from the fuel may be controlled by mineral solubility, colloid formation, liquid/solid phase interactions such as adsorption and precipitation, and trace element incorporation into newly formed solid phases. Which of these processes control radionuclide release and mobilization depends not only on the specific radionuclide, but also in a coupled manner on coexisting waste form degradation, dissolution, and precipitation processes. Because the released radionuclide concentrations depend on processes that are not completely understood, the model reports include conservative assumptions to encompass the uncertainties associated with several WF degradation processes.

The objective of the work described herein is to provide systematic documentation of the alteration phase solids that formed on the surface of spent fuel that was corroded in the unsaturated tests. Specific objectives are to (1) characterize the alteration phases that may be controlling radionuclide solubility and thus the associated radionuclide mobilization, and (2) document the evolution of the effective surface area of the unclad CSNF in contact with water and humid air. The goals include determination of the role of mineral paragenesis in radionuclide releases and sequestration, the control of trace radionuclide solubility by alteration phase minerals, and changes in the fuel surface area during corrosion.

2.2 PROCEDURES

The spent fuels and their solid alteration products that are characterized in this study are described in Section 2.2.1. Microscopy and spectroscopy methods used to characterize the materials are described in Section 2.2.2; details of other experimental methods used to generate and study the alteration phases can be found in the references.

2.2.1 Test Materials

The characterization of specimens of five spent nuclear fuels and their alteration products from the ANL unsaturated tests is discussed in this report. The unsaturated tests and findings are described in detail elsewhere (Finch et al. 1999, Finch 2003). Two of the fuels, ATM-103 and ATM-106, are pressurized water reactor (PWR) spent fuels with nominal burnups of 30 and 45 megawatt days per kilogram of uranium (MWd/kgU), respectively (Guenther et al. 1988a and 1988b). The other three fuels, designated as ATM-109A, ATM-109B, and ATM-109C (Goldberg 2003) are boiling water reactor (BWR) fuels with burnups of 64, 71, and 72 MWd/kgU, respectively. One BWR fuel (ATM-109C) contains 2% Gd as a burnable neutron absorber. Characteristics of the five fuels, and the types of tests conducted for each fuel, are summarized in Table 2-1.

Each unsaturated fuel test subjected approximately 8 grams of unclad fuel pellet fragments (~5 mm-diameter chunks) to water and/or humid air in a nominally oxidizing environment at 90 °C. The intent was to produce conditions relevant to potential future hydrological conditions at Yucca Mountain. Three test conditions were used: low drip rate (LDR), high drip rate (HDR), and humid air (HA). Tests in humid air are also referred to as vapor tests. The low and high drip rate tests used simulated groundwater with injection rates of 0.15 and 1.5 mL/week, respectively. Humid air exposure tests limited water contact to air at 100% RH. Tests with the PWR spent fuels were run for approximately 10 years (1992 to 2002) and tests with the BWR spent fuels were run for about 4 years (1998 to 2002). Solid alteration phase products from these tests were stored dry at room temperature (ambient laboratory atmosphere) until analysis.

2.2.2 Solids Analysis Methods

Visible Light Microscopy

A starting point for characterizing the state of the CSNF solids from the unsaturated tests was to examine the material using visible light microscopy. This allows qualitative description of alteration phase coverage and distribution along with information regarding how water penetrates intact fuel fragments during corrosion. Of particular interest are details of grain boundary penetration. This information addresses scaling-related questions associated with application of laboratory test results to repository-relevant configurations: Does the rind follow all the contours of the pellet surfaces equally? Do changes in water penetration or exclusion occur as a result of self-sealing of pathways? Natural analogs for the paragenesis of mineral deposits often show reaction front behavior that follows the geometric surface area as opposed to

complex inter-granular penetration. As demonstrated in the following results, evidence of the geometric surface area reaction front behavior is seen in the unsaturated tests of CSNF.

Installation of a new remotely controlled motorized light microscope with digital camera in the hot cell facility was completed near the end of FY 04. This device has been tested and used to examine cross sections of corroded fuel fragments in the as-cut condition. It has provided dramatic improvement in imaging quality over the video camera with macro lens that was the prior means of viewing the fuel. This report includes images from both systems: Figures 2-1 and 2-2 were obtained using the video camera with macro lens and Figure 2-3 was obtained using the new microscope and digital camera.

Scanning Electron Microscopy

Two scanning electron microscopes (SEM) were used in these studies: a Hitachi 3000N and an RJ Lee Personal SEM. The SEM uses a focused beam of electrons to form an image of the surface of CSNF from backscattered or secondary electrons. The SEM provides useful magnifications up to approximately 10,000X. The SEM is also used to provide elemental compositional information with associated energy dispersive x-ray spectroscopy (EDS).

Transmission Electron Microscopy

Analyses were performed with a JEOL FX II transmission electron microscope (TEM) operated at 200 keV beam energy and equipped with EDS and a Gatan™ image filter/electron energy loss spectrometer. This instrument provides high-magnification imaging, electron diffraction (for crystal phase identification), and electron energy loss spectroscopy (EELS) for elemental composition.

The TEM specimens must be prepared as electron-transparent thin sections. For a TEM with 200 keV beam energy, a uranium oxide sample must be less than 100 nm thick to be effectively transparent. Often, small crystallites can be prepared by taking a scraping of fines of the material, which are then suspended in ethanol and transferred, using a pipette, to a carbon-coated TEM grid and allowed to dry. While this type of preparation is simple, it does not work for all materials and does not preserve orientation information among different phases within a sample. A more complex and time-consuming method of preparation is to thin-section a specimen using a diamond knife in an ultramicrotome. Using this approach, a small fragment of the sample is embedded in epoxy, which is then meticulously sliced away by passing the epoxy block across a stationary diamond knife using an ultramicrotome. On each pass of the ultramicrotome arm, the epoxy block containing the sample is advanced by a few tens of nanometers. The ultramicrotomed thin sections are floated on ultrapure water and collected on a TEM grid for later analysis. Results from samples prepared by pipette transfer by and ultramicrotome methods are included in this report.

X-Ray Absorption Spectroscopy

Few techniques have proven more effective than x-ray absorption spectroscopy **(**XAS) for determining oxidation states and structural environments of elements in solids. Using a novel

bent-Laue analyzer, we have obtained detailed XAS information from trace elements in specimens of CSNF. Several XAS measurements from CSNF were performed at the Materials Research Collaborative Access Team (MR-CAT) insertion device beamline located at Sector 10 of the Advanced Photon Source (APS). The brightness of the APS facility in the high-energy x-ray regimes makes it ideal for investigating radionuclide systems, which have relatively high-energy absorption edges and which must be carefully encapsulated for radiological safety. This approach has allowed, for the first time, direct observation of oxidation state, coordination environment, and site symmetry of fission product and actinide elements in CSNF and its alteration products.

Table 2-1. Characteristics of the Spent Fuels Tested [a]

Fuel	**ATM-103** [b]	**ATM-106** [c] **NBD107**	**ATM-109A** [d]	**ATM-109C** [d]	**ATM-109B** [d]
Reactor	PWR	PWR	BWR	BWR	BWR
Burnup (MWd/kgU)	30	45	71	64	72
Grain Size (µm)	17-20	6-16	~15	Bimodal 5, 10-20	~30
Fission Gas Release (%)	<0.25	11	4.4	3.5	2.95
Rim Structure Thickness (µm)	None	100	80-140	150-250 Confined to 5 µm grains	100-180
Out-of-reactor	1980	1980	1991	1991	1991
Gd (%)[e]	<0.02	<0.02	<0.02	2	<0.02
Test Type [f]	HDR, LDR, HA	HDR, LDR, HA	HDR, HA	HDR, HA	HA
Approximate test duration (years)	10	10	4	4	4

[a]Adapted from SITP-02-WF-001, Rev. 00.
[b](Guenther et al. 1988a).
[c](Guenther et al. 1988b).
[d](Vaidyanathan et al. 1997). See also Goldberg 2003.
[e]All fuels have radiogenic Gd from fission; ATM-109C was doped with 2% Gd as burnable neutron poison.
[f]HDR = high drip rate (~1.5 mL/week); LDR = low drip rate (~0.15 mL/week), HA = humid air (saturated water vapor in air).

2.3 RESULTS

2.3.1 Alteration Phase Characteristics – Visible Light Microscopy

Light microscopy of the CSNF post-test solids revealed a coating of white-to-yellow alteration products covering most of the (initially black) oxide fuel (Figures 2-1a to 2-1k). Some areas of the alteration coating had been spalled off, either incidentally from handling or through a deliberate effort to recover some of the alteration material. The coating of alteration material is mildly adherent, but appears unlikely to serve as an effective protective layer for the underlying fuel. As illustrated in Figures 2-1a to f, the general appearance of the alteration of the fuel from the HDR, LDR, and HA tests is similar. The alteration materials coating the ATM-109 fuels (Figures 2-1g to k) are sparser owing to the shorter test duration (4 years vs. 10 years for the ATM-103 and -106 fuels).

To provide greater detail, selected fragments of the CSNF specimens were embedded in epoxy resin and cross-sectioned using a diamond-blade saw. Light microscopy of these cross-sectioned fragments in the as-cut condition revealed that the alteration rind was relatively thin and mostly adherent (Figure 2-2). There was no evidence of gross grain boundary penetration or degradation of the interior of the CSNF fragments.

Using the new remotely controlled motorized light microscope with digital camera in the hot cell, we reexamined cut specimens of ATM-103 tested under low drip rate test conditions (Figures 2-3a–c) that had been previously imaged using the video camera (Figures 2-1 and 2-2). Note that the epoxy resin has turned a dark gray owing to radiation damage. Specimens of ATM-106 tested under high drip rate test conditions for 10 years were also epoxy-embedded and cross-sectioned in the hot cell. Digital photomicrographs were taken using the light microscope, revealing a thin (~100 micrometer) alteration rind surrounding relatively intact fuel fragments (~5 mm across) (Figure 2-3b). The alteration rind appears somewhat thicker than that seen on the low drip rate tests on ATM-103 (Figure 2.3a). However, the alteration appears to have been localized to the region near the geometric surface.

2.3.2 SEM and TEM Results

Examination of Alteration Phases from Test S62J-92

This section describes SEM and TEM examinations of alteration phase material taken from test S62J-92, a high drip rate unsaturated test of ATM-106 fuel fragments sampled at 92 months of testing.[§] This material had been stored in a labeled container since it was removed from the ongoing test on December 12, 2000.

The S62J-92 material was recovered from storage and consisted of pale yellow crystallites affixed to double-sided cellophane tape. Cutting with a razor separated a piece of the tape, and the fraction of material on the cut-away tape was transferred to an aluminum SEM stub. The specimen was examined with a Hitachi 3000N SEM using a low-vacuum mode that dissipated accumulated charge and obviated the need to carbon coat the sample.

The sample was found to consist mostly of plate-like, or sometimes needle-like (acicular) alteration phases containing uranium, sodium, and silicon. Occasionally, particles containing only uranium (note: EDS is insensitive to oxygen) were found that had a topography strongly suggesting that they were individual fuel grains (Figure 2-4). The fuel grains often showed evidence of pitting on the surface. A single molybdenum-ruthenium-palladium particle was observed, and it is identified as an epsilon (5-metal) particle based on its composition and appearance. The alteration crystals are shown with the epsilon (ε) particle and a fuel grain in Figure 2-4. Greater detail, including crystal phase identification of the alteration material, was obtained using the TEM, as described below.

[§] The sample designation “S62J-92” comes from “S” for spent fuel, “6” for ATM-106, “2J” for high drip rate test with EJ-13 water, and -92 denotes the sample was removed after 92 months of testing. “1J” is used to indicate a low drip rate test and “V” to indicate humid air (vapor) test.

A scraping of material was taken from the SEM stub containing alteration phases from the S62J-92 test described above. Fines of this material were then suspended in ethanol and transferred to a carbon-coated TEM grid using a pipette and allowed to dry. This grid was then examined with TEM. The TEM image in Figure 2-5 shows crystallites having the platy morphology that was typically observed. The composition determined by EDS was predominantly uranium, silicon, and sodium (which is consistent with EDS conducted during the SEM analysis). From the EELS analysis, which has a much greater energy resolution than EDS and is sensitive to oxygen, the crystallites also contain oxygen and trace amounts of lanthanum and neodymium. Electron diffraction patterns (Figure 2-6) were taken from several crystallites range from a nearly powder pattern (Figure 2-6a) to close to a zone axis pattern (Figure 2-6b). The measured diffraction spacings (d-spacings) are tabulated in Table 2-2. The satellite peaks in Figure 2-6b arise from some unidentified superstructure, perhaps lamellar twinning. The combined d-spacings from the seven diffraction patterns in Table 2-2 match reasonably well with those reported by Burns (1998) for sodium/potassium boltwoodite [$(Na,K)(UO_2)(SiO_3OH)(H_2O)_{1.5}$], as seen in Table 2-3. Missing diffraction spacings are due largely to preferred orientation of a relatively small number of crystals, which precludes obtaining a true powder pattern in the TEM. The composition of sodium boltwoodite is consistent with the EDS and EELS analyses, and it is a phase detected in tests of unirradiated UO_2 under similar unsaturated conditions (Wronkiewicz et al. 1992, 1996).

Although sodium boltwoodite is a phase identified by Burns et al. (2004) as a likely candidate for coprecipitation of neptunium within a uranium phase, EELS placed the concentration level of neptunium below the level of detection in this sample. However, due to plural scattering interference (see Fortner et al. 2004), the detection level for neptunium in the uranium matrix is about 1 atom neptunium in 200 atoms of uranium. This is well above the concentrations of neptunium in the parent fuel, or what is expected in sodium boltwoodite precipitated from solution by assuming Henry's Law behavior (Finch and Cunnane 2001), or that used in reactive transport modeling (Chen 2003). An approach for detecting neptunium in alteration phases using the more sensitive detection capabilities of synchrotron XAS is described later in this report, parts of which have been published elsewhere (Fortner et al. 2004).

TEM Examination of a Plutonium-Enriched Interface in Sample S61J-49

A small chip of material taken from test sample S61J-49, a low drip rate unsaturated test of ATM-106 fuel fragments sampled at 49 months of testing, had been separately prepared for TEM examination using an ultramicrotome to prepare electron-transparent thin sections. Previous examination of these sections revealed a thin region between the unaltered CSNF and a uranyl alteration rind that was enriched in plutonium, zirconium, rare earth elements, and possibly americium relative to the fuel (Buck et al. 2004). A detailed description of the layer has been published by Buck et al. (2004). However, a resurgent interest in the fate of neptunium led us to re-examine this material. This sample, which was recovered after 49 months of testing, provides a retrospective viewpoint for comparison with similar interfacial TEM specimens that will be taken from the 10-year tests.

The TEM micrograph in Figure 2-7 shows uranium oxide fuel with epsilon particles and a wispy alteration material that is enriched in plutonium and americium relative to the fuel. The

same field of view appears in Figure 2-8, which was formed using an energy filter tuned to the uranium $O_{4,5}$ edge at 98 eV (the plutonium $O_{4,5}$ edge is also accepted by the filter). The bright areas in Figure 2-8 contain actinides, while the dark areas generally consist of mounting epoxy and epsilon particles. One striking aspect of the images is the presence of submicron-sized epsilon particles in the region of fuel that is actively corroding. This observation is important because it indicates that the technetium in the epsilon particles may not be released when the fuel matrix corrodes. The persistence of epsilon particles during corrosion is revisited in Section 2.3.3.

Compositional information from EELS shows that the altered material, which is actually a thin transition zone between the unaltered fuel and the uranyl alteration rind (Buck et al. 2004), can be enriched in plutonium and americium by up to 15 times relative to the unaltered fuel (Figure 2-9). The enrichment actually varied from location to location within this material. Interestingly, there is no evidence of neptunium enrichment in the alteration rind, as the neptunium EELS signal should be approximately 60% of the americium signal based upon ORIGEN calculations (Guenther et al. 1988b). However, it should be noted that the noise level of the spectrum of Figure 2-9 would put the neptunium signal just at the level of detection if neptunium was enriched 15 times relative to unaltered CSNF. Plural scattering effects further complicate detection of this weak neptunium EELS signal (Fortner et al. 2004). Given the very thin plutonium-enriched zone (~100 nm), and the approximately 20:1 ratio of plutonium to neptunium in the fuel, a separate neptunium-rich zone would be extremely small and likely escape detection. Further studies using fuel fragments corroded for longer times and with greater alteration are planned to help resolve the open question of the neptunium disposition as the fuel corroded.

Although the epsilon particles are composed mostly of molybdenum, technetium, ruthenium, rhodium, and palladium, the EELS spectrum in Figure 2-10 shows only molybdenum and ruthenium in the epsilon particles that are embedded in the alteration material. This is because the technetium concentration is low enough that the EELS signal would be at the noise level of the spectrum in Figure 2-10, and the rhodium and palladium peaks are obscured by the oxygen peak that arises from the fuel and the plutonium layer.

2.3.3 X-Ray Absorption Spectroscopy Results

By analyzing x-ray absorption spectra from a particular element's absorption edge, the oxidation state and local coordination environment of that element can be determined. Photoelectron scattering from neighboring atoms creates a subtle modulation of the absorption above the edge energy known as extended fine structure (Stern 1988). Careful analysis of the extended x-ray absorption fine structure (EXAFS) contained within the absorption edge spectrum yields detailed information about the absorbing element including distances to near neighbors, types and numbers of neighboring atoms, and details of the radial distribution function (Stern 1988). The energy of the absorption threshold and near-edge absorption features also can be used to obtain information about the charge state of the central atom and the site symmetry. Typically, one measures x-ray absorption as a function of incident x-ray energy by monitoring the fluorescence yield in an energy window that includes an emission line of the element of interest. A fundamental difficulty in detecting and measuring the x-ray absorption spectra of the small

quantities of Np, Mo, or Tc in a uranium matrix is that the K-α fluorescence x-rays are not well separated in energy from the uranium L-β lines. Solid-state detectors cannot resolve these energies at sufficient count rates. Measuring useful spectroscopic information requires that the background from the matrix uranium be substantially decreased. To achieve the required spectral resolution, we used a bent-Laue analyzer (Figures 2-11 and 2-12) having a bandwidth of about 75 eV to separate the tails of the uranium fluorescence peak from the Mo and Tc K-α fluorescence. Detailed discussion of the principles of the bent-Laue analyzer can be found in Zhong et al. (1999) and Karanfil et al. (2000). Specifics regarding the application of the bent-Laue analyzer to trace element spectroscopy in a uranium matrix can be found in Kropf et al. (2004) and Fortner et al. (2004).

Several specimens of reacted CSNF were chosen for synchrotron XAS studies. The goals, as stated in the Test Plan (ANL 2004), were to examine the sequestration of key radionuclides (Np, Pu, and Tc) into alteration phases and noble metal particles (also referred to as epsilon particles), which may affect their long-term release behavior. The XAS specimens included a sample of reacted ATM-106 fuel from a high drip rate unsaturated test sampled after 104 months. This sample was expected to be very similar to the S62J-92 sample that was discussed earlier because it is from the same test, only it was sampled 12 months later. The SEM micrograph of the ATM-106 sample in Figure 2-13 shows an anomalous agglomeration of epsilon particles near the surface of a reacted fuel grain. These are surrounded by acicular alteration phases, which are probably sodium boltwoodite, based on morphology and composition. This identification is consistent with the material identified by electron diffraction in the S62J-92 sample, discussed earlier. The agglomeration of epsilon particles in the alteration zone is reminiscent of that described earlier in the TEM study of the Pu enrichment layer in S61J-49, although at a much larger scale.

A separate XAS examination was done on an ATM-103 fuel grain that had been pulled from an apparently unaltered zone in a high drip rate test sampled at 44 months (S32J-44). This sample was described as unaltered fuel because it retained the characteristic black appearance of unaltered fuel, rather than the characteristic yellow or white of the alteration products. This specimen was used as a baseline to establish the capability of XAS to detect and analyze neptunium in a CSNF sample. Figures 2-14 and 2-15 show the absorption spectra for Np and Pu in the ATM-103 S32J-44 sample. From XAS (Figure 2-14), Np is present in the fuel at ratio of only 0.4 mg Np/gram U, as calculated by Guenther et al. (1988a), or 0.6 mg Np/gram U, as measured from the fluorescence spectra. The background on which the Np L3-edge spectrum rides includes uranium fluorescence that makes it through to the detector and an unexpected contribution from inelastic scattering that is attributed to the uranium. At 1 part in 1700, the Np signal-to-background ratio is 0.15, barely large enough to measure a usable EXAFS signal. The data shown are summed from 24 hours of data acquisition. Much better counting statistics are needed to determine the Np coordination environment. Nevertheless, from comparing the x-ray absorption near-edge spectroscopy (XANES) result with published spectra, it seems reasonable to assign to the Np a +4 oxidation state (Soderholm et al. 1999). The EXAFS data for the two detectors (see inset, Figure 2-14) also suggest that Np is present in a UO_2-like phase, given the similarity to the PuO_2 and UO_2 spectra [Np to O distance, i.e., RNp-O = 2.34 Å and some evidence for RNp-Ac = 3.85 Å]. Higher-quality data to 12 $Å^{-1}$ would make this a much more convincing argument. If these data are corroborated by further evidence, the Np is also likely dispersed in the UO_2 on the U sites.

Plutonium, having a higher concentration in the fuel (8.3 mg Pu/gram U) (Guenther et al. 1988a), gives a better signal (Figure 2-15). The EXAFS data (not shown) clearly identify the Pu in a PuO_2-like phase (Richmann et al. 2001). Fitting the data using methods similar to that used by Richmann et al. results in R_{Pu-O} = 2.33 Å and R_{Pu-Ac} = 3.86 Å, where Ac is Pu or U, which have similar backscattering amplitudes and phase shifts. These values are quite similar to those determined for bulk PuO_2 by Richmann et al. based on a fluorite-type crystallographic structure, R_{Pu-O} = 2.344 Å and R_{Pu-Pu} = 3.833 Å. Incorporation of Pu into the UO_2 matrix (which also has a fluorite-type structure) is far more likely than the existence of a separate PuO_2 phase.

Mo is present at a concentration of 3.0 mg Mo/gram U (Guenther et al. 1988a). The XAS signal of Mo in ATM-103 fuel (Figure 2-16) is consistent with a mixture of metallic and oxide molybdenum. The Fourier transform of the EXAFS reveals some Mo-O [R = 2.14 Å] and a larger number of Mo-metal [R = 2.61 Å] scattering paths, indicating that the Mo is present in both oxide and metallic forms. A separate study of molybdenum and technetium in the high drip rate test with ATM-106 (Figure 2-17; see also Fortner et al. 2004) showed that regions enriched in epsilon particles could be located using XAS. The EXAFS signals of molybdenum and technetium in Figure 2-17 look very similar (aside from a small phase shift at low momentum transfer, *k*), indicating that these elements reside in similar crystal chemical environments in the epsilon phase. These spectra differ from that obtained for a molybdenum metal reference material, probably because pure molybdenum metal has a body-centered cubic crystal structure and the epsilon phase has a hexagonal close-packed structure.

The S62J-104 sample was later used in an XAS study to better ascertain the fate of neptunium during corrosion. The uranium XAS map in Figure 2-18 was obtained by translating the specimen through the beam while a solid-state detector counted x-rays from the uranium L-α fluorescence. The horizontal line in the figure indicates the path of a line scan (Figure 2-19) that was obtained by simultaneously collecting uranium and neptunium near-edge XAS at multiple points along the path as the sample was translated. The uranium spectrum was obtained using a conventional solid-state detector, while the neptunium spectrum was collected using the bent-Laue analyzer and a separate x-ray detector (e.g., ion chamber). The scan in Figure 2-19 shows both the total uranium intensity and the ratio of the neptunium signal to that of uranium. The uranium signal can be separated into high-intensity regions containing intact fuel (dark areas in Figure 2-18), and moderate-intensity areas containing uranyl phases (lighter areas in Figure 2-18). Neptunium is closely associated with the intact fuel rather than the uranyl phases, with a nominal concentration (as a fraction of uranium) near the expected value of 0.00047 from Guenther et al (1988b). However, there are two regions that show deviations from this behavior: an enrichment of neptunium near the left edge of the scan (reaching a fraction of 0.0007 at the point labeled "3") and a shoulder to the right of the small grain just right of center in the scan, where neptunium coexists with uranyl phases at a depleted fractional concentration of about 0.0001. These findings are consistent with neptunium not oxidizing and dissolving when the UO_2 matrix undergoes oxidative dissolution (leading to surface enrichment of neptunium), and with little Np coprecipitation into uranyl phases. Previous studies (Fortner et al. 2004) have indicated that coprecipitation does not occur at higher levels. This may be due to the fact that Np(IV) has a higher oxidation potential than the fuel's corrosion potential, which leads to little Np(V) release and consequently lower neptunium concentrations in the uranyl alteration phases.

While more data are needed to confirm this hypothesis, it is consistent with *all* of the known observations on neptunium oxidation kinetics and precipitation/coprecipitation.

The more intense uranium signals in Figure 2-19a coincide with fuel grains, while intermediate signal levels indicate uranyl alteration phases. The neptunium appears to remain localized in or near the unaltered fuel, with a suggestion of enrichment above the nominal Np/U level of 0.00047 toward the left edge of the figure at position "3." These spectra are consistent with Np(IV), with the possible exception of spectrum 12, which may indicate a mixed valence (Kropf et al. 2004).

Table 2-2. Electron Diffraction Data from S62J-92 Solids[a]

S62J-92solids.1	
Q (1/Å)	d (Å)
0.93	6.76
1.28	4.93
1.70	3.71
1.86	3.39
2.43	2.59
2.72	2.31
2.75	2.28
2.88	2.18
3.20	1.97
3.98	1.58

S62J-92solids.2	
Q (1/Å)	d (Å)
0.93	6.76
1.28	4.91
1.84	3.41
1.97	3.20
2.04	3.09
2.44	2.58
2.79	2.26
2.89	2.17
3.20	1.97

S62J-92solids.3	
Q (1/Å)	d (Å)
1.33	4.74
1.85	3.40
2.05	3.06
2.13	2.96
2.95	2.13
2.98	2.11
3.00	2.10
3.32	1.89
3.72	1.69
3.78	1.66

S62J-92solids.8	
Q (1/Å)	d (Å)
1.27	4.97
1.74	3.61
2.06	3.05
2.08	3.03
2.75	2.28
3.20	1.96
3.47	1.81
4.10	1.53
4.40	1.43
4.74	1.33
5.25	1.20

S62J-92solids.9	
Q (1/Å)	d (Å)
0.98	6.44
1.75	3.59
1.78	3.54
2.12	2.96
2.85	2.21
3.33	1.89
3.58	1.76
3.73	1.69

S62J-92solids.12	
Q (1/Å)	d (Å)
1.27	4.95
1.84	3.42
1.86	3.38
2.01	3.13
2.04	3.09
2.06	3.06
2.82	2.23
2.86	2.20
3.26	1.93
3.32	1.90
3.51	1.79
3.65	1.72
3.70	1.70
4.06	1.55
4.07	1.54
4.57	1.38

S62J-92solids.14	
Q (1/Å)	d (Å)
1.76	3.58
2.09	3.01
3.24	1.94
3.51	1.79
3.77	1.67
4.13	1.52
4.78	1.31
5.17	1.22
5.27	1.19
0.21*	30.65*

*satellite peak

[a]The measured electron momentum transfer (Q) is tabulated along with the more familiar crystal d-spacing, d, where $d = 2\pi/Q$. The results are for 7 separate measurements, with data filenames heading each list of measurements.

Table 2-3. Comparison of d-spacings from Na/K Boltwoodite[a] and Observed in S62J-92[b]

d (Å)	Na/K Boltwoodite Relative Intensity	Na/K Boltwoodite Miller Indices h k l	S62J-92 0bserved[c]	d (Å)	Na/K Boltwoodite Relative Intensity	Na/K Boltwoodite Miller Indices h k l	S62J-92 Observed [c]
6.8366	999	1 0 0	1, 2	2.7169	1		
6.4219	331	0 0 1	9	2.695	18	1 2 1	
5.4339	194	$\underline{1}$ 0 1		2.6543	5		
4.9111	5	1 1 0	1, 2, 8, 12	2.5528	42	2 1 1	1,2
4.7504	252	0 1 1	3	2.5356	56	$\underline{2}$ 1 2	
4.306	142	$\underline{1}$ 1 1		2.4845	91	1 1 2	
4.1732	26	1 0 1		2.4556	57	2 2 0	
3.5924	212	1 1 1	1,8,9,14	2.4504	64	$\underline{2}$ 2 1	
3.5298	234	0 2 0	9	2.3898	1		
3.4183	224	2 0 0	1,2,3,12	2.3752	1		
3.4045	220	$\underline{2}$ 0 1	1,12	2.3474	27	$\underline{3}$ 0 1	1
3.2472	3			2.2788	41	3 0 0	1,8
3.2109	9		2	2.2275	12	$\underline{3}$ 1 1	12
3.1364	329	1 2 0	12	2.2095	87	$\underline{1}$ 0 3	9,12
3.0933	38	0 2 1	2,12	2.1686	17	3 1 0	
3.0766	14	2 1 0		2.1594	27		
3.0665	27	$\underline{2}$ 1 1	3,8,12	2.153	15		
2.9601	145	$\underline{1}$ 2 1	8,14	2.1406	40		3
2.9501	301	$\underline{1}$ 1 2	3,9	2.1214	3		
2.9228	282	0 1 2		2.1111	33		3
2.7381	2						

[a]Burns 1998.

[b]The published data are matched to the experimental d-spacings from Table 2.2 as "observed." Only spacings > 2.11 Å are listed.

[c]Indicates similar d-spacing observed in spectrum "S62J-92solids.n" (n = 1, 2, 3, 8, 9, 12, 14).

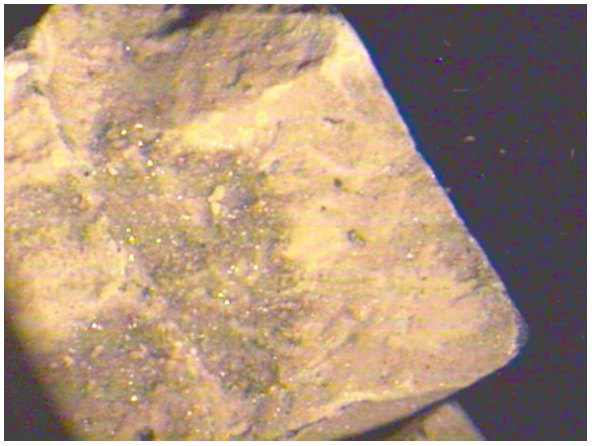

Fig. 2-1a. ATM-103 Fuel Fragments from Vapor Test.

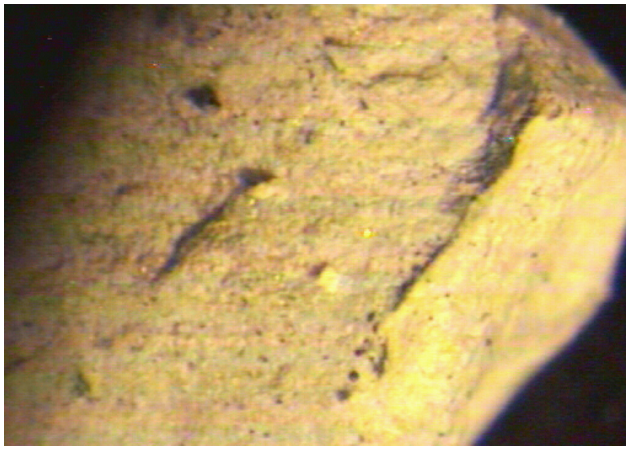

Fig. 2-1b. ATM-103 Fuel Fragments from Low Drip Rate Test.

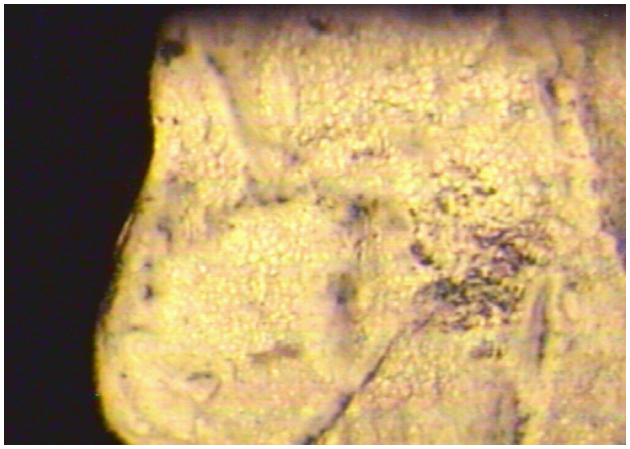

Fig. 2-1c. ATM-103 Fuel Fragments from High Drip Rate Test.

Fig. 2-1d. ATM-106 Fuel Fragments from Vapor Test. Note scale: the outside diameter of the zircaloy fuel holder is 1.34 cm.

Figure 2-1e. ATM-106 Fuel Fragments from Low Drip Rate Test.

Figure 2-1f. ATM-106 Fuel Fragments from High Drip Rate Test.

Fig. 2-1g. ATM-109B Fuel Fragments from Vapor Test.

Fig. 2-1h. ATM-109A Fuel Fragments from Vapor Test.

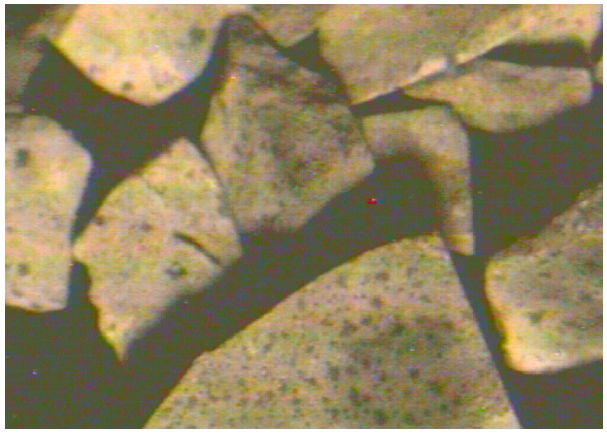

Fig. 2-1i. ATM-109C Fuel Fragments from High Drip Rate Test.

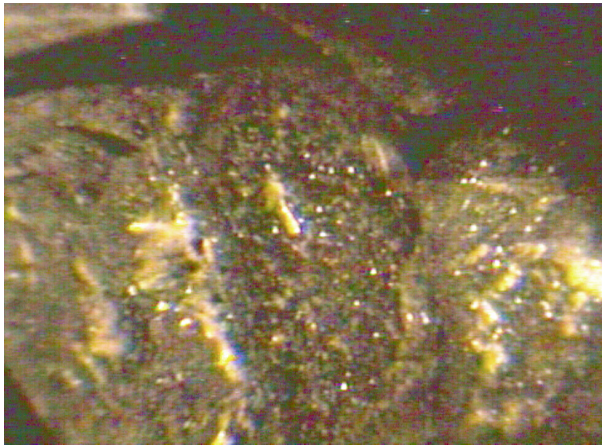

Fig. 2-1j. ATM-109C Fuel Fragments from Vapor Test.

Fig. 2-1k. ATM-109C Fuel Fragments from High Drip Rate Test.

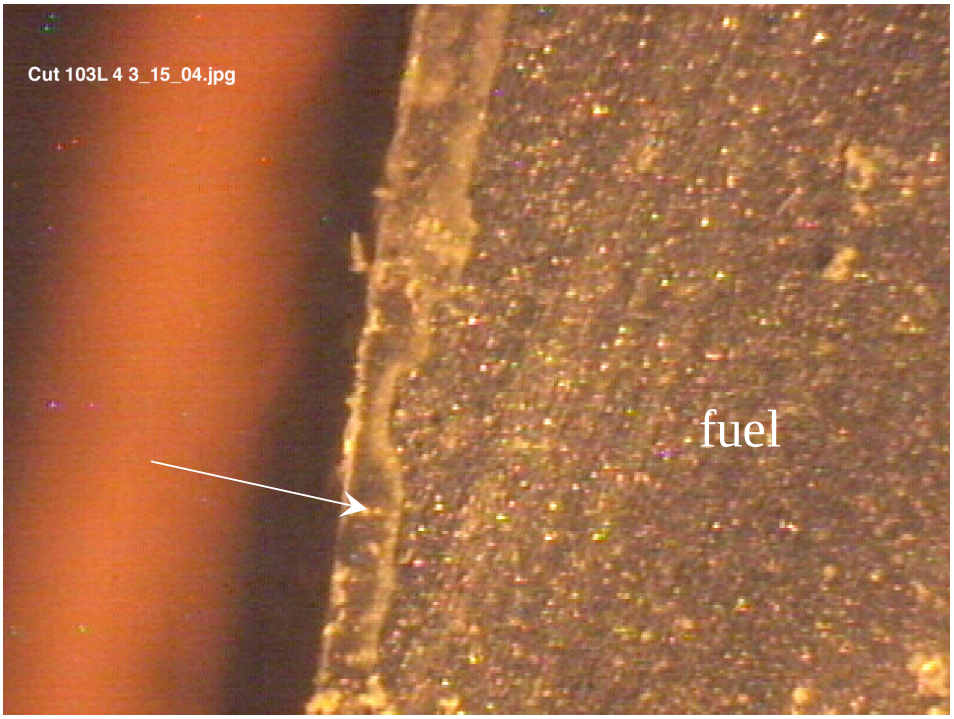

Fig. 2-2. Cross-Sectioned Fragment of ATM-103 Fuel Tested 10 Years under Low Drip Rate Conditions. Arrow points to a thin alteration rind.

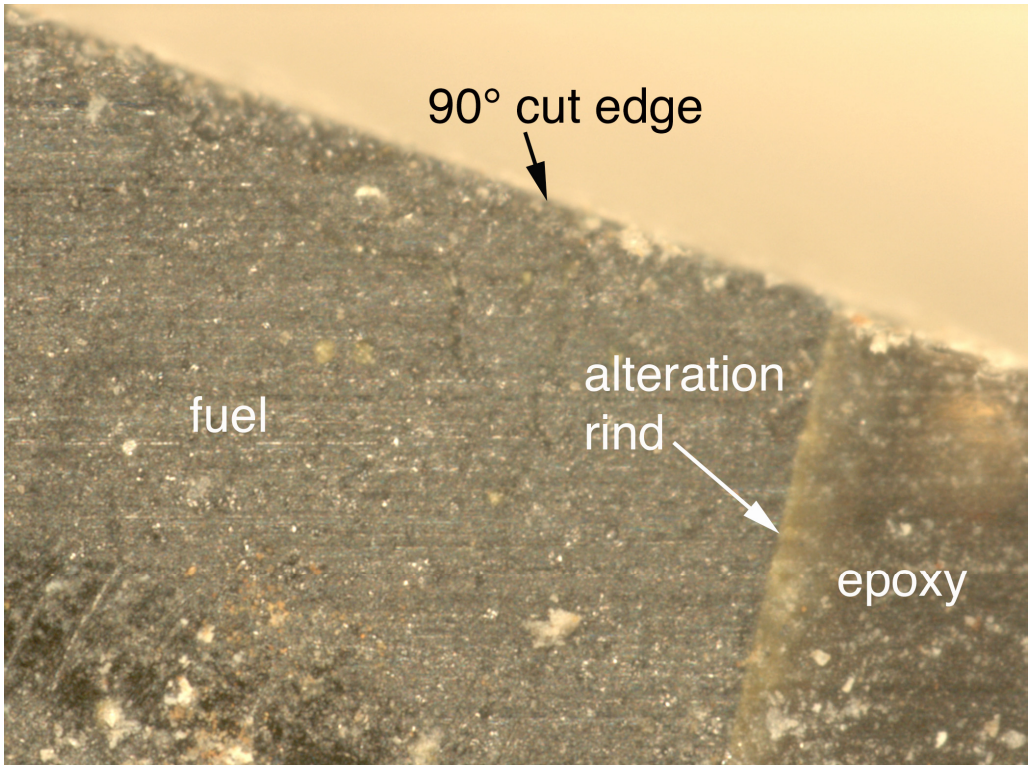

Fig. 2-3a. Detail of Cross-Sectioned Fragment of ATM-103 from a Low Drip Rate Test of 10 Years.

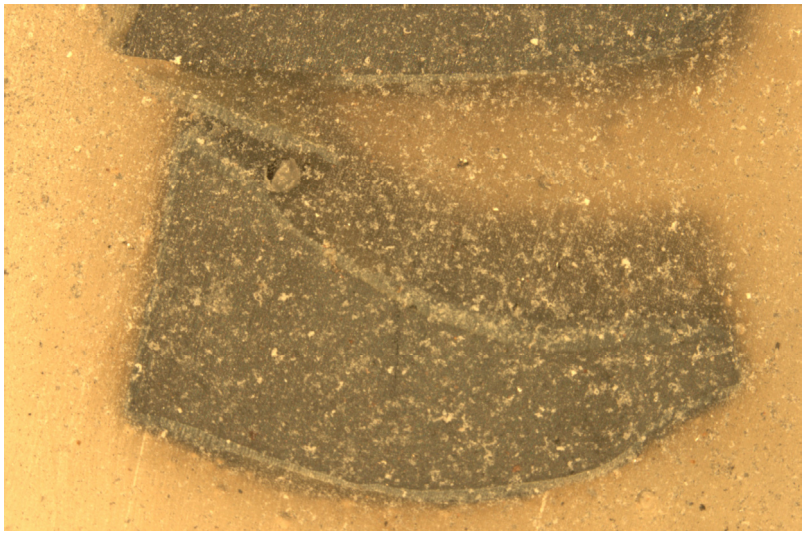

Fig. 2-3b. Cross-Sectioned Fragments of ATM-106 from High Drip Rate Test of 10 Years. The fragments are approximately 5 mm across. A more clearly defined alteration rind surrounds these fragments than was observed in the low drip rate ATM-103 fragments.

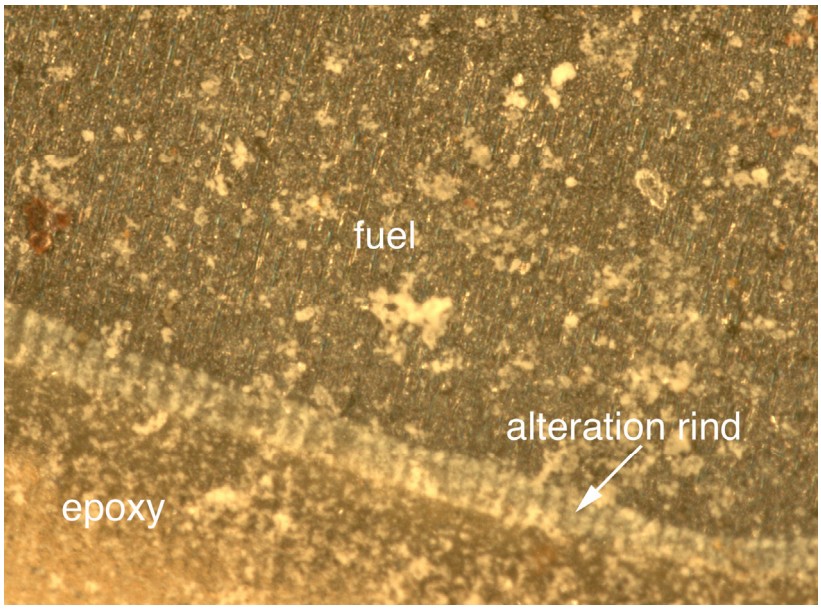

Fig. 2-3c. Detail of Cross-Sectioned Fragment of ATM-106 from High Drip Rate Test of 10 Years. Note the sharp interface between the alteration rind and the underlying fuel. Much of the light-colored material scattered across the surface is epoxy debris from the cutting wheel.

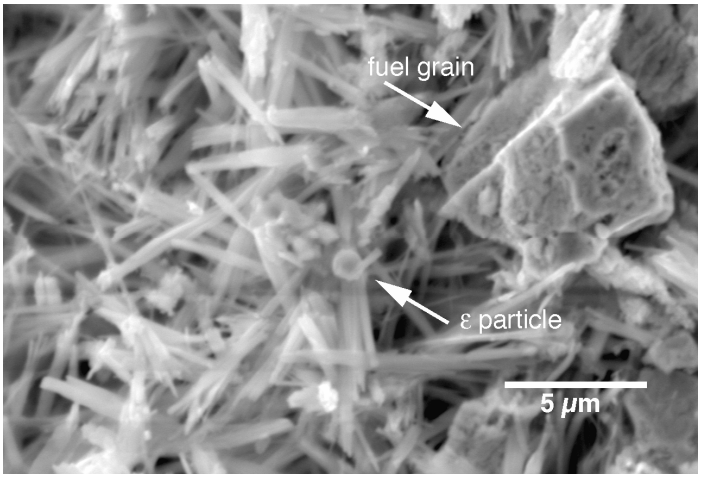

Fig. 2-4. SEM Micrograph of Material Taken from Test S62J-92. Note the presence of an epsilon particle in the center and a pitted fuel grain in the upper right.

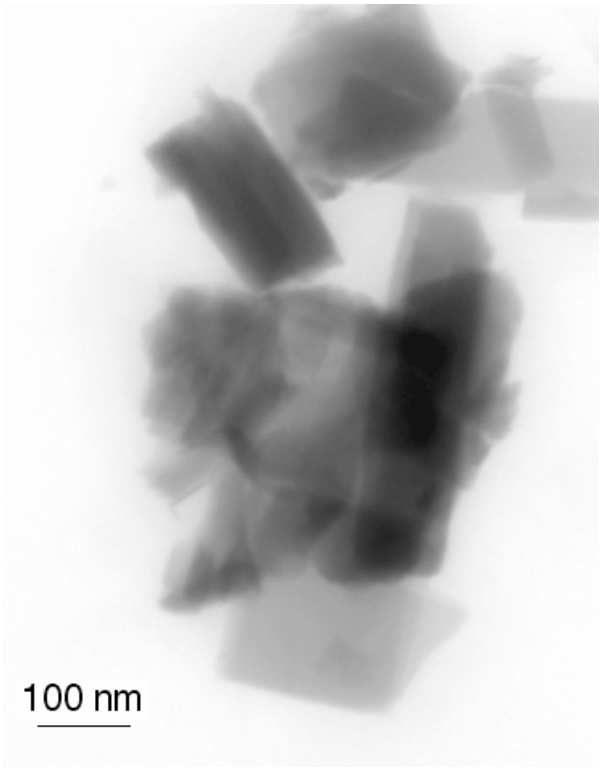

Fig. 2-5. TEM Micrograph of Crystallites from the S62J-92 Sample.

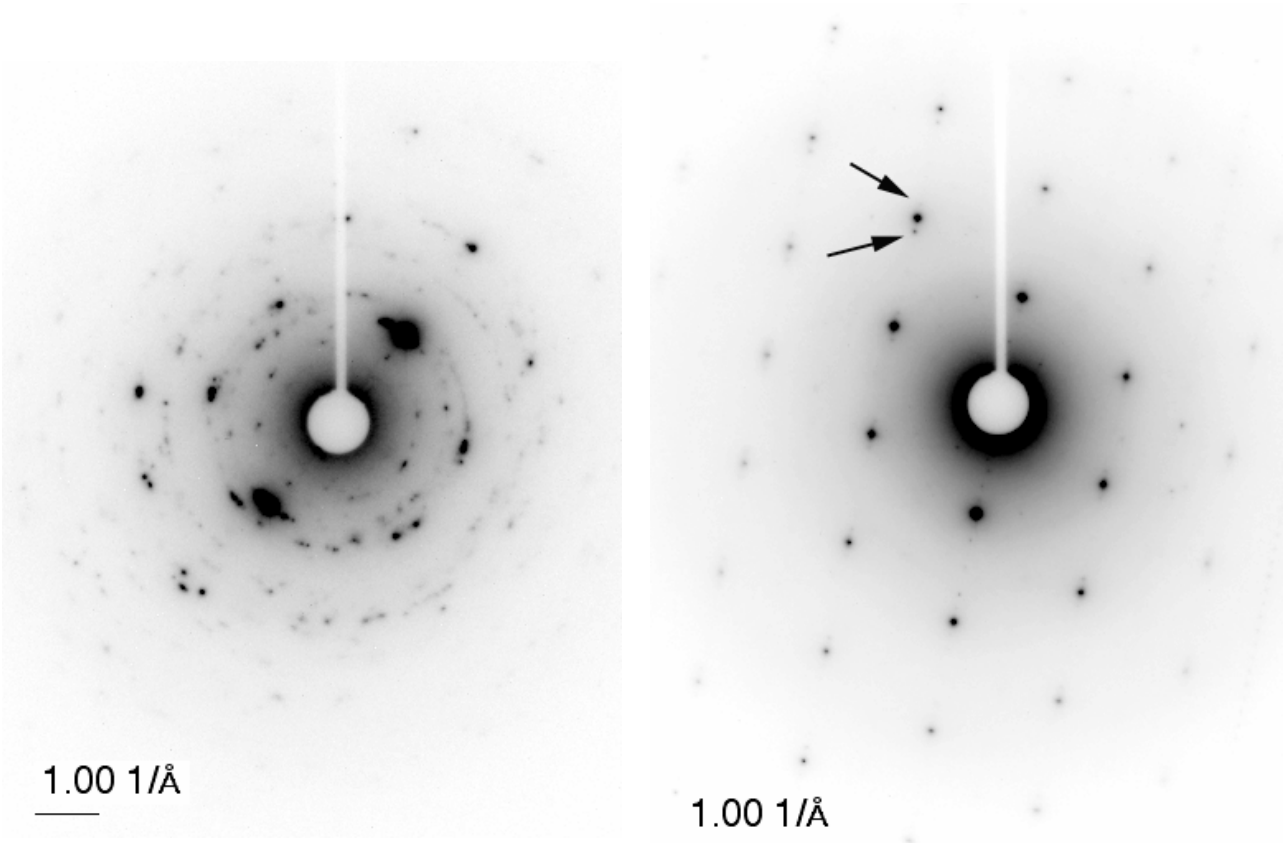

(a) (b)

Fig. 2-6. Electron Diffraction Patterns from Platy Uranium Phase from Test Sample S62J-92. These, along with 5 other patterns (not shown), are quantified in Table 2-2. Note the satellite peaks (marked with arrows) visible in the nearly zone axis pattern in (b).

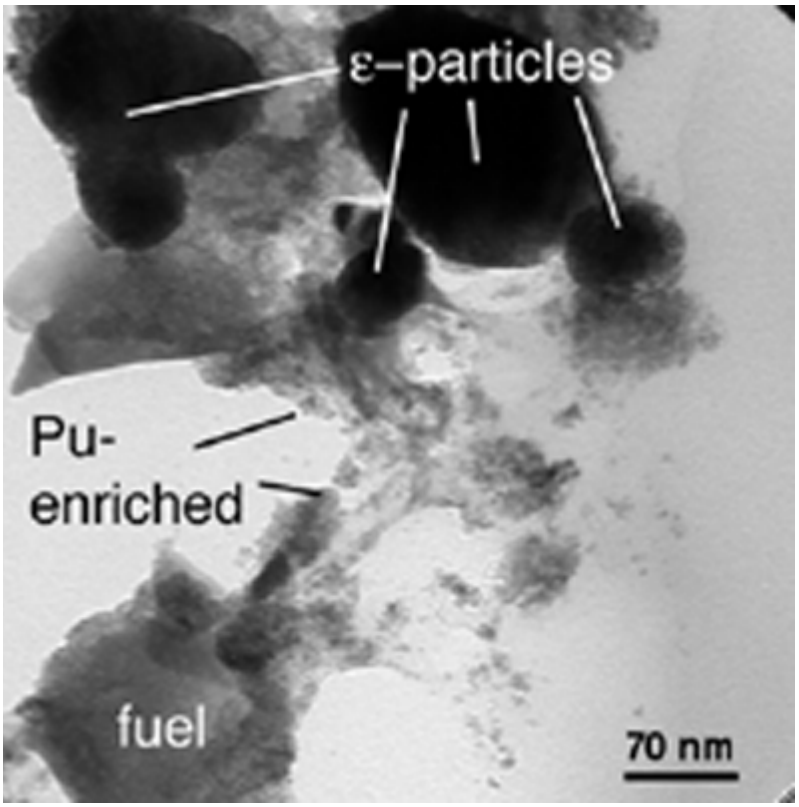

Fig. 2-7. TEM Micrograph of the Plutonium-Enriched Material with Epsilon Phase and Fuel Fragments.

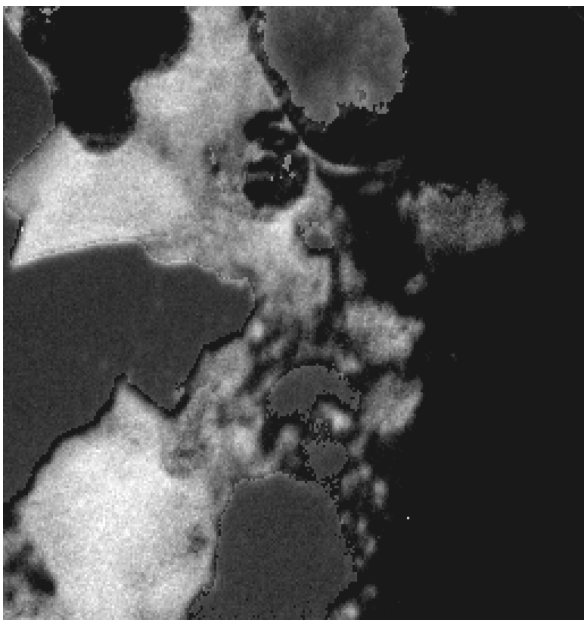

Fig. 2-8. Image-filtered TEM Micrograph of Field of View in Figure 2.7. Electrons that lost an amount of energy characteristic of U or Pu were used to form image.

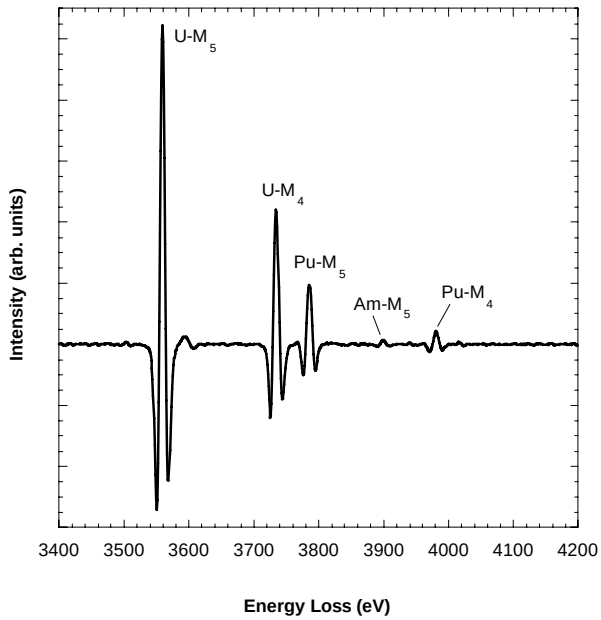

Fig. 2-9. Electron Energy Loss Spectum Showing Plutonium and Americium Enrichment. Nominally, the Pu-M_5 peak intensity would be ~1% that of the U-M_5 peak in the unaltered fuel.

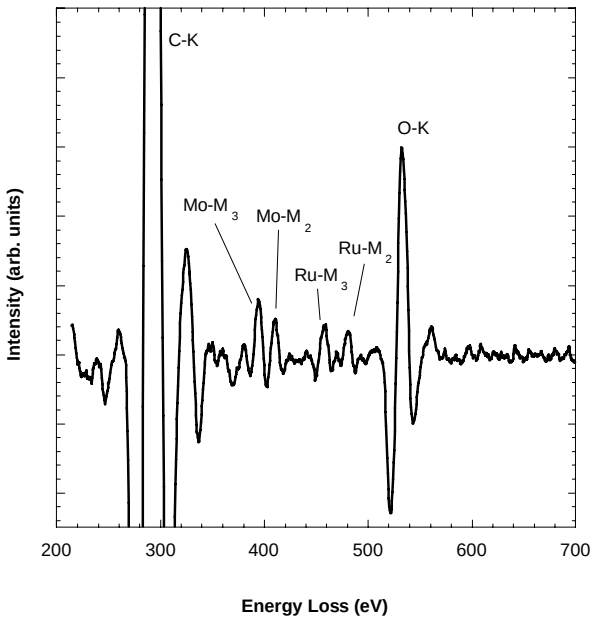

Fig. 2-10. Energy Loss Spectrum Showing the Presence of Molybdenum and Ruthenium from the Epsilon Particles. The strong carbon peak arises from the substrate film.

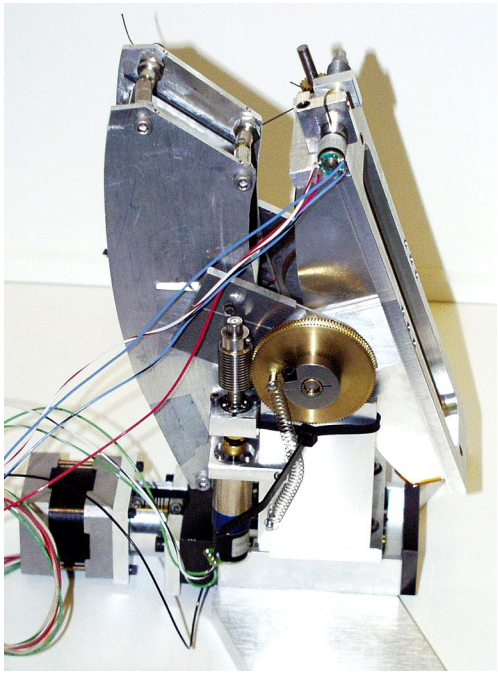

Fig. 2-11. Bent-Laue X-ray Energy Analyzer.

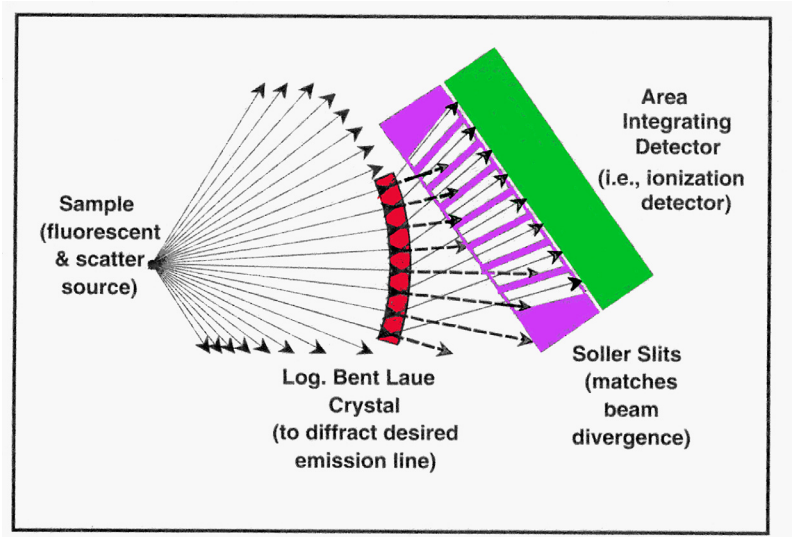

Fig. 2-12. Schematic of How a Bent-Laue Analyzer Functions. The bent silicon crystal selectively diffracts x-rays within an energy window into a detector shielded from direct illumination by soller slits.

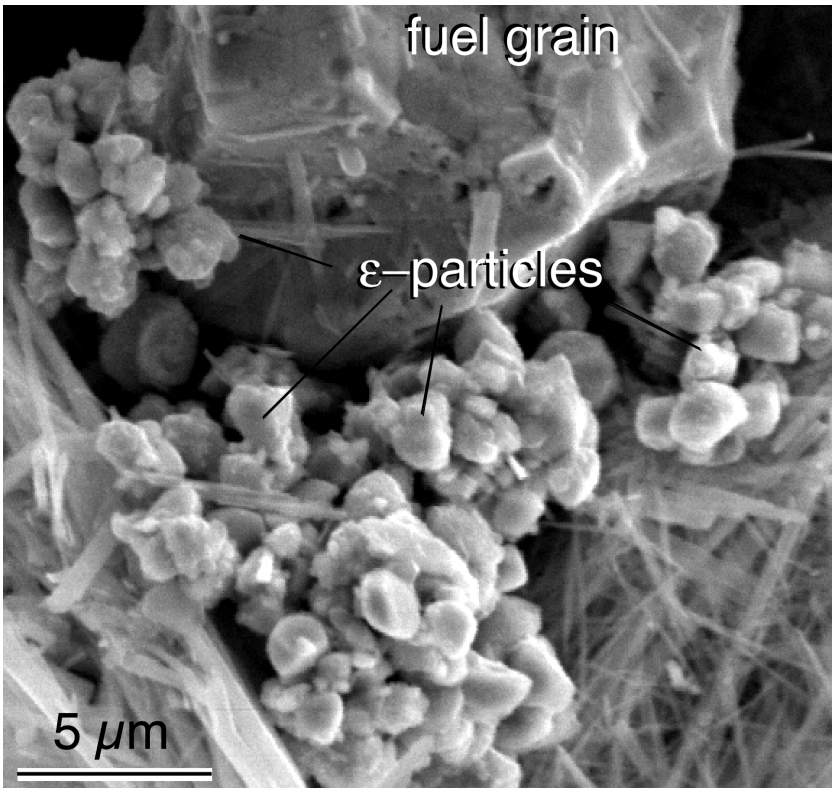

Fig. 2-13. SEM Micrograph Showing Anomalous Clustering of Epsilon Particles on Surface of Pitted Fuel Grain and Acicular Uranyl Alteration Products (likely Sodium Boltwoodite) from the High Drip Rate Unsaturated Test of ATM-106 Sampled at 104 Months.

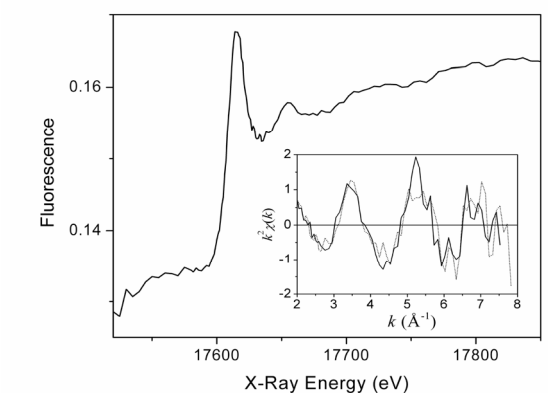

Fig. 2-14. Neptunium L_3 Edge XAS from Unaltered ATM-103, without Background Correction. Edge shape is consistent with Np(IV) oxidation state in the fuel. Inset shows EXAFS signal from two separate runs.

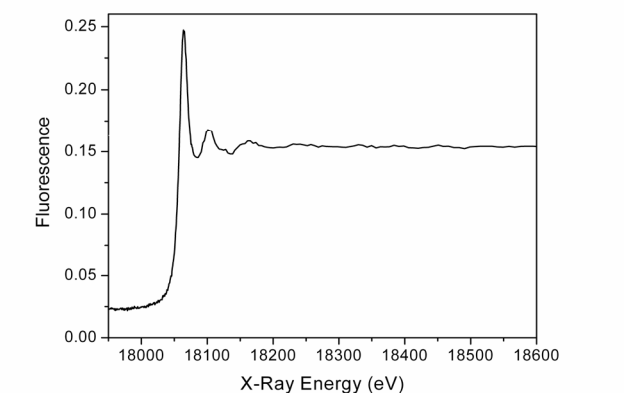

Fig. 2-15. Plutonium L_3 Edge XAS from Unaltered ATM-103. Edge shape and EXAFS (not shown) are consistent with Pu (IV) in the fluorite crystal structure of UO_2.

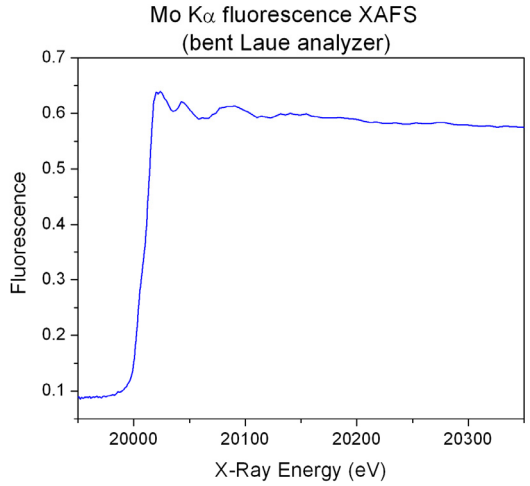

Fig. 2-16. Molybdenum K-edge XAS from ATM-103 CSNF using Bent-Laue Analyzer Detection at the APS. The molybdenum is present in the fuel at only 0.3 wt%. The ability of the Bent-Laue analyzer to resolve these weak features in the presence of a strong background makes the XAS analysis of trace elements in CSNF possible.

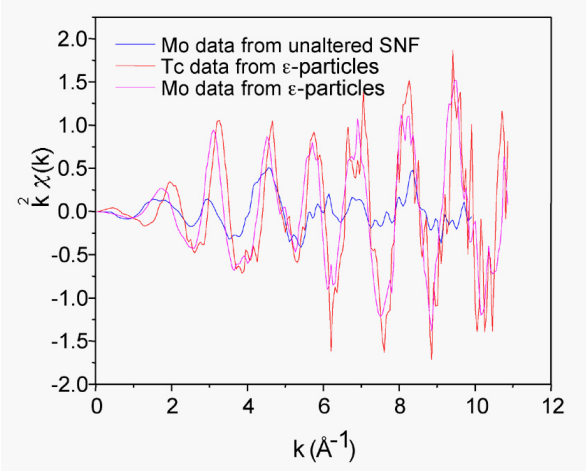

Fig. 2-17. EXAFS Measurements from Molybdenum in Bulk, Unaltered ATM-103 Fuel (Blue Line) Compared with that from Molybdenum and Technetium in Epsilon Particles that Segregated during ATM-106 Fuel Corrosion (Magenta and Orange Lines, Respectively). The EXAFS from bulk fuel is characteristic of mixed metallic and oxide molybdenum, whereas the EXAFS from epsilon phase shows molybdenum and technetium in equivalent metallic environments.

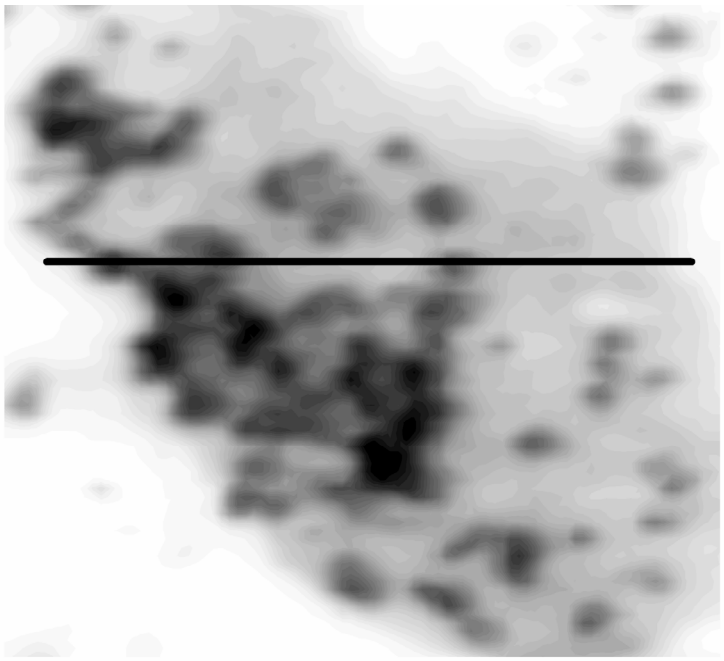

Fig. 2-18. Uranium XAS Map of S62J-104 Specimen. Darker areas are fuel grains, while gray areas are uranyl alteration phases. Horizontal line shows the location of the line scan of uranium and neptunium shown in Figure 2-19. Field of view of the image is approximately 340 x 340 µm.

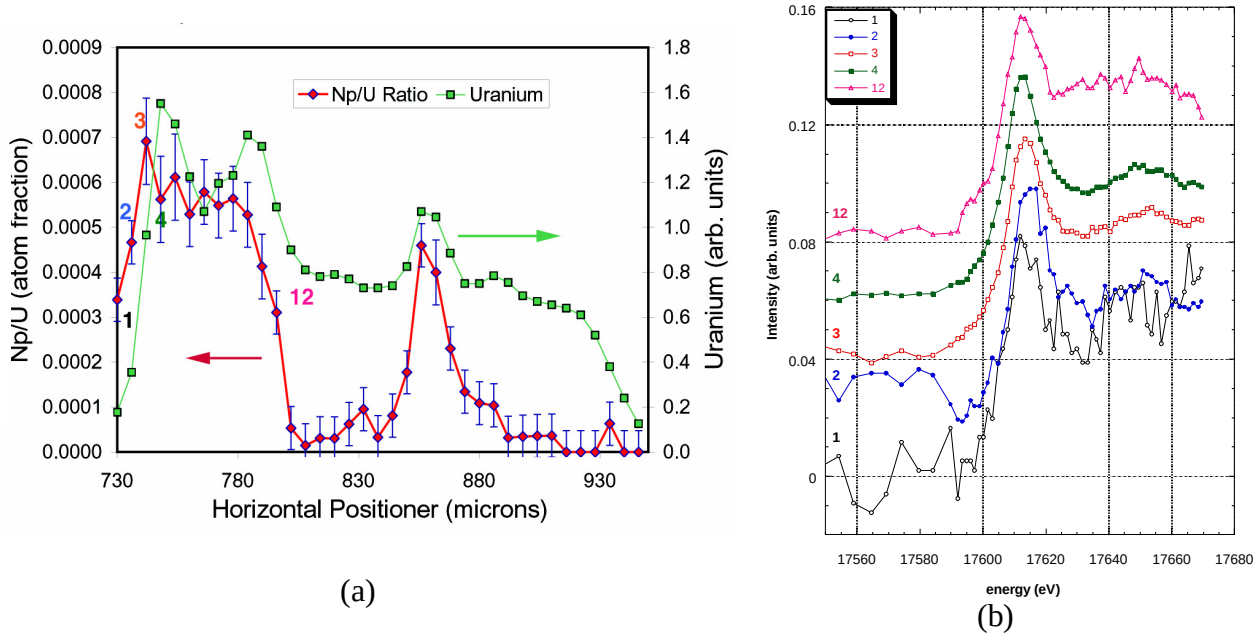

(a) (b)

Fig. 2-19. (a) Line scans showing total uranium intensity (green) and ratio of neptunium to uranium signal (red) and (b) normalized Np XAS spectra from selected points in the line scan (labeled in order as 1, 2, 3, 4, and 12).

2.4 DISCUSSION

An examination of CSNF that had undergone up to 10 years of corrosion testing has provided valuable insights into mechanisms of radionuclide release and sequestration (particularly for Np, Pu, and Tc). Corrosion fronts have been found to follow exposed geometric surfaces, with little apparent effect from grain boundary penetration. This simplifies surface area scaling estimates. The alteration rind is adherent, but appears unlikely to serve as an effective protective layer. The important radioelements technetium and plutonium have been found to remain in relatively insoluble solids during corrosion; technetium remains alloyed in noble metal particles, while plutonium resists oxidation and remains proximal to the surface of the corroding fuel. Uranyl alteration products are found to be devoid of, or at least relatively depleted in, neptunium (relative to the original fuel). This is in apparent contrast with reports of Np incorporation in certain coprecipitation experiments. These results are consistent with the hypothesis that neptunium, which is resistant to oxidation relative to uranium, is not oxidized as the fuel corrodes and behaves as if NpO_2 is the solubility-controlling phase. Although coprecipitation of Np with uranyl phases is not ruled out by this hypothesis, such a phenomenon will likely depend upon the lower rate of paragenesis that occurs when NpO_2-like solids are in contact with uranyl solids and water. Nonetheless, the evidence, albeit incomplete, is pointing toward replacement of the conservative assumption of Np_2O_5 as a solubility-limiting phase with a model based upon NpO_2.

2.5 REFERENCES

Buck, E.C., Finn, P.A., and Bates, J.K. (2004). *Micron* **35,** 235-243.

Burns, P.C. (1998). *Can. Mineral.* **36,** 1069.

Burns, P.C., Deely, K.M., and Skanthakumar, S. (2004). *Radiochim. Acta* **92,** 151-159.

Chen, Y. (2003). *Computers & Geosciences* **29**, 385-397.

Finch, R.J. (2003). *Unsaturated Testing of Bare Spent UO_2 Fuel Fragments: Data Report. YMP/SF-3A-455,* Chicago, Illinois: Argonne National Laboratory. MOL. 20040129.0324.

Finch, R.J., and Cunnane, J.C. (2001). *Proceedings of the Ninth International High-Level Radioactive Waste Management Conference*, April 29-May 3, 2001, Las Vegas, Nevada. American Nuclear Society, La Grange Park, Illinois.

Finch, R.J., Buck, E.C., Finn, P.A., and Bates, J.K. (1999). "Oxidative Corrosion of Spent UO_2 Fuel in Vapor and Dripping Groundwater at 90°C." *Scientific Basis for Nuclear Waste Management XXII, Symposium held November 30-December 4, 1998, Boston, Massachusetts, U.S.A.* (edited by D.J. Wronkiewicz and J.H. Lee) *Mat. Res. Soc. Symp. Proc.* **556,** 431-438. Warrendale, Pennsylvania: Materials Research Society. TIC: 246426.

Goldberg, M. (2003). *Rod Segment Test Data Report, CSNF Degradation Model: Q Data Input from ANL Testing.* Task Number: PAWC1M5. [Argonne, Illinois]: Argonne National Laboratory, Chemical Engineering Division. ACC: MOL.20030627.0221.

Fortner, J.A., Finch, R.J., Kropf, A.J., and Cunnane, J.C. (2004). "Re-evaluating Neptunium in Uranyl Alteration Phases from Corroded Spent Fuel. *Nuclear Technology* **148**(2), 174-180.
Goldberg, M. (2003). *Rod Segment Test Data Report, CSNF Degradation Model: Q Data Input from ANL Testing.* Task Number: PAWC1M5. (Argonne, Illinois): Argonne National Laboratory, Chemical Engineering Division. ACC: MOL.20030627.0221.

Guenther, R.J., Blahnik, D.E., Campbell, T.K., Jenquin, U.P., Mendel, J.E., Thomas, L.E., and Thornhill, C.K. (1988a). *Characterization of Spent Fuel Approved Testing Material ATM--103.* PNL-5109-103. Richland, Washington: Pacific Northwest Laboratory. ACC: NNA.19911017.0104

Guenther, R.J., Blahnik, D.E., Campbell, T.K., Jenquin, U.P., Mendel, J.E., and Thornhill, C.K. (1988b). *Characterization of Spent Fuel Approved Testing Material--ATM-106.* PNL-5109-106. Richland, Washington: Pacific Northwest Laboratory. ACC: NNA.19911017.0105.

Karanfil, C., Zhong, Z., Chapman, L.D., Fischetti, R., Bunker, G.B., Segre, C.U., and Bunker, B.A. (2000). CP521, *Synchrotron Radiation Instrumentation: SRI99: 11th U.S. National Conference,* (edited by P. Pianetta) **178** American Institute of Physics, New York.

Kropf, A.J., Finch, R.J., Fortner, J.A., Aase, S., Karanfil, C., Segre, C.U. Terry, J., Bunker, G., and Chapman, L.D. (2004). *Rev. Sci. Inst.*, **74,** 4696-4702.

Richmann, M.K., Reed, D.T., Kropf, A.J., Aase, S.B., and Lewis, M.A. (2001). *J. Nucl. Mater.* **279,** 303-312.

Soderholm, L., Antonio, M.R., Williams, C., and Wasserman, S.R. (1999). *Anal. Chem.* **71**(20), 4622-28.

Stern, E.A. (1988). *X-Ray Absorption: Principles, Applications, Techniques of EXAFS, SEXAFS, and XANES,* (edited by D.C. Koningsberger and R. Prins) Wiley-Interscience, New York.

Vaidyanathan, S. et al. (1997). "High Burnup BWR Fuel Pellet Performance," Proc. 1997 Intl. Topical Meeting on LWR Fuel Performance, 471-477.

Wronkiewicz, D.J., Bates, J.K., Gerding, T.J.,. Veleckis, E., and Tani, B.S. (1992). *J. Nucl. Mater* **190,** 107.

Wronkiewicz, D. J., Bates, J. K., Wolf, S. F. and Buck, E. C. (1996). *J. Nucl. Mater* **238,** 78.

Zhong, Z., Chapman, D., Bunker, B., Bunker, G., Fischetti, R., and Segre, C. (1999). *J. Synchrotron Rad.* **6**, 212.

3.0 DISSOLVED CONCENTRATION TESTING
(J. Jerden, Jr. and R. Finch)

The following is a progress report on experiments being performed at ANL to address the issue of mineralogical controls on neptunium solubility. The work reported here was performed under the Test Plan ANL-TP-04-004, Rev. 0, "Source Term Dissolved Concentration Limits." The objectives are:

- Identifiy and characterize phases controlling dissolved concentrations of neptunium in waters emanating from a breached waste package containing spent nuclear fuel, under expected Yucca Mountain conditions.

- Expand and refine the understanding of processes that could facilitate the incorporation of neptunium into spent fuel alteration phases (e.g., structural charge compensation by coupled substitutions and the dependence on pH and temperature).

Current performance assessment models for the repository at Yucca Mountain indicate that neptunium (Np) is one of the most important long-term contributors to dose. The current scientific basis for modeling the Np dissolved concentration limits, and the uncertainties in this scientific basis, are discussed in Section 2.1. As discussed there, a potentially important process that may control the dissolved concentration of neptunium released from corroding spent nuclear fuel is incorporation or coprecipitation into uranyl alteration phases. Separate experiments performed at Pacific Northwest National Laboratory (PNNL) and by Professor Peter Burns at The University of Notre Dame indicate that, under specific chemical conditions, neptunium may be scavenged by precipitating uranyl minerals (Friese et al. 2004a, Friese et al. 2004b, Burns et al. 2004). However, the range of conditions under which this can occur and the mechanism of neptunium uptake remain uncertain. This section describes experiments that are underway at ANL to quantify the chemical conditions under which neptunium is incorporated into alteration phases and to identify the uptake mechanism.

A primary objective of experiments discussed in this section is to expand and refine our understanding of processes that may lead to the incorporation of neptunium into spent fuel alteration phases. The experiments discussed are coprecipitation tests (identified as Task 1 in the Test Plan ANL-TP-04-004, Rev.0) that involve precipitating uranyl phases from neptunium-bearing aqueous solutions of relevant composition by base titration. These experiments differ from previous neptunium coprecipitation tests (Friese et al. 2004a, Friese et al. 2004b, Burns et al. 2004) in that they take into account other components expected to be present in seepage water (e.g., Ni^{2+} and Na^{+}) based on the output from the in-package chemistry model.

3.1 BACKGROUND

The long half life (2.14 Ma) and potential mobility of neptunium-237 (^{237}Np) in oxidizing groundwaters make it an important isotope for evaluating long-term performance of a geologic repository for high-level nuclear waste (Viswanathan et al. 1998). Performance assessment (PA) models indicate that the dose contribution from ^{237}Np may become significant after about 50,000 years (DOE 1998). This dose estimate is founded in part on the assumption that dissolved

concentrations of Np in groundwaters emanating from a breached waste package containing CSNF will be limited by the precipitation of Np_2O_5 (Efurd et al. 1998, Kaszuba and Runde 1999).

During the oxidative dissolution of spent nuclear fuels under hydrologically unsaturated conditions, as examined in unsaturated corrosion experiments (also known as the "drip tests") conducted at ANL, the release of Np to solution was approximately congruent with U (Finn et al. 1998). However, a substantial amount of U released from the dissolving fuel matrix reprecipitated on the surface of the corroded fuel (Finn et al. 1998, Finch et al. 1999), implying that a comparable fraction of Np is also either retained in the fuel or in (unidentified) precipitated solids. Congruent release of U and Np has also been reported in a number of other experiments on spent fuel dissolution, in the apparent absence of uranyl solid formation (CRWMS M&O 2000a). Furthermore, dissolved concentrations of Np in solutions recovered from ANL unsaturated tests and batch tests conducted at PNNL on spent fuels are well below the Np concentrations that might be expected if Np_2O_5 were limiting the dissolved concentration of Np. In fact, if concentrations of Np in solutions recovered from these fuel corrosion tests are representative of concentrations likely to emanate from a breached waste container with CSNF, Np-related peak radiation doses to individuals near Yucca Mountain might be several orders of magnitude lower than current estimates. Retention of Np in the unsaturated experiments with U- and Si-saturated groundwater may be caused by one or more of several factors, including:

1. Incomplete oxidation of Np(IV) in the fuel to Np(V) under experimental conditions; at least two potential mechanisms are consistent with this hypothesis.
   - Coprecipitation of Np(IV) with poorly crystalline "residue" phase(s) such as the Pu-rich layer reported by Buck et al. (2004).
   - Retention of Np(IV) in dissolving UO_2 fuel as a solid solution $(Np,U)O_2$, in which the Np content increases as alteration of the fuel proceeds (due to the preferential removal of U).
2. Coprecipitation of neptunium in U(VI) compounds.
3. Sorption of Np onto existing solids, test vessel components, or both.
4. Ion exchange of dissolved Np species (e.g., NpO_2^+) with cations in existing compounds (e.g., Na^+ in Na boltwoodite).

Total neptunium concentrations reported from the ANL unsaturated tests generally remained below the Np concentrations expected if NpO_2 was the controlling phase at atmospheric oxygen fugacity (0.2 atm). However, it should be emphasized that the partial pressure of oxygen at 90°C and ~100% RH (the prevailing conditions in the ANL unsaturated tests) is approximately 0.06 atm. NpO_2 is expected to be substantially less soluble under these conditions than it is under a more oxygen-rich atmosphere.

Recent experimental studies appear to have improved the prospect for successfully developing a defensible coprecipitation model for inclusion in performance assessment calculations, because retention of Np by precipitated uranyl solids has been reported by several authors over the past year or so (Buck et al. 2003; Burns et al. 2004, Douglas et al. 2004, Friese et al. 2004a, Friese et al. 2004b). However, the mechanism by which Np was retained in those solids (all high-specific-surface-area powders) has not been identified in any of those experiments (e.g., structural incorporation; surface-mediated sorption; precipitation of

undetected minor Np-rich phases). Identification of the retention mechanism is important in assessing the relevance of these experimental observations to long-term retention of Np in the repository.

A number of sources note that available thermodynamic data predict NpO_2 to be the stable Np-bearing solid at most redox and pH conditions expected in groundwaters at the repository horizon at Yucca Mountain (Sassani and Siegmann 1999, Efurd et al. 1998, Kaszuba and Runde 1999, CRWMS M&O 2000b, CRWMS M&O 2000c, CRWMS M&O 2000d). However, crystalline NpO_2 has not been observed to precipitate from homogeneous Np(V)-bearing aqueous solutions below approximately 250°C (Roberts et al. 2003). Because of this apparent kinetic limitation on NpO_2 formation at low temperatures, NpO_2 is currently ignored as a potential long-term solubility-limiting solid at Yucca Mountain in current performance assessment calculations.

Based on data compiled in the critical review of Np and Pu thermodynamic data recently published by the Nuclear Energy Agency (NEA OECD 2001, Table 3.1, p. 41), the reaction to form NpO_2 from Np_2O_5,

$$0.5Np_2O_5 \rightarrow NpO_2 + 0.25O_{2(gas)} \qquad (3\text{-}1)$$

may be thermodynamically favorable at atmospheric O_2 fugacity ($fO_2 \approx 0.2$ atm), with a calculated Gibbs free energy of reaction equal to -5.9 kJ mol^{-1} (±8 kJ mol^{-1}). The relatively large estimated uncertainty leaves considerable doubt as to which solid is stable under ambient atmospheric conditions. Perhaps as important is the implication that, regardless of which solid is stable thermodynamically, the driving force to convert one to the other (i.e., NpO_2 to Np_2O_5) may be quite small under expected repository-relevant conditions. During the period of elevated temperature and high humidity, even ambient atmospheric fO_2 will be quite low, on the order of 0.06 atm at 90ºC. As indicated by Equation 3-1, NpO_2 is further stabilized relative to Np_2O_5 under exposure to lower oxygen fugacity conditions.

Efurd et al. (1998) conducted solubility experiments on solids precipitated from homogeneous aqueous solutions at both low and high temperatures ("over-saturation" experiments) and examined the solids with powder x-ray diffraction (XRD). The neptunium solids synthesized were dark greenish-brown and XRD data for solids formed at low temperature (~25°C) showed only a few broad Bragg reflections, whereas solids formed at 90°C gave sharper diffraction peaks. Most diffraction peaks in the powder pattern of solids precipitated from J13 water at 90°C correspond with those of crystalline Np_2O_5 (Efurd et al. 1998, Figure 2, p. 3896). Additional diffraction lines may correspond to a crystalline compound with a diffraction pattern similar to that of schoepite ($UO_3 \bullet 2H_2O$) and possibly a solid that may resemble alpha-$UO_2(OH)_2$. The latter is a tentative identification based on a single strong diffraction peak. Although Efurd et al. concluded that they had synthesized a single hydrated Np(V) compound for which they propose a composition of $Np_2O_5 \bullet xH_2O$ (unknown value for x), there is no evidence presented in the paper to support such a claim. It seems more likely that they obtained at least two crystalline solids in their over-saturation experiments: Np_2O_5 and an unidentified Np oxyhydroxide structurally similar to schoepite.

Efurd et al. (1998) used the solids obtained in their 90°C over-saturation experiments to perform additional experiments in fresh J13 water ("under-saturation" experiments). The steady-state Np concentration reported for both the over-saturation and under-saturation experiments converge to approximately the same values for a given pH (Table 5 in Efurd et al. 1998). It is not stated in the paper whether solids from the under-saturation experiments were re-examined by XRD after the second series of experiments were concluded. Efurd et al. (1998, p. 3896) used the Np concentrations measured in J13 groundwater at 25°C to calculate an uncorrected solubility product for their precipitated solid(s) (assumed by them to have the formula $Np_2O_5 \bullet xH_2O$). At pH 6 and 7, where the hydrated NpO_2^+ ion is the predominant Np(V) species in solution, Efurd et al. reported a mean solubility product with log K_{sp} = 5.2±0.8 for the following reaction:

$$Np_2O_5 \bullet xH_2O + 2H^+ = 2NpO_2^+ + (x+1)H_2O. \quad (3\text{-}2)$$

The solubility product determined by Efurd et al. (1998), ostensibly for $Np_2O_5 \bullet xH_2O$, was subsequently cited by Kaszuba and Runde (1999) as the solubility product for anhydrous Np_2O_5, according to the reaction:

$$Np_2O_5 + 2H^+ = 2NpO_2^+ + H_2O. \quad (3\text{-}3)$$

The solubility product for this reaction can be calculated by using the Gibbs free energies of formation for Np_2O_5 and NpO_2^+ (Nuclear Energy Agency 2001, Table 3.1, p. 41). Based on the NEA data, log K_{sp} = 3.69 for the dissolution of anhydrous Np_2O_5, as given by Equation 3-3, and corresponds to an activity of NpO_2^+ for all pH values below 7 that are approximately one order of magnitude lower than those calculated from the K_{sp} reported by Kaszuba and Runde (1999) for the same reaction. This is a potentially important observation because if the concentration of Np reported by Efurd et al. (1998) is kinetically controlled by the coexistence of a stable and an unstable pair of solids, the solution concentration of Np is likely to be oversaturated with respect to the more stable compound and undersaturated with respect to the more soluble compound.

In the case of solubility control by two Np compounds, the value of the steady-state Np concentration Np_{ss} can be described by the following relation (Bethke 1996):

$$Np_{ss} = \frac{1}{\gamma_{NpO_2^+}} \times \frac{(A_S k_+)_{Np_2O_5} + (A_S k_+)_{Np-hydrate}}{(A_S k_+ / K_{SP})_{Np_2O_5} + (A_S k_+ / K_{SP})_{Np-hydrate}}, \quad (3\text{-}4)$$

where A_S and k_+ represent the surface areas and reaction-rate constants, respectively, for the two Np solids, and each K_{SP} is the corresponding equilibrium constant. Unfortunately, the reaction-rate constants and surface areas of solids in experiments reported by Efurd et al. (1998) are not known, nor is the identity of the second solid, or if it is even present. As implied in Equation 3-4, the second phase is presumably a Np-hydrate.

Based on both XRD data and solubility data reported by Efurd et al. (1998), it seems likely that the Np concentrations they measured correspond to steady-state concentrations

established by two (or more) coexisting Np solids, one of which may well be crystalline, anhydrous Np_2O_5.

Despite these uncertainties, the K_{SP} reported by Kaszuba and Runde (1999) was adopted for use in TSPA-SR (DOE 1998, CRWM M&O 2000d). Section 6.1.1 of CRWMS M&O (2000b, p. 19) states that "the solubility product derived for $Np_2O_5 \bullet xH_2O$ is used to conservatively describe the solubility of Np_2O_5, which, because it possesses fewer water molecules [*sic*], should possess lower solubility." This is an unfounded statement, as there is no *a priori* reason why an anhydrous oxide should have a lower solubility in water than an oxyhydroxide and, in fact, the opposite is commonly true. Many anhydrous oxides spontaneously form hydrated (or hydroxylated) compounds when placed in contact with water or humid air. For example, UO_3 readily alters to the hydrated uranium oxyhydroxide, schoepite, in water, because schoepite is substantially *less* soluble than anhydrous UO_3.

The NEA compendium (NEA OECD 2001) provides thermodynamic data for two forms of amorphous solid Np(V) oxyhydroxide: "fresh" and "aged" $NpO_2(OH)$, which is equivalent to $Np_2O_5 \bullet H_2O$. The Gibbs free energy of reaction for the conversion of amorphous $NpO_2(OH)$ to crystalline anhydrous Np_2O_5,

$$NpO_2(OH)_{(am,\ aged)} \rightarrow 0.5\ Np_2O_5 + 0.5H_2O, \qquad (3\text{-}5)$$

is -16 kJ mol^{-1} (± 12 kJ mol^{-1}). Crystalline Np_2O_5 is thermodynamically more stable (and therefore less soluble) than hydrated, "aged" amorphous $NpO_2(OH)$ in water, although the estimated uncertainties in the Gibbs free energies are sufficiently large that the driving force for conversion of aged $NpO_2(OH)$ to crystalline Np_2O_5 may be quite small.

Despite the efforts discussed above to better understand the stabilities of pure Np solids, no pure Np solids, including NpO_2, Np_2O_5, and $NpO_2(OH)$, have yet been identified in any experiments on spent fuel. However, Finch (2002) reported formation of NpO_2 at 150°C and 90°C following reaction of Np-doped U_3O_8 in humid air under very oxidizing conditions (i.e., with excess oxygen generated by decomposition of H_2O_2 inside stainless-steel test vessels). These are the lowest temperatures reported for the precipitation of NpO_2 from aqueous solutions (cf., Roberts et al. 2003), possibly resulting from the high surface areas of solids in those tests and the fact that Np in the starting solids was tetravalent, as it is in spent fuel (Kropf et al. 2004). Previous attempts to precipitate Np oxides from homogeneous solutions generally produced Np_2O_5; however, at higher temperatures (<250°C), Roberts et al. successfully precipitated crystalline NpO_2 from homogeneous Np(V)-bearing solutions. In the 90°C experiments reported by Finch (2002), Np_2O_5 was tentatively identified in addition to NpO_2, so that uncertainty remains regarding which solid is likely to exert long-term solubility control on Np at lower temperatures. Nevertheless, these tests provide substantial evidence that NpO_2 is the predominant Np-limiting solid likely to form in the repository. Of course, the potential catalytic effect of a solid surface on NpO_2 precipitation in laboratory tests does not change the thermodynamics of the reaction; rather, surface-mediated catalysis simply lowers the activation energy required for NpO_2 precipitation compared with that in homogeneous solution.

Substantial effort continues to be devoted to examining the potential for using Np-bearing U solids as the solubility-limiting solids for Np. A number of factors support using a coprecipitation-based solubility model to calculate dissolved Np concentrations in a breached waste package (Finch and Cunnane 2001, Chen 2003):

- Np(V) and U(VI) exhibit similar crystal-chemical behaviors (Burns et al. 1997) providing a theoretical foundation for a coprecipitation-based model.
- Under certain experimental conditions, Np has been shown to be associated with some uranyl compounds that may form during corrosion of CSNF in contact with groundwater or humid air. Although the mechanism by which Np is retained in these solids remains largely unexplained (Friese et al. 2004a, Friese et al. 2004b, Burns et al. 2004), experiments have provided empirical support (albeit rather limited) for Np sequestration by some potentially relevant U(VI) solids.
- Many uranyl minerals are known to persist in nature for hundreds of thousands of years (Finch et al. 1996).

Crystal-chemical arguments have been used to suggest that Np(V) should substitute for U(VI) in structural sites of crystalline uranyl compounds, provided that a charge-balance mechanism is available (Burns et al. 1997). Buck et al. (1998) were the first to report trace levels of Np (on the order of 0.4 wt%) in a uranium(VI) oxyhydroxide, "dehydrated schoepite" $(UO_2)O_{0.25-z}(OH)_{1.5+2z}$ $(0 < z < 0.15)$, that had formed on corroded fuel in contact with humid air (~100% RH) at 90°C. Dehydrated schoepite is structurally related to schoepite, $(UO_2)_4O(OH)_6(H_2O)_6$, and metaschoepite, $(UO_2)_4O(OH)_6(H_2O)_5$, which are the solids currently used to model limits on uranium concentrations in groundwaters considered representative of Yucca Mountain groundwater (CRWMS M&O 2000d).

The observation by Buck et al. (1998) is now acknowledged to have likely been caused by an unusual spectral interference by U (Buck et al. 2004, Fortner et al. 2004). Other recent evidence also shows that synthetic schoepite and dehydrated schoepite do not incorporate Np (Burns et al. 2004). More recent studies suggest that whereas schoepite (and related simple oxyhydroxides) may not incorporate Np, other uranyl solids may well do so (McNamara et al. 2003, Buck et al. 2004, Burns et al. 2004, Friese et al. 2004a, Friese et al. 2004b).

At the low Np concentrations believed relevant to the repository (a few hundred parts per million), Np can be considered a trace constituent in most host phases, so that Np substitution should obey Henry's law. We can estimate the Np concentration in aqueous solution by using the method described by Bruno et al. (1999), in which a Henry's law constant of one is assumed for a trace element in a solid that precipitates and dissolves congruently with respect to the major and trace elements (in this case, U and Np, respectively). The relationship between the dissolved concentration of Np and that of U is:

$$[\mathrm{Np}]_{aq} = \frac{x}{1-x}[\mathrm{U}]_{aq}, \qquad (3\text{-}6)$$

where x is the mole fraction of the trace component (Np) in a binary solid solution that is in equilibrium with a liquid, in this case (meta)schoepite in water. Equation 3-6 is used to calculate

the concentration of dissolved Np in solution by multiplying the calculated concentration of dissolved U (calculated by assuming metaschoepite-groundwater equilibrium) by the ratio x/(1-x), which is the Np:U ratio in the uranyl compound of interest.

It is well established that U(VI) oxyhydroxides tend to form early during the oxidative corrosion of UO_2, including uraninite in nature (Finch and Murakami 1999), unirradiated synthetic UO_2 (Wronkiewicz et al. 1992) and spent UO_2 fuels (Finch et al. 1999). However, in the presence of dissolved silica and other elements in J13-like groundwaters, the early-formed U(VI) oxyhydroxides are likely to dissolve, eventually altering to uranyl silicates (Finch et al. 1999). Provided sufficient dissolved silica can contact the corroding fuel – which implies sufficient groundwater flux into the waste package – the (very) long-term U(VI) solids are expected to be uranyl silicates.

Although uranyl silicates appear to be promising candidates as Np-bearing solids, no evidence has yet been found for the incorporation of Np into uranyl silicates formed in the ANL unsaturated tests with spent fuel (CRWMS M&O 2000a, Fortner et al. 2004, Section 2.3.3 of this report). One explanation for this may be that during the initial alteration of spent fuel, early formed uranyl oxyhydroxides do not incorporate Np as it is released from the fuel, so that the subsequently formed uranyl silicates–which commonly form through the replacement of preexisting uranyl oxyhydroxides (Wronkiewicz et al. 1992, 1996; Finch et al. 1999) – precipitate in the absence of available Np. Nevertheless, Np concentrations in the ANL unsaturated tests have always been well below the values expected if Np_2O_5 were limiting Np releases in those tests. A possible explanation for this result may be that Np in the fuel, present as Np(IV), is not completely oxidized in those experiments.

Thus, the identity of Np-bearing solids formed during the corrosion of fuel remains elusive. Nevertheless, substantial effort has continued toward the development of a secondary-phase model, including experimental studies attempting to incorporate Np into a variety of U(VI) solids (Friese et al. 2004a, Friese et al. 2004b, Burns et al. 2004). Unfortunately, due to the continued lack of firm evidence for incorporation of Np into the structures of any U(VI) compounds, experiments are still needed that can help establish the following:

- Identities of the most relevant U(VI) solids that are likely to sequester neptunium,
- Whether Np is incorporated into the structures of U(VI) corrosion products,
- The molar Np:U ratio (or range of Np:U ratios) in Np-bearing U(VI) corrosion products,
- The molar Np:U ratio (or range of Np:U ratios) in solutions in contact with Np-bearing U(VI) corrosion products,
- The limit of Np concentrations in U(VI) compounds under repository-relevant conditions, and
- The fate of Np during the alteration of early-formed U(VI) corrosion products as they continue to interact with in-package aqueous solutions and Yucca Mountain groundwaters.

Although necessary for model development, such information is essentially qualitative. In order to quantify and model dissolved Np concentrations likely to be controlled by the solubilities of Np-bearing solid corrosion products (if they exist), the following quantitative data are needed for each potentially relevant Np-bearing solid (CRWMS M&O 2000a):

- The solubilities and thermodynamic stabilities in the water chemistries expected in the repository,
- Equilibrium partitioning of Np between relevant solids and aqueous solutions (Henry's Law behavior) as a function of solution chemistry, and possibly as a function of solid chemistry as well, and
- Precipitation and dissolution rates for all relevant Np-bearing solids (kinetic rate laws).

It is clear that the research effort required to quantify how Np-bearing U(VI) solids will limit dissolved Np concentrations is daunting. However, it will not be possible to implement into PA a defensible solid-solution model for Np solubility limits without this information. Strictly empirical evidence that radionuclides are associated with U(VI) solids under select experimental conditions provides little confidence that these same solids will limit Np mobility over repository-relevant time scales.

3.2 PROCEDURES

The experiments discussed in this report are coprecipitation tests (identified as Task 1 in the Test Plan ANL-TP-04-004, Rev. 0). These tests approach the issue of neptunium incorporation into alteration phases from a solution perspective and involve methods similar to those used in coprecipitation tests of Quinones et al. (2001). They involve precipitating uranyl phases from neptunium-bearing aqueous solutions of relevant composition, by base titration.

These tests focus on how pH and the presence of the cations Na^+ and Ni^{2+} influence the coprecipitation of neptunium with uranyl precipitates. These two cations were chosen because the in-package chemistry model predicts that nickel will be one of the dominant dissolved species (>0.1 molal) supplied by degradation of waste package internal components and sodium will be one of the dominant dissolved species for scenarios in which seepage waters enter the waste package. Nickel was included in all of the experiments reported here. Future tests are planned in which nickel is not present to verify its role in the precipitation process. In brief, the experiments discussed in this report involved first making an acidic (nitric matrix) solution of uranium, neptunium, and nickel in proportions relevant to a breached waste package, then increasing the solution pH until the solution became oversaturated with respect to uranyl oxide hydrates, such as schoepite. Two different bases were used to bring the experimental solutions to supersaturation: (1) sodium hydroxide and (2) tris(hydroxymethyl)aminomethane (tris). The tris buffer was used because it contains no sodium. Therefore, comparing results from experiments using these two bases will help differentiate the role that sodium plays in the uptake of neptunium by the precipitating solids from the effect of the pH.

The following list is a step-by-step account of how the coprecipitation experiments discussed in this report were performed:

Starting Solutions

(a) A neptunium stock solution was obtained. This source stock solution was diluted with deionized water (DIW).

(b) A uranium stock solution was obtained by dissolving uranium oxide powder. This source stock solution was diluted with DIW.

(c) A nickel stock solution was obtained by dissolving nickel oxide powder. This source stock solution was diluted with DIW.

(d) These stock solutions were mixed in desired proportions in 30-mL polypropylene copolymer centrifuge tubes. The pH of these solutions was measured using pH paper. The samples were mixed by shaking the centrifuge tubes intermittently (every hour) over an approximately 8-hour period. At the end of this period, 2-mL aliquots of each mixed sample were taken, filtered, and submitted for inductively coupled plasma-mass spectrometry (ICP-MS) analyses. A small volume of dilute base (<1 mL) was added to each aliquot to prepare the aliquot for analyses. The results of the analyses are shown in Table 3-1.

Precipitation and Sampling

(e) The pH of the mixed samples was adjusted to target values near 4.5 or 8.5 using either sodium hydroxide or tris(hydroxymethyl)aminomethane (tris). The final pH values (after precipitation) and the volume of base that were used for each sample are presented in Table 3-2.

(f) The pH-adjusted samples were sealed in high-density polyethylene vessels and placed in a temperature-controlled oven at 90^{o}C. The samples were shaken 5 times daily throughout the reaction period.

(g) The samples were reacted for 9 days at 90^{o}C. At the end of the reaction period, the samples were cooled and the final pH was measured. The supernatant was centrifuge filtered, acidified, and submitted for ICP-MS analyses. The final pH values and dissolved concentrations in molal units (corrected for dilution) are presented in Table 3-3.

(h) The precipitates from these tests were rinsed with 1 molar acetic acid and DIW in an effort to removed sorbed neptunium. Characterization of the solids from these tests is ongoing and will be presented in future reports.

3.2.1 Data Analysis

The dissolved concentrations of the analyte elements are reported by the ICP-MS analyst in parts per billion (ppb), which is equivalent to µg of the analyte per kg of solution (µg/kg). Analyses of the data involved adjusting for dilutions, converting to molal units, then calculating the percent of each element removed from solution by the precipitation process.

The dilution factors and dilution correction calculations can be reproduced from the data presented in Tables 3-1 and 3-2. The results of unit conversion to molal and percent uptake are presented in Table 3-3. Dilution corrections were made using the following relationship:

$$C_o = C_m\left(\frac{M_m}{M_o}\right), \tag{3-7}$$

where C_o and C_m are the concentrations in the original solution (prior to dilution) and final solution (measured concentration in diluted sample), respectively. M_o and M_m are the total sample masses of the original solution and diluted solution, respectively.

The term "uptake" is used to indicate the amount of a given element that is removed from the aqueous phase, and could include lattice incorporation or adsorption processes. The percent of a given analyte that was removed from solution (generally referred to as percent uptake) was calculated as follows:

$$\text{Uptake (\%)} = \left(\frac{C_i - C_f}{C_i}\right) x\,100 \tag{3-8}$$

where C_i and C_f are the concentrations of the analyte in the initial solution (prior to pH adjustment) and final solution (following precipitation), respectively.

3.2.2 Accuracy and Precision

The ICP-MS analyses were performed using a QA-compliant procedure that calls for the use of certified calibration and control standards and the determination of quantitation limits for each set of runs. Only concentration values exceeding the limit of quantitation (based on blank runs) are reported. The uranium and nickel concentrations were determined by analysis of a single isobar free isotope and assuming that the element has a natural isotopic composition. This is a fully quantitative method and the estimated uncertainty for these data is ±10% based on quality control samples that are analyzed with the unknowns. The neptunium concentrations are quantified using a single standard analysis method that does not include a correction for isobaric interferences. However, isobaric interference is not a problem for the samples from these experiments because neptunium is the only mass 237 nuclide present. The accuracy of the semiquantitative analyses are improved by running a quality control sample containing a nuclide with a mass ±10 amu of the unknown. For the present analyses, a U-238 standard was analyzed to determine the accuracy of the Np-237 concentrations. Based on this method, the accuracy of the neptunium concentration measurements is determined to be ±20%.

3.3 RESULTS

During titration of all sample solutions [step (e) above], it was noted that the solution was instantaneously clouded by the precipitation of either a yellow or orange-yellow solid when the pH reached approximately 4, regardless of whether sodium hydroxide or tris was used. The precipitates that formed have not yet been fully characterized; however, based on the color and solution conditions, it is likely that they are uranyl oxide hydrates.

The dissolved concentrations of uranium, neptunium, and nickel were measured before and after the pH adjustments. For some samples, the precipitation process results in a substantial

decrease in the dissolved concentration of neptunium in the solution sample; however, in other cases the neptunium concentration is unaffected. The decrease in dissolved neptunium associated with precipitation is reported here as percent uptake (i.e., uptake by the solid precipitate). The general term "uptake" is used because it is not yet known if the process that removed the neptunium from solutions in these experiments involved lattice substitution into the precipitating phase or adsorption onto its surface, or both. Future work will focus on determining the uptake mechanism.

The starting solutions contained a uranium-to-nickel ratio of approximately 1 and uranium-to-neptunium ratios of ~15, ~25, and ~85, as well as four samples with no neptunium (Table 3-3). The initial concentrations of uranium and nickel varied from $10^{-2.3}$ to $10^{-2.5}$ molal. The initial concentration of neptunium (in neptunium-bearing samples) varied from $10^{-3.5}$ to $10^{-4.3}$ molal. The initial concentrations of sodium (in sodium-bearing samples) varied from $10^{-1.1}$ to $10^{-1.5}$ molal.

The solution compositions following precipitation are shown as a function of pH in Figure 3-1. The uranium final concentration is dependent on pH, varying from 10^{-3} molal at a pH of 4.4 to 10^{-6} molal at a pH of 7 to 10^{-4} molal at a pH of 8. There is an outlier data point at the highest pH that does not fit the general trend (the concentration is lower than expected). This outlier may reflect incomplete equilibration with atmospheric carbon dioxide at this relatively high pH. The neptunium concentrations following precipitation vary from $10^{-3.6}$ to $10^{-5.5}$ molal and show no systematic dependence on pH or the uranium-to-neptunium ratio. Nickel concentrations following precipitation are mostly around $10^{-2.6}$ molal with a few samples as low as 10^{-4} molal.

Figure 3-2 shows the percent of each element removed from solution by precipitation (calculated using Equation 3-8). The removal of uranium from solution is greater than 90% at pH values greater than 5, with two samples near 70% at pH 4.4. This is consistent with the known solubility of uranyl oxide hydrates such as metaschoepite. The percentage of neptunium removed from solution due to precipitation is greater than 80% for samples titrated with sodium hydroxide to pH values greater than 7. Samples titrated to similar pH values with tris show neptunium uptakes of less than 40%. This suggests that sodium, which is not present in the tris-titrated samples but is available in the NaOH-titrated samples, plays an important role in the neptunium uptake process. This observation is consistent with the hypothesis that sodium is providing charge compensation that facilitates incorporation of neptunium into the structure of the precipitating uranyl oxide hydrate.

It is likely, based on crystal chemical arguments, that neptunium is incorporated into the precipitating phase by substituting for uranium in the crystal structure. In oxygen-saturated fluids with pH >2 (such as those used in these experiments and predicted to be present in the repository), neptunium will be present as Np(V), which forms the $[NpO_2]^+$ ion with a geometry similar to the uranyl ion $[UO_2]^{2+}$. Thus, if Np(V) substitutes for U(VI) in the uranyl minerals, charge compensation could be accomplished by cations such as sodium being incorporated into the interlayer site in the uranyl oxide hydrate structure. If the sodium charge compensation mechanism limits the amount of neptunium that can be incorporated into the precipitating phases, this would explain why samples titrated to pH values less than 7 show lower neptunium

uptakes than samples titrated to higher pH values: more sodium is made available so the precipitating phases are able to incorporate more neptunium. The uptake of neptunium was found to be insensitive to the ratio of uranium-to-neptunium ratio in the starting solution (see Figure 3-1, where the U:Np ratio is given next to each data point).

Nickel uptake does not show a consistent pH dependence; however, some of the highest uptakes occur in high pH samples. The solids produced from these high pH samples include minor amounts of a green mineral in addition to the yellow precipitate. This green mineral could be a nickel oxide or hydroxide. Future work will focus on the solids characterization for these tests.

Table 3-1. ICP-MS Data and Dilutions for Test Solutions Prior to Precipitation

Sample ID[a]	CpU-Ni(a)	CpU-Ni(b)	CpU-Ni[c]	CpU-Ni(d)	CpNpU25-Ni(a)	CpNpU25-Ni(b)	CpNpU25-Ni[c]	CpNpU25-Ni(d)
Concentrations reported by analyst (C_f in Equation 2-8)								
Ni (µg/kg)	2.03E+05	2.24E+05	2.04E+05	2.12E+05	2.13E+05	1.62E+05	2.14E+05	2.12E+05
U (µg/kg)	8.61E+05	8.48E+05	8.27E+05	8.58E+05	7.16E+05	5.61E+05	7.35E+05	7.28E+05
Np (µg/kg)	----	----	----	----	5.21E+04	3.69E+04	5.31E+04	5.01E+04
Dilutions								
Original Sample (g)	2.00	2.00	2.00	2.00	2.00	2.00	2.00	2.00
Diluted Sample (g)	2.48	2.65	2.60	2.71	2.58	2.71	2.66	2.70
Concentrations corrected for dilution (C_i in Equation 2-8)								
Ni (µg/kg)	2.52E+05	2.97E+05	2.65E+05	2.87E+05	2.75E+05	2.20E+05	2.85E+05	2.86E+05
U (µg/kg)	1.07E+06	1.12E+06	1.08E+06	1.16E+06	9.24E+05	7.60E+05	9.78E+05	9.83E+05
Np (µg/kg)	----	----	----	----	6.72E+04	5.00E+04	7.06E+04	6.76E+04

Table 3-1. **(**Continued)

Sample ID[a]	CpNpU50-Ni(a)	CpNpU50-Ni(b)	CpNpU50-Ni[c]	CpNpU50-Ni(d)	CpNpU100-Ni(a)	CpNpU100-Ni(b)	CpNpU100-Ni[c]	CpNpU100-Ni(d)
Concentrations reported by analyst (C_f in Equation 2-8)								
Ni (µg/kg)	2.00E+05	1.97E+05	1.93E+05	2.00E+05	2.01E+05	2.03E+05	2.10E+05	2.14E+05
U (µg/kg)	7.54E+05	7.97E+05	8.30E+05	7.80E+05	8.29E+05	8.35E+05	8.22E+05	8.31E+05
Np (µg/kg)	3.10E+04	2.79E+04	3.00E+04	2.92E+04	9.88E+03	9.31E+03	9.87E+03	9.98E+03
Dilutions								
Original Sample (g)	2.00	2.00	2.00	2.00	2.00	2.00	2.00	2.00
Diluted Sample (g)	2.73	2.80	2.74	2.66	2.69	2.72	2.80	2.81
Concentrations corrected for dilution (C_i in Equation 2-8)								
Ni (µg/kg)	2.73E+05	2.76E+05	2.64E+05	2.66E+05	2.70E+05	2.76E+05	2.94E+05	3.01E+05
U (µg/kg)	1.03E+06	1.12E+06	1.14E+06	1.04E+06	1.12E+06	1.14E+06	1.15E+06	1.17E+06
Np (µg/kg)	4.23E+04	3.91E+04	4.11E+04	3.88E+04	1.33E+04	1.27E+04	1.38E+04	1.40E+04

[a]Sample ID uniquely identifies the sample throughout the experimental and analytical processes (used for data tracking purposes).

Table 3-2. ICP-MS Data and Dilutions for Test Solutions after Precipitation

Sample ID[a]	jCpU-Ni(a1)	jCpU-Ni(b1)	jCpU-Ni(c1)	jCpU-Ni(d1)	jCpNpU25-Ni(a1)	jCpNpU25-Ni(b1)	jCpNpU25-Ni(c1)	jCpNpU25-Ni(d1)
Concentrations reported by analyst (C_f in Equation 2-8)								
Ni (µg/kg)	1.61E+05	2.47E+03	1.37E+05	1.58E+05	1.47E+05	1.14E+05	9.15E+04	1.43E+05
U (µg/kg)	4.80E+03	1.71E+02	1.93E+04	3.14E+05	1.71E+04	7.70E+02	3.95E+02	1.52E+04
Np (µg/kg)	----	----	----	----	4.30E+03	4.76E+04	4.67E+04	5.03E+04
Base Dilutions	**NaOH**	**NaOH**	**Tris**	**Tris**	**NaOH**	**NaOH**	**Tris**	**Tris**
Original Sample (g)	26.04	26.5	26.17	25.89	25.9	26.11	26.33	26.53
Diluted Sample (g)	26.94	28.61	28.09	26.77	27.94	26.87	27.43	28.80
Concentrations corrected for dilution (C_i in Equation 2-8)								
Ni (µg/kg)	1.67E+05	2.67E+03	1.47E+05	1.63E+05	1.59E+05	1.17E+05	9.53E+04	1.55E+05
U (µg/kg)	4.97E+03	1.85E+02	2.07E+04	3.25E+05	1.84E+04	7.93E+02	4.12E+02	1.65E+04
Np (µg/kg)	----	----	----	----	4.64E+03	4.90E+04	4.87E+04	5.46E+04

Table 3-2. (Continued)

Sample ID[a]	jCpNpU50-Ni(a1)	jCpNpU50-Ni(b1)	jCpNpU50-Ni(c1)	jCpNpU50-Ni(d1)	jCpNpU100-Ni(a1)	jCpNpU100-Ni(b1)	jCpNpU100-Ni(c1)	jCpNpU100-Ni(d1)
Concentrations reported by analyst (C_f in Equation 2-8)								
Ni (µg/kg)	1.12E+05	3.88E+03	1.49E+05	1.31E+05	1.58E+05	3.49E+02	1.62E+05	1.45E+05
U (µg/kg)	1.56E+03	2.67E+02	3.15E+05	1.19E+04	1.42E+04	4.74E+02	4.10E+05	1.46E+04
Np (µg/kg)	2.95E+04	7.23E+03	3.27E+04	2.56E+04	1.14E+04	6.42E+02	1.11E+04	8.58E+03
Base Dilutions	**NaOH**	**NaOH**	**Tris**	**Tris**	**NaOH**	**NaOH**	**Tris**	**Tris**
Original Sample (g)	25.99	26.19	26	26.01	25.84	26.07	26.31	26.03
Diluted Sample (g)	26.94	28.17	26.79	27.99	26.75	28.35	27.17	28.25
Concentrations reported by analyst (C_f in Equation 2-8)								
Ni (µg/kg)	1.16E+05	4.17E+03	1.54E+05	1.41E+05	1.64E+05	3.80E+02	1.67E+05	1.57E+05
U (µg/kg)	1.62E+03	2.87E+02	3.25E+05	1.28E+04	1.47E+04	5.15E+02	4.23E+05	1.58E+04
Np (µg/kg)	3.06E+04	7.78E+03	3.37E+04	2.76E+04	1.18E+04	6.98E+02	1.15E+04	9.31E+03

[a]Sample ID uniquely identifies the sample throughout the experimental and analytical processes (used for data tracking purposes).

Table 3-3. Results of Coprecipitation Tests[a]

Initial solutions (prior to precipitation)								
Sample ID[b]	**CpU-Ni(a)**	**CpU-Ni(b)**	**CpU-Ni[C]**	**CpU-Ni(d)**	**CpNpU25-Ni(a)**	**CpNpU25-Ni(b)**	**CpNpU25-Ni[c]**	**CpNpU25-Ni(d)**
Initial pH	<2	<2	<2	<2	<2	<2	<2	<2
Base	NaOH	NaOH	Tris	Tris	NaOH	NaOH	Tris	Tris
Ni (molal)	4.29E-03	5.06E-03	4.52E-03	4.89E-03	4.68E-03	3.74E-03	4.85E-03	4.88E-03
U (molal)	4.49E-03	4.72E-03	4.52E-03	4.88E-03	3.88E-03	3.19E-03	4.11E-03	4.13E-03
Np (molal)	**----**	**----**	**----**	**----**	2.84E-04	2.11E-04	2.98E-04	2.85E-04
Na	3.34E-02	7.38E-02	----	----	7.29E-02	2.84E-02	----	----
U/Np	**----**	**----**	**----**	**----**	14	15	14	14
U/Ni	1.0	0.9	1.0	1.0	0.8	0.9	0.8	0.8

Final solutions (after precipitation)								
	jCpU-Ni(a1)	**jCpU-Ni(b1)**	**jCpU-Ni(c1)**	**jCpU-Ni(d1)**	**jCpNpU25-Ni(a1)**	**jCpNpU25-Ni(b1)**	**jCpNpU25-Ni(c1)**	**jCpNpU25-Ni(d1)**
Final pH	5.2	7.2	7.8	4.4	8	6.2	6.6	7.8
Ni (molal)	2.84E-03	4.54E-05	2.51E-03	2.78E-03	2.70E-03	2.00E-03	1.62E-03	2.65E-03
U (molal)	2.09E-05	7.76E-07	8.70E-05	1.36E-03	7.75E-05	3.33E-06	1.73E-06	6.93E-05
Np (molal)	**----**	**----**	**----**	**----**	1.96E-05	2.07E-04	2.05E-04	2.30E-04
Percent Uptake								
Ni	33.8	99.1	44.5	43.1	42.3	46.5	66.5	45.7
U	99.5	99.9	98.0	72.0	98.0	99.9	99.9	98.3
Np	**----**	**----**	**----**	**----**	93.1	2.0	31.1	19.2

Table 3-3. (Continued)

Initial solutions (prior to precipitation)								
Sample ID[b]	**CpNpU50-Ni(a)**	**CpNpU50-Ni(b)**	**CpNpU50-Ni[c]**	**CpNpU50-Ni(d)**	**CpNpU100-Ni(a)**	**CpNpU100-Ni(b)**	**CpNpU100-Ni[c]**	**CpNpU100-Ni(d)**
Initial pH	<2	<2	<2	<2	<2	<2	<2	<2
Base	NaOH	NaOH	Tris	Tris	NaOH	NaOH	Tris	Tris
Ni (molal)	4.65E-03	4.70E-03	4.51E-03	4.53E-03	4.61E-03	4.70E-03	5.01E-03	5.12E-03
U (molal)	4.32E-03	4.69E-03	4.78E-03	4.36E-03	4.68E-03	4.77E-03	4.83E-03	4.91E-03
Np (molal)	1.79E-04	1.65E-04	1.73E-04	1.64E-04	5.61E-05	5.34E-05	5.83E-05	5.92E-05
Na	3.53E-02	7.04E-02	----	----	3.38E-02	8.05E-02	----	----
U/Np	24	28	28	27	84	89	83	83
U/Ni	0.9	1.0	1.1	1.0	1.0	1.0	1.0	1.0

Final solutions (after precipitation)								
	jCpNpU50-Ni(a1)	**jCpNpU50-Ni(b1)**	**jCpNpU50-Ni(c1)**	**jCpNpU50-Ni(d1)**	**jCpNpU100-Ni(a1)**	**jCpNpU100-Ni(b1)**	**jCpNpU100-Ni(c1)**	**jCpNpU100-Ni(d1)**
Final pH	6	7.2	4.4	7.6	5	8.2	4.4	7.8
Ni (molal)	1.98E-03	7.11E-05	2.62E-03	2.40E-03	2.79E-03	6.47E-06	2.85E-03	2.68E-03
U (molal)	6.79E-06	1.21E-06	1.36E-03	5.38E-05	6.17E-05	2.17E-06	1.78E-03	6.66E-05
Np (molal)	1.29E-04	3.28E-05	1.42E-04	1.16E-04	4.98E-05	2.95E-06	4.84E-05	3.93E-05
Percent Uptake								
Ni	57.4	98.4	41.9	47.0	39.5	99.8	43.0	47.6
U	99.8	99.9	71.4	98.7	98.6	99.9	63.2	98.6
Np	27.7	80.0	18.0	29.0	11.2	94.4	17.0	33.5

[a]The solution concentrations prior to precipitation (initial) and after precipitation (final) were calculated from the dilution-corrected ICP-MS data shown in Tables 3-1 and 3-2. The Percent Uptake was calculated with Equation 3-8.
[b]Sample ID uniquely identifies the sample throughout the experimental and analytical processes (used for data tracking purposes).

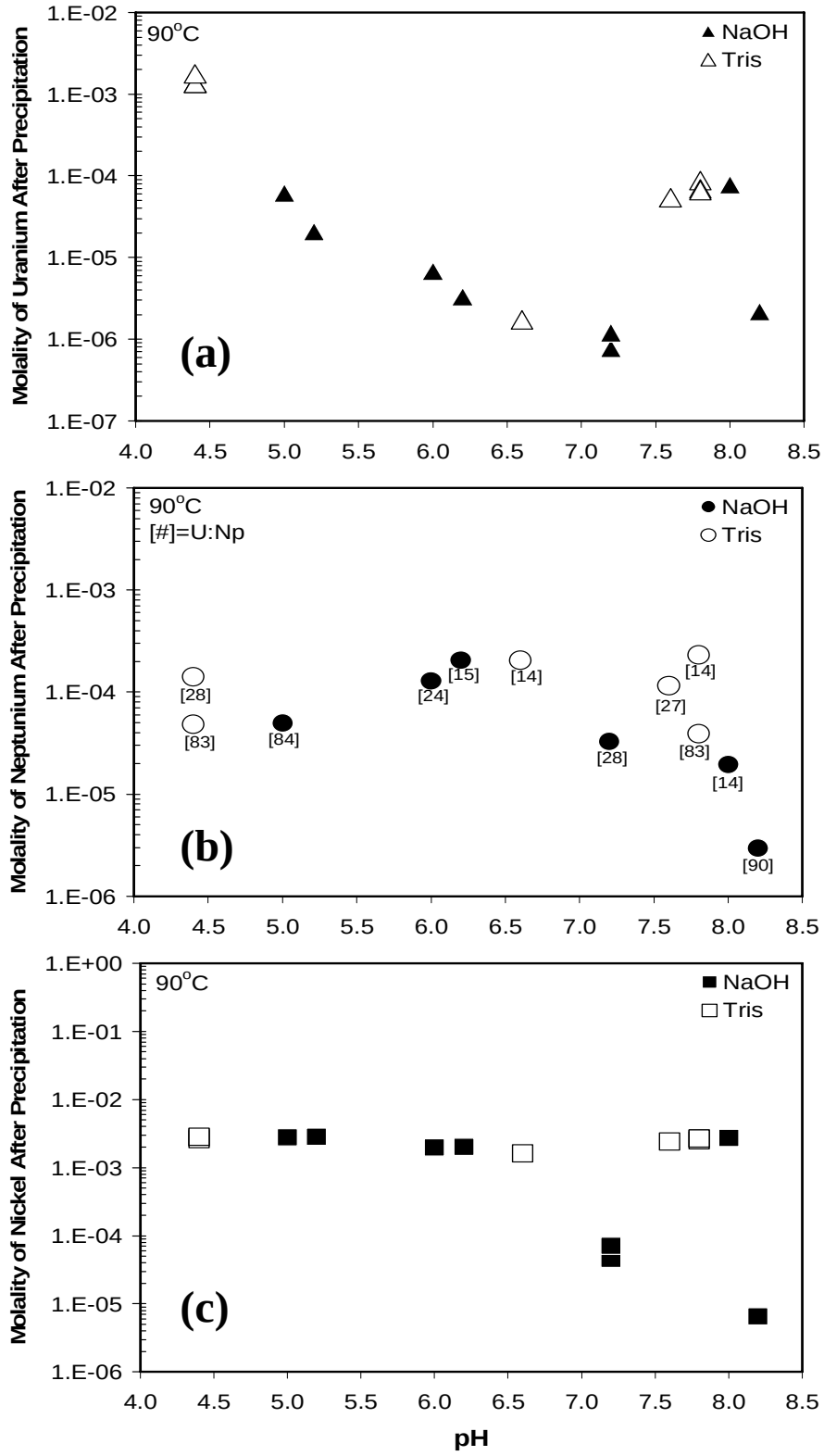

Fig. 3-1. Dissolved Concentrations after Precipitation Plotted as a Function of Measured Final pH for (a) U, (b) Np, and (c) Ni. Filled and open symbols indicate samples titrated with sodium hydroxide and tris, respectively.

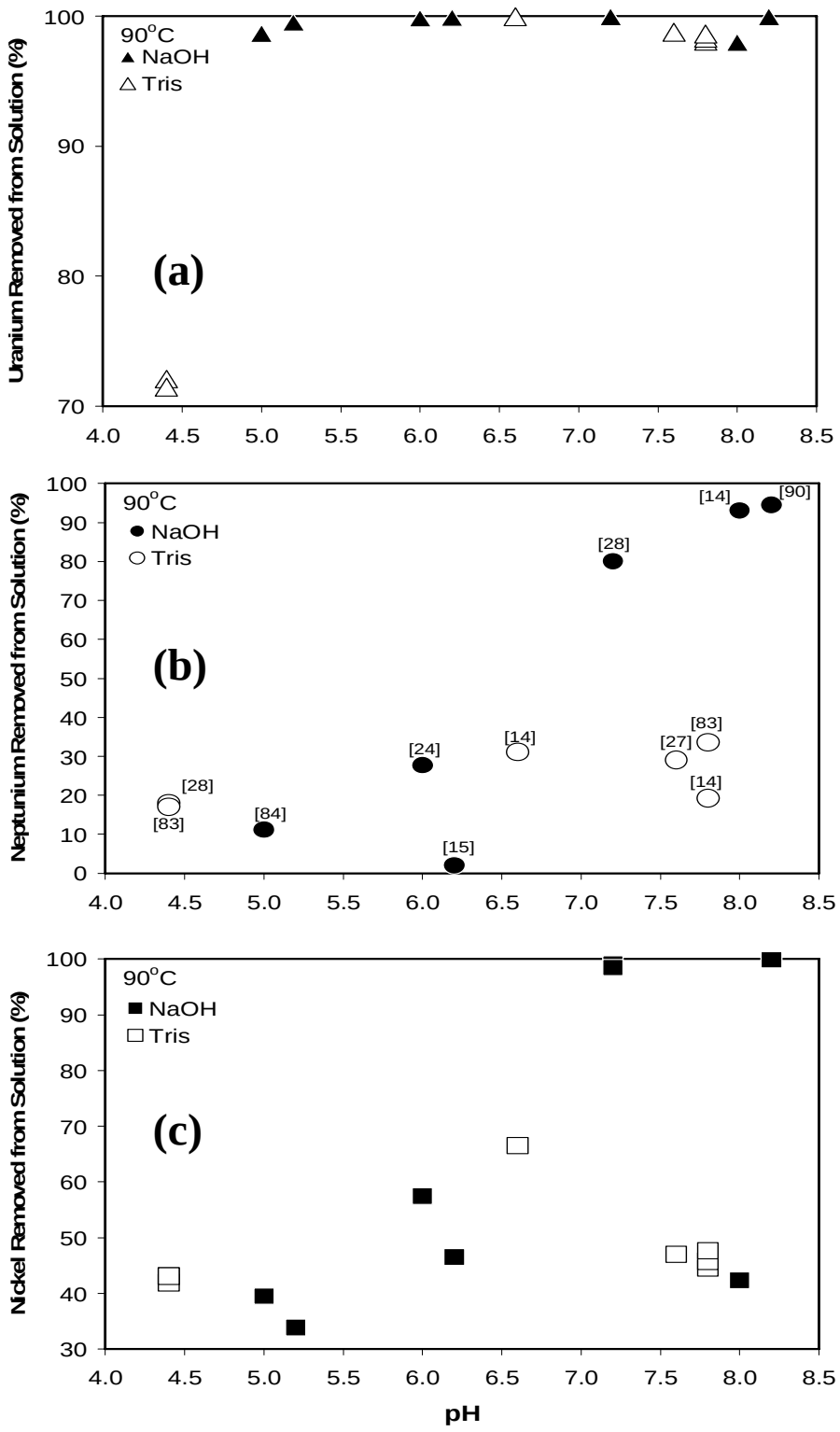

Fig. 3-4. Percent Uptake after Precipitation Plotted as a Function of the Measured Final pH for (a) U, (b) Np, and (c) Ni. Filled and open symbols indicate samples titrated with sodium hydroxide and tris, respectively.

3.4 DISCUSSION

The results from this set of coprecipitation tests are consistent with the hypothesis that neptunium may be incorporated into uranyl oxide hydrate precipitates if sodium is present to provide charge balance in the precipitating phase. The amount of neptunium removed from solution by uranyl phase precipitation was greater than 80% for samples that were adjusted to pH values greater than 7 using sodium hydroxide. Samples that were titrated to the same pH range using tris, which is a non-sodium-bearing base, showed neptunium removal from solution of less than 40%. This indicates that the process responsible for neptunium uptake is facilitated by the presence of sodium at pH values from 7 to 8.2, which is at the upper end of the pH range predicted for CSNF waste packages by the in-package chemistry model. Future work will focus on characterizing the solids produced from the coprecipitation tests and distinguishing the effects that pH and the presence of charge compensating ions have on the neptunium incorporation process. Most uranyl solids that have been found to retain Np (by whatever mechanism) are not currently included in performance assessment models. A substantial amount of data on the thermodynamic stability of those solids would be required before they could be included in a coprecipitation-based solubility-control model for calculating limits on dissolved Np concentrations for PA.

Results from the experiments conducted during FY 04 are consistent with the hypothesis that neptunium can be incorporated into uranyl oxide hydrate precipitates if sodium is present to provide charge balance in the precipitating phase (e.g., Burns et al. 1997, Burns et al. 2004). However, more work is needed to confirm that the neptunium uptake observed in these coprecipitation tests is by lattice incorporation rather than sorption. The presence of relatively high concentrations of Ni^{2+} in the starting solution appears to have little effect on neptunium uptake by the precipitating solid. The results are consistent with existing literature showing that spent fuel and UO_2 alteration products such as metaschoepite and dehydrated schoepite will probably incorporate only trace amounts of neptunium unless charge balance can be achieved (e.g., by the presence of a counter ion of suitable charge and ionic radius such as Na^+).

These and previous neptunium dissolved concentration tests (e.g., Friese et al. 2004a, Friese et al. 2004b, Burns et al. 2004) suggest that the extent of incorporation of neptunium into uranyl alteration phases is highly dependent on the system chemistry (e.g., presence/absence of ions capable of charge balancing the hypothesized $[NpO_2]^+ \leftrightarrow [UO_2]^{2+}$ substitution). Therefore, building a robust scientific basis for a coprecipitation model for neptunium will require experiments that systematically span the range of conditions predicted by the in-package chemistry model for CSNF waste packages. These experiments are underway as part of Test Plan ANL-TP-04-004. Furthermore, the alteration mineral paragenesis may play a key role in whether or not neptunium is incorporated into tertiary alteration phases (e.g., uranyl silicates). That is, if neptunium is not incorporated into the alteration phases that form first (e.g., metaschoepite) then there may not be a pathway for incorporation into alteration phases that form later (e.g., Na boltwoodite).

Based on the literature reviewed and referenced in Section 3.1, we suggest here that current Np-based dose estimates are conservative, in part due to the use in performance assessment models of a pure Np phase (Np_2O_5) that is thermodynamically unstable relative to the

less-soluble NpO_2 phase, as well as the use of questionable solubility data for Np_2O_5. Current experimental evidence, albeit limited, suggests that NpO_2 is more likely to provide an upper limit on dissolved Np concentrations. NpO_2 is not included in PA models because it has not been observed to form under the expected range of repository-relevant temperatures (20 to 100°C); however, this reflects an apparent kinetic barrier to spontaneous nucleation from a homogeneous solution. Although accurately predicting dissolved Np concentrations in waters emanating from a breached waste container would probably require detailed knowledge about Np substitution into, and sorption onto, a wide variety of internal waste package components (including spent fuel, stainless steel, and their respective alteration/corrosion products), NpO_2 should provide a realistic yet conservative upper limit on dissolved Np concentrations. Furthermore, considerable effort would be required to implement a defensible "secondary-phase" or "solid-solution" model into performance assessment calculations, especially within the time frame of successfully licensing the repository to accept waste by 2010. On the other hand, implementing a demonstrably conservative, yet realistic, single pure-phase model based on NpO_2 should be relatively straightforward. In order to do this, additional effort is required to ascertain whether NpO_2 is likely to provide a conservative upper limit on dissolved Np concentrations under repository-relevant conditions.

3.5 REFERENCES

Bethke, C.M. (1996). *Geochemical Reaction Modeling*. Oxford University Press, New York.

Bruno, J., Duro, L., de Pablo, J., Casas, I., Ayora, C., Delgado, J., Gimeno, M.J., Peña, J., Linklater, C., Pérez del Villar, L., and Gómez, P. (1999). "Estimation of the Concentrations of Trace Metals in Natural Systems. The Application of Codissolution and Coprecipitation Approaches to El Berrocal (Spain) and Poços de Caldas (Brazil)." *Chemical Geology,* **151,** 277-291. Amsterdam, The Netherlands: Elsevier Science B.V. TIC: 246492.

Buck, E.C., Finch, R.J., Finn, P.A., and Bates, J.K. (1998). "Retention of Neptunium in Uranyl Alteration Phases Formed During Spent Fuel Corrosion." *Scientific Basis for Nuclear Waste Management XXI, Symposium held September 28-October 3, 1997, Davos, Switzerland.* (edited by I.G. McKinley and C. McCombie), **506,** 87-94. Warrendale, Pennsylvania: Materials Research Society. TIC: 240702.

Buck, E.C., McNamara, B.K., Douglas, M., and Hanson, B.D. (2003). *Possible Incorporation of Neptunium in Uranyl (VI) Alteration Phases*. PNNL-14277, Pacific Northwest National Laboratory, Richland, Washington.

Buck, E.C., Finn, P.A., and Bates, J.K. (2004). "Electron Energy-Loss Spectroscopy of Anomalous Plutonium Behavior in Nuclear Waste Materials." *Micron* **35**(4), 235-243.

Burns, P.C., Ewing, R.C., and Miller, M.L. (1997). "Incorporation Mechanisms of Actinide Elements into the Structures of U(6+) Phases Formed During the Oxidation of Spent Nuclear Fuel." *Journal of Nuclear Materials,* **245**(1), 1-9. Amsterdam, The Netherlands: Elsevier Science B.V. TIC: 235501.

Burns, P.C., Deely, K.M., and Skanthakumar, S. (2004). “Neptunium Incorporation into Uranyl Compounds that Form as Alteration Products of Spent Nuclear Fuel: Implications for Geologic Repository Performance.” *Radiochimica Acta* **92**(3), 151-159.

Chen, Y. (2003). "Using Reactive Transport Modeling to Evaluate the Source Term at Yucca Mountain." *Computers & Geosciences* **29,** 285-397. New York, New York: Pergamon. TIC: 254363.

CRWMS M&O (2000a). *Secondary Uranium-Phase Paragenesis and Incorporation of Radionuclides into Secondary Phases*. ANL-EBS-MD-000019, Rev. 00. Las Vegas, Nevada: CRWMS M&O. ACC: MOL.20000414.0644.

CRWMS M&O (2000b). *Waste Form Degradation Process Model Report*. TDR-WIS-MD-000001, Rev. 00, ICN 01. Las Vegas, Nevada: CRWMS M&O. ACC: MOL.20000713.0362.

CRWMS M&O (2000c). *Pure Phase Solubility Limits-LANL*, ANL-EBS-MD-000017, Rev. 00, ICN 01.

CRWMS M&O (2000d). *FY 01 Supplemental Science and Performance Analyses Volume 1: Scientific Bases and Analyses*. TDR-MGR-MD-000007, Rev. 00. Las Vegas, Nevada: CRWMS M&O.

DOE (1998). U.S. Department of Energy, Office of Civilian Radioactive Waste Management: *Viability Assessment of a Repository at Yucca Mountain. Total System Performance Assessment. Volume 3*. DOE/RW-0508. USDOE OCRWM, Yucca Mountain Site Characterization Office, North Las Vegas, Nevada.

Douglas, M., Clark, S.B., Friese, J.I., Arey, B.W., Buck, E.C., Hanson, B D., Utsunomiya, S., and Ewing, R.C. (2004). “Neptunium Association with Uranium(VI) Silicate Solid Phases.” *Radiochimica Acta* (in press).

Efurd, D.W., Runde, W., Banar, J.C., Janecky, D.R., Kaszuba, J.P., Palmer, P.D., Roensch, F.R., and Tait, D. (1998). "Neptunium and Plutonium Solubilities in a Yucca Mountain Groundwater." *Environmental Science & Technology*, **32**(24), 3893-3900. Easton, Pennsylvania: Environmental Science & Technology. TIC: 243857.

Finch, R.J., Suksi, J., Rasilainen, K., and Ewing, R.C. (1996). "Uranium Series Ages of Secondary Uranium Minerals, with Applications to the Long-Term Storage of Spent Nuclear Fuel." *Scientific Basis for Nuclear Waste Management XIX, Symposium held November 27-December 1, 1995, Boston, Massachusetts* (edited by W.M. Murphy and D.A. Knecht), **412**, 823-830. Pittsburgh, Pennsylvania: Materials Research Society. TIC: 233877.

Finch, R.J., Buck, E.C., Finn, P.A., and Bates, J.K. (1999). "Oxidative Corrosion of Spent UO_2 Fuel in Vapor and Dripping Groundwater at 90°C." *Scientific Basis for Nuclear Waste Management XXII, Materials Research Society Symposium held November 30-December 4,*

1998, Boston, Massachusetts, USA (edited by D.J. Wronkiewicz and J.H. Lee.), **556**, 431-438. Warrendale, Pennsylvania: Materials Research Society. TIC: 246426.

Finch, R.J., and Murakami, T. (1999). "Systematics and Paragenesis of Uranium Minerals." Chapter 3 of *Uranium: Mineralogy, Geochemistry and the Environment* (edited by P.C. Burns and R.J. Finch) Reviews in Mineralogy, **38**. Washington, D.C. Mineralogical Society of America. TIC: 247121.

Finch, R.J., and Cunnane, J.C. (2001). "Modeling Neptunium Concentrations in a Breached Waste Package with Commercial Spent Fuel." In *Proceedings of the Ninth International Conference on High-Level Radioactive Waste Management*, Las Vegas, Nevada, (American Nuclear Society, LaGrange Park, Illinois).

Finch, R.J. (2002). "Precipitation of Crystalline NpO_2 during Oxidative Corrosion of Neptunium-Bearing Uranium Oxides." In *Scientific Basis for Nuclear Waste Management XXV*, B.P. (edited by B.P. McGrail and G.A. Cragnolino) Materials Research Society Symposium Proceedings, **713**, 639-646.

Finn, P.A., Wronkiewicz, D.J., Finch, R.J., Hoh, J.C., Mertz, C.J., Emery, J.W., Buck, E.C., Fortner, J.A., Wolf, S.F., Neimark, L.A., and Bates, J.K. (1998). *Yucca Mountain Project – Argonne National Laboratory, Annual Progress Report, FY 1997 for Activity WP 1221*. Argonne Technical Report ANL-98/12 (June).

Fortner, J.A., Finch, R.J., Kropf, A.J., and Cunnane, J.C. (2004). "Re-Evaluating Neptunium in Uranyl Phases Derived from Corroded Spent Fuel," *Nuclear Technology* **148**(2), 174-180.

Friese, J.I., Buck, E.C., McNamara, B.K., Hanson, B.D., and Marschman, S.C. (2003). "Existing Evidence for the Fate of Neptunium in the Yucca Mountain Repository." PNNL-14307, Pacific Northwest National Laboratory, Richland, Washington.

Friese, J.I., Douglas, M., McNamara, B.K., Clark, S.B., Hanson, B.D. (2004a). *Np Behavior in Synthesized Uranyl Phases: Results of Initial Tests*, PNNL-14856. Pacific Northwest National Laboratory, Richland, Washington.

Friese, J.I., Douglas, M., Clark, S.B., Buck, E.C., and Hanson, B.D. (2004b). *Neptunium Incorporation/Sorption with Uranium Alteration Products*, Materials Research Society, 2004 Spring Meeting.

Kaszuba, J.P., and Runde, W.H. (1999). "The Aqueous Geochemistry of Neptunium: Dynamic Control of Soluble Concentrations with Applications to Nuclear Waste Disposal." *Environmental Science & Technology*, **33**(24), 4427-4433. American Chemical Society, Washington, D.C. TIC: 246667.

Kropf, A.J., Fortner, J.A., Finch, R.J., Cunnane, J.C., Karanfil, C. "A Bent Silicon Crystal in the Laue Geometry to Resolve Actinide X-Ray Fluorescence for X-Ray Absorption Spectroscopy." *Physica Scripta* (in press).

McNamara, B.K., Buck, E.C., Hanson, B.D. (2003) “Observation of Studtite and Metastudtite on Spent Fuel.” *Scientific Basis for Nuclear Waste Management XXVI* (edited by R.J. Finch and D.B. Bullen) Materials Research Society Symposium Proceedings ,**757**, 401-409.

NEA OECD 2001. *Chemical Thermodynamics of Neptunium and Plutonium*. (NEA, Vienna).

Quinones, J., Serrano, J., Diaz Arocas, P., (2001). “The Effect of Coprecipitation in Some Key Spent Fuel Elements.” *Journal of Nuclear Materials*, **298**, pp. 63-68.

Roberts, K.E., Wolery, T.J., Palmer, C.E.A., Prussin, T.G., Allen, P.G., Bucher, J.J., Shuh, D.K., Finch, R.J., Prussin, S.G. (2003). “Precipitation of Crystalline Neptunium Dioxide from Near-Neutral Aqueous Solution.” *Radiochimica Acta*, **91**, 87-103.

Sassani, D., and Siegmann, E. (1999). CRWMS M&O Report B00000000-01717-2200-00191. Las Vegas, Nevada.

Viswanathan, H., Robinson, B.A., Valocchi, A.J., and Triay, I.R. (1998). “A Reactive Transport Model of Neptunium Migration from the Potential Repository at Yucca Mountain.” *Journal of Hydrology,* **209**, 251-280.

Wronkiewicz, D.J., Bates, J.K., Gerding, T.J., Veleckis, E., and Tani, B.S. (1992). "Uranium Release and Secondary Phase Formation during Unsaturated Testing of UO2 at 90°C." *Journal of Nuclear Materials,* **190**, 107-127. Amsterdam, The Netherlands: North-Holland Publishing Company. TIC: 236558.

Wronkiewicz, D.J., Bates, J.K., Wolf, S.F., and Buck, E.C. (1996). "Ten-Year Results from Unsaturated Drip Tests with UO2 at 90°C: Implications for the Corrosion of Spent Nuclear Fuel." *Journal of Nuclear Materials,* **238**(1), 78-95. Amsterdam, The Netherlands: North-Holland Publishing Company. TIC: 243361.

4.0 HLW GLASS TESTING
(W. Ebert)

Glass testing was performed in Fiscal Year 2004 (FY 04) to address two issues regarding coefficient values used in the Defense HLW glass degradation model. The first issue is that the coefficients used for the temperature dependencies in acidic and alkaline solutions were determined from tests conducted at 70 and 90ºC, which is a narrow temperature range. The second issue is that tests were conducted with a glass representing the HLW glass anticipated from the Defense Waste Processing Facility (DWPF), while about 60% of the HLW glass to be disposed will be from Hanford. The rates calculated with the model must be representative of Hanford glasses. Therefore, several tests were conducted to evaluate the adequacy of the current model for modeling glass dissolution at low temperatures and dissolution of a glass with a composition relevant to Hanford HLW glass. To extend the temperature range of the available data, we conducted tests at 40ºC with the same glass (SRL 202G) and same test method used to determine the current model coefficients. These results can be used to provide confidence that the temperature dependence coefficients (activation energies) in the current model adequately represent dissolution at low temperatures, or to revise the activation energies in the future. Tests were also conducted to measure the degradation rates of a glass formulated to represent HLW glass from Hanford (namely, Hanford-H glass) for comparison with the model and with tests used to develop the model. The results can be used to provide confidence that the model adequately represents Hanford HLW glasses.

The tests with SRL 202G and Hanford-H glasses were conducted following the scientific investigation test plan (SITP) "Long-Term Studies of the Degradation and Radionuclide Release from Defense High-Level Waste (DHLW) Glass," (SITP-02-WF-002, Rev. 00) under the *Technical Work Plan for Waste Form Degradation Testing* (TWP-WIS-MD-000008, Rev. 02 ICN 04 and TWP-WIS-MD-000008, Rev. 03). The tests were conducted under the *ANL Quality Assurance Plan for Technical Activities in Support of the Yucca Mountain Project* (YMP/G-3A-001, Rev. 05). One exception is that solutions for tests conducted with Hanford-H glass in leachants spiked with salt had to be analyzed using an analytical method that did not comply with QA requirements. Those data are included for corroborative purposes only and are identified in this report as "non-Q data."

Data were compiled and analyzed using the Microsoft Office version XP of Microsoft EXCEL. Simple statistical computations (e.g., the calculation of mean values and standard deviations) were performed using the routines provided with EXCEL. Data plots were generated using KaleidaGraph software (Version 3.6, Abelbeck Software) and linear regression routines provided within that commercial software application. The transcriptions, calculations, plots, and regressions were checked by an independent technical reviewer.

4.1 BACKGROUND

The release of radionuclides from high-level radioactive waste (HLW) glasses is quantified in TSPA calculations using the Defense HLW glass degradation model (BSC 2004). The release of radionuclides is modeled to occur at the same rate (on a fractional basis) that the glass degrades, which was determined from the release rate of boron under various laboratory

test conditions representing possible repository environments. The model accounts specifically for the effects of solution pH and temperature on the dissolution rate, and uses a range of rate coefficient values to account for the effects of the glass composition, solution composition, and water contact conditions (i.e., humid air, dripping water, or immersion). The specific glass dissolution rate is calculated in the model by using Equation 4-1,

$$rate_G = k_E \bullet 10^{\eta \bullet pH} \bullet \exp\left(\frac{-E_a}{RT}\right), \tag{4-1}$$

where $rate_G$ is the dissolution rate in units of mass glass per unit area per unit time, k_E is the rate coefficient, η is the pH coefficient, E_a is the temperature coefficient, T is the absolute temperature, and R is the ideal gas constant. The dissolution rates of borosilicate waste glasses have a "V-shaped" pH dependence in which the rates are lowest at near-neutral pH values and increase as the pH increases or decreases from near-neutral pH values. The two parts of "V" are referred to as the acidic and alkaline legs, and the rate expression given in Equation 4-1 is used to model each leg with separate parameter values. Single values for η and E_a and maximum and minimum values for k_E were determined for the acidic and alkaline legs from rates measured in various laboratory tests in which glass samples were immersed in acidic or alkaline solutions, exposed to humid air, or contacted by dripping water. In implementing the model in TSPA, values of k_E can be selected from ranges specified for the acidic and alkaline legs. The sum of the rates calculated with the equations for the acidic and alkaline legs will give the glass degradation rate, which can be used as the fractional release rate of all radionuclides in TSPA calculations. The rates calculated with the model using the maximum and minimum values of k_E are given by Equations 4-2a and 4-2b, respectively, where the rate has units of g/(m^{2}d) and T is the temperature in Kelvin:

$rate_{maximum}$

$$= 1.15\times10^{7} \bullet 10^{-0.49 \bullet pH} \bullet \exp\left(\frac{-31}{0.008314\times T}\right) + 3.47\times10^{4} \bullet 10^{0.49 \bullet pH} \bullet \exp\left(\frac{-69}{0.008314\times T}\right) \tag{4-2a}$$

$rate_{minimum}$

$$= 8.41\times10^{3} \bullet 10^{-0.49 \bullet pH} \bullet \exp\left(\frac{-31}{0.008314\times T}\right) + 28.2 \bullet 10^{0.49 \bullet pH} \bullet \exp\left(\frac{-69}{0.008314\times T}\right) \tag{4-2b}$$

In the model, the ranges of k_E have triangular distributions, with the most probable values (the modes) being the minimum values. The mean values of k_E are given by the averages of the minimum, mode, and maximum values of the distributions for each leg. The mean values are $k_{E\ mean\ acidic}$ = 3.84 x 10^6 g/(m^{2}d) and $k_{E\ mean\ alkaline}$ = 1.16 x 10^4 g/(m^{2}d), and the equation for the mean rate is given by Equation 4-2c:

$rate_{mean}$

$$= 3.84\times10^{6} \bullet 10^{-0.49\bullet pH} \bullet \exp\left(\frac{-31}{0.008314\times T}\right) + 1.16\times10^{4} \bullet 10^{0.49\bullet pH} \bullet \exp\left(\frac{-69}{0.008314\times T}\right) \quad \text{(4-2c)}$$

The in-package chemistry model uses the most expected (minimum) rate in Equation 4-2b.

4.1.1 Tests with SRL 202U Glass at 40ºC

In the Defense HLW glass degradation model, the same pH dependence is used at all temperatures and the same temperature dependence is used at all pH values. The coefficient values for the pH and temperature dependence terms in the current model (i.e., Equations 4-2a, 4-2b, and 4-2c) were determined from the results of tests with a glass referred to as SRL 202G glass, which has a composition representative of HLW glasses being made at the Defense Waste Processing Facility (DWPF) at the DOE Savannah River Site. (Note that SRL 202G glass was formulated and made for use in tests specified for SRL 165 glass in the SITP. The different name was adopted during glass preparation.) Tests were conducted previously with SRL 202G glass at 70 and 90ºC in simple 2-component pH buffer solutions at nominal pH values of 1.3, 3.7, 4.9, 8.5, 9.3, 9.8, and 12 (Ebert 2003). Although these tests spanned a wide pH range, the temperature range was narrow. Tests at 40ºC were planned, but they were delayed, and data were not available during development of the model. Those tests were completed in FY 04, and the results can be compared with the pH and temperature dependencies used in the current model to evaluate the accuracy of the model at low temperatures. The results of tests at 40ºC can be used to refine the coefficients for future revisions to the model. The methodology used to determine the temperature dependence of the model is summarized below.

The pH dependence was determined first by separate regression of the dissolution rates measured in the acidic or alkaline solutions at each temperature. The average of the pH dependencies determined from tests at 70 and 90ºC was used for the model; those values are -0.49 and 0.49 for acidic and alkaline legs, respectively. The temperature dependence was then determined by fitting the data for tests at each temperature with lines having the average pH dependence (this was done separately for tests in acidic and alkaline solutions). The fitted lines were used to determine the dissolution rates at pH 0 and pH 14. The differences in the rates at pH 0 and pH 14 at 70 and 90ºC were used to determine the temperature dependence for the rate equations in acidic and alkaline solutions with the Arrhenius equation by using Equation 4-3:

$$E_a = \frac{\ln\left(\frac{rate_2}{rate_1}\right) \bullet R}{\frac{1}{T_1} - \frac{1}{T_2}} \quad \text{(4-3)}$$

where E_a is the activation energy, $rate_1$ is the dissolution rate at temperature T_1 (K), $rate_2$ is the dissolution rate at temperature T_2 (K), and R is the ideal gas constant, 0.008314 kJ/(mol•K). The resulting activation energies used in the model are 31 and 69 kJ/mol for the acidic and alkaline legs, respectively.

4.1.2 Tests with Hanford-H Glass

Glasses made with Hanford tank wastes at the Waste Treatment and Immobilization Plant will account for about 60% of the HLW glass to be disposed in the Yucca Mountain repository. However, because the range of compositions for Hanford HLW glasses had not been identified at the time testing was started, most laboratory tests supporting TSPA model development were conducted with glasses representing HLW glasses from the DWPF, in particular, SRL 202G glass. A glass referred to as "Hanford-H" glass was formulated based on glass compositions recently developed for Hanford HLW. The objective of the tests with Hanford-H glass was to provide data that can be used to evaluate how well the model parameter values developed in the Defense HLW glass degradation model are likely to represent Hanford HLW glasses. Tests were conducted to compare degradation rates measured at different temperatures with each other and with the rates calculated using the model. Additional tests were conducted with Hanford-H glass in brine solutions made to simulate evaporated tuff groundwater seepage in a breached waste package. The Defense HLW glass degradation model does not directly account for separate effects of brine solutions, and tests in brines were not used in the development of the model. This was because previous tests have shown no deleterious effects of brines on glass dissolution relative to demineralized water (e.g., Marples et al. 1990). The dissolution rates of Hanford-H glass at 90ºC in pH 3.7 and pH 9.7 leachant solutions without and with added NaCl and KCl are compared. The analytical method that was required to analyze the brine test solutions is not currently compliant with QA requirements, and those results cannot be used to develop the model. Nevertheless, they provide corroborative data that validate the omission of an additional term for the effect of brines in the glass model.

4.2 PROCEDURES

Tests were conducted to allow direct comparison with the results of tests used to develop the model parameter values and with the degradation rates calculated with the model under the test conditions. Three test methods were used to measure the glass dissolution rate under a wide range of conditions: the Materials Characterization Center Test No. 1 static leach tests (MCC-1 tests), the product consistency test (PCT), and the vapor hydration test (VHT). The MCC-1 and PCT methods have been standardized by the American Society for Testing and Materials (ASTM) International, and an ASTM standard method is being developed for the VHT. These methods are represented by ANL procedures that identify quality assurance and records requirements for the test methods. The glass degradation rates measured under these test conditions can be compared with the rates calculated by the Defense HLW glass degradation model at equivalent temperatures and pH values. The MCC-1, PCT, and VHT methods are described in detail below.

4.2.1 MCC-1 Static Leach Test Method

Tests were conducted using an ANL procedure that is a slight modification of the Materials Characterization Center static leach test method 1 (MCC-1). [The MCC-1 method has been standardized by the ASTM as standard test method C 1220 (ASTM-C1220) (ASTM

2002a). Monolithic samples of SRL 202G glass were prepared as disks with the faces ground to a final surface finish using 600-grit SiC paper with water lubrication.

The pH values of the stock buffer solutions themselves and of solutions recovered from blank tests conducted without glass were measured for comparison with solutions from tests with glass to determine if glass dissolution affected the pH significantly. The concentrations of key glass components present in the leachant solutions were determined by analysis of both the leachant and the blank tests solutions. These were used as background concentrations for tests with glass.

All MCC-1 tests were conducted in 23-mL Teflon vessels with Teflon mesh sample support stands. The vessels and support stands were cleaned by filling with a dilute nitric acid solution and heating at 70ºC overnight. This was followed by three or more full-volume rinses of demineralized water. Tests at 40 ºC were conducted by placing the sample in the vessel and then adding enough buffer solution to attain a glass surface area-to-solution volume (S/V) ratio of about 10 m^{-1}. Adding a mass of solution, in grams, equal to ten times the surface area of the sample, in cm^3, results in an S/V ratio of about 10 m^{-1}. Tests at 90 ºC were conducted with an amount of solution 17 times the surface area of the sample to generate an S/V ratio of about 7 m^{-1}. This provides sufficient solution to dilute the silica released from the glass to concentrations low enough that solution feedback effects remain negligible in tests run over several days. The results of tests conducted for different durations are expected to indicate when solution feedback has become significant. The tests conducted for short durations are expected to show a linear increase in the concentrations of soluble components, whereas concentrations in tests of longer durations will deviate negatively due to the slowing effect of dissolved silica. Blank tests were conducted by placing an amount of buffer solution similar to the amount used in tests with glass in a Teflon test vessel. Blank tests were conducted for 10 days and used as background concentrations for all test durations.

Vessels were sealed, weighed, and placed in an oven that had been previously set at the desired temperature. The oven temperature was verified using a NIST-traceable thermometer prior to starting the tests. The oven temperature was continuously monitored with a thermocouple and logged by a recorder twice a day. At the end of the scheduled test duration, the vessels were removed from the oven, weighed, and opened. The change in weight of the sealed vessel was used to determine if any leakage occurred during the test. A small aliquot of the solution (about 0.5 mL) was taken for pH analysis. The pH was measured at room temperature with a combination electrode that had been calibrated with NIST-traceable buffer solutions immediately before measurement of test solutions. The pH values of the test solutions were measured within two hours after opening the vessels. The remaining test solutions were stabilized with a few drops of concentrated nitric acid and submitted for composition analysis with inductively coupled plasma-mass spectrometry (ICP-MS). The glass samples were placed in labeled containers and archived.

The B concentrations measured in the test solutions were used to calculate the amounts of glass that dissolved in tests in each pH buffer. Boron is commonly used as an indicator of glass dissolution and was used for this purpose in previous tests with SRL 202G glass. The Si concentration was also measured to track its effect on the reaction affinity. The Na concentration

was measured to compare the rate of dealkalization with the rate of glass dissolution. The normalized mass losses based on B, Na, and Si were calculated by dividing the measured concentration (less the background concentrations in the leachant solutions as measured in the blank tests) by the S/V ratio of the test and by the mass fraction of B, Na, or Si in the glass. The normalized mass loss gives the mass of glass dissolved per unit surface area. The glass dissolution rate is then determined from a plot of the normalized mass loss (NL) against the test duration. The values of NL(B), NL(Na), and NL(Si) are all expected to increase linearly in short-term tests and then deviate negatively at longer test durations as the concentration of dissolved silica increases. Only the results prior to the rollover are used to determine the rates used to evaluate the pH and temperature dependencies.

The same scheme that was used for identifying tests conducted at 70 and 90ºC was used to identify tests conducted at 40ºC. The test number was used to indicate the glass composition, nominal buffer pH value, test temperature, and test duration. In the generic test number "GBx-y-z," G indicates a test with SRL 202G glass and H indicates a test with Hanford-H glass, Bx gives the buffer index number, y gives the temperature, and z is a suffix used to identify the test duration. Blank tests were conducted for 10 days with each buffer and are indicated by the suffix "B1" in the test number. The concentrations measured in the blank tests are used as background concentrations in tests with glass. Four tests with SRL 202G were added to the matrix after the initial series of tests was completed. These were conducted to provide longer test durations (16 and 23 days) for tests series in which the dissolution rate was not well defined by the shorter-term tests. The solutions from these tests were analyzed only for B, Na, and Si. The matrices of MCC-1 tests with SRL 202G and Hanford-H glass are included in Table 4-1.

4.2.2 Product Consistency Test (PCT) Method

The PCT is conducted by immersing a known mass of crushed and sized glass in a known volume of demineralized water and measuring the amounts of soluble glass components released into the solution after various test durations (ASTM-C1285) (ASTM 2002b). Triplicate 7-day PCTs were conducted with Hanford-H glass for comparison with PCTs that were conducted with other reference glasses as part of TSPA glass degradation model development. Specifically, the average rates of several reference waste glasses over the 7-day test period, which were calculated as NL(B)/7, were used to determine the value of the rate coefficient (k_E) that is used to calculate the maximum rate in alkaline solutions. The PCT with Hanford-H glass can also be used to show that the glass meets chemical durability requirements in the Waste Acceptance System Requirements Document, which is evaluated using a 7-day PCT. Triplicate PCTs were conducted in parallel with duplicate blank tests. Tests were conducted in demineralized water using 23-mL Type 304L stainless steel vessels with Teflon gaskets. Vessels were placed in an oven maintained at 90±2ºC. The oven temperature was confirmed to be at 90±2ºC using a NIST-traceable thermometer prior to starting the tests. The oven temperature was continuously monitored with a thermocouple and logged by a recorder twice a day. The vessels were removed from the oven after 7 days (±2 hours) and allowed to cool briefly. Aliquots of the test solution were then taken for pH and ICP-MS analysis. The pH was measured with a combination electrode that was calibrated with NIST-traceable standards before use. The solutions for ICP-MS analysis were diluted with demineralized water and acidified with a few drops of concentrated nitric acid. The reacted glass was removed from the vessels and archived. The

PCTs are referred to as PHanH-1, PHanH-2, and PHanH-3, with the prefix "P" indicating the test is a PCT, and "HanH" indicating the test was run with Hanford-H glass. The two PCT blanks are designated PHanH-B1 and PHanH-B2. The test matrix is included in Table 4-1.

4.2.3 Vapor Hydration Test Method

The VHT is conducted by suspending two monolithic samples in a test vessel containing a small amount of water. The samples are prepared the same as for MCC-1 tests and with a 600-grit finish. Water vapor formed at the test temperature condenses on the glass due to glass deliquescence, and the glass reacts with the condensed water. At the end of the desired test duration, the samples are removed and the corroded surfaces examined. A series of VHTs was conducted with Hanford-H glass using different amounts of added water. Some tests were conducted with only enough water to saturate the air in the vessel and form a thin static film of water on the samples at the test temperature. These are referred to as "standard VHTs." Other tests were conducted with enough water that a reflux cycle occurred during the test, wherein water vapor condensed on the glass, then dripped off. Under these conditions, the glass is continuously rinsed by freshly condensed water. These are referred to as "excess-water VHTs." The amount of water in the VHT vessel affects the reaction progress. In standard VHTs, only enough water to form a static thin film of condensed water on the test samples is available in the test vessel, and components released as the glass degrades are confined to the static film.

In excess-water VHTs, enough water is available within the test vessel to be absorbed into the surface film and cause solution to drip off during the test. Solution dripping from the sample carries dissolved glass components with it to the reservoir of water in the vessel bottom. Water from that reservoir will evaporate and condense into the film of water on the sample as long as the vapor pressure of the solution in the reservoir exceeds that of the solution on the sample. If enough water is present in the vessel, a reflux cycle can be established wherein fresh vapor continuously condenses in the solution on the glass and dilutes it, while solution periodically drips off the sample back into the reservoir. The accumulation of soluble glass components in the reservoir as a function of time provides a measure of the extent of glass dissolution rate. Because the solution contacting the glass in excess-water VHTs is continuously refreshed, it is not expected to become as alkaline as it does in standard (static) VHTs. Excess-water VHTs represent conditions in which the humid air contacting the glass is refreshed and water vapor can continuously condense on the sample, for example, due to the deliquescence of glass corrosion products. Tests with excess water provide insight into the role of deliquescence as a process for accumulating water in a breached codisposal package.

The VHTs were conducted by suspending two glass monoliths with a small amount of demineralized water in a Type 304L stainless steel vessel. Standard VHTs were conducted with 0.15 g of water added for tests at 150ºC and 0.25 g of water added for tests at 200ºC. This provided enough water to saturate the air space at the test temperature plus condense about 0.05 mL of water on each sample. The excess-water VHTs at all temperatures were conducted with 3 g of demineralized water added to the vessel. It was expected that this would provide an adequate source of water to maintain a reflux cycle and saturated vapor at all test temperatures. The samples used in the VHTs were prepared in the same way as those used in MCC-1 tests. The dimensions of the samples used in the excess-water VHTs were measured and the surface

area calculated; the surface areas were needed to calculate the dissolution rates from the measured solution concentrations. The dimensions of samples used in standard VHTs were not measured because the surface area was not used to determine the extent of reaction in those tests. Instead, the thickness of an alteration layer formed at the sample surface was used to determine the extent of reaction in standard VHTs. Small notches were cut on diametrically opposite sides of each sample for tying the sample with Teflon thread. Two samples were suspended in each test vessel from an inverted U-shaped Type 304L stainless steel rod using Teflon thread. The amount of demineralized water added to the vessel was determined by mass. The vessel was sealed using a Teflon gasket and a compression fitting torqued to about 120 ft-lb. The mass of the assembled vessel was measured immediately before the vessel was placed in the oven.

The oven temperatures were confirmed to be within 2ºC of the targeted temperature using a NIST-traceable thermometer prior to starting the tests. The oven temperatures were continuously monitored with thermocouples and logged by a recorder twice a day. At the end of the desired test duration, each vessel was removed from the oven and set in a shallow container of water to cool the bottom of the vessel (approximately the bottom 1 cm) and condense the water vapor. This was done to transport most of the water from the samples to the vessel bottom and condense the water vapor. The vessel was dried and weighed before being opened. For standard VHTs, the pH of water condensed in the bottom of the vessel was measured with pH paper. The pH is measured to determine if water dripped from the sample during the test or termination procedure, which would result in an alkaline pH. The samples were allowed to air dry and then removed by cutting the Teflon threads and stored for later analysis. For excess-water VHTs, an aliquot of the solution was taken to measure the pH with a combination pH electrode and the remaining solution was transferred to a tared bottle and weighed. Enough demineralized water was added to provide about 10 mL of solution for analysis and then the solutions were acidified with a few drops of ultrapure concentrated nitric acid. The solution bottles were reweighed and submitted for ICP-MS analysis. The measured concentrations were adjusted to account for the dilution by water and nitric acid based on mass.

The tests resumed after each sampling using the following procedure. After the test solution was removed from the test vessel, about 5 mL of demineralized water was added to the vessel using a pipette, being careful not to wet the samples. This was done to dilute any remaining leachate solution from the vessel. The water was then removed from the vessel using a pipette and the vessel (with the glass samples still suspended in the vessel) was placed in a 70ºC oven to dry for about 1 hour. This was done to evaporate any remaining leachate solution from the vessel and minimize carryover to the next test interval. The glass samples were not rinsed, so any residual solution that remained on the samples was carried over into the next test interval. This approach was taken so that the release rate measured was a combination of the reflux and glass dissolution rates, and material was not considered to be released until it dripped off the sample. Heating at 70ºC is expected to evaporate solution condensed on the sample, but not remove water fixed in alteration phases such as clays. The deliquescent salts left on the sample become rehydrated when the test is resumed and may drip from the sample during the next interval. The vessels were removed from the oven after drying and allowed to air-cool for about 15 minutes before restarting the tests. The Teflon gaskets in the vessel lids were replaced before restarting the tests. Approximately 3 mL of demineralized water was added to the vessel; then the vessel was sealed, weighed, and placed back into the test oven to continue the test.

Tests were typically interrupted for about 4 hours to sample and replace the water. This time was not subtracted from the total test duration.

Test numbers were assigned to identify the test as a VHT with particular glass, the test temperature, and a numerical indicator. For example, test VHan(150)-1 is a VHT (V) with Hanford-H glass (Han) conducted at 150ºC (150), and is test number 1. An additional digit was used to designate the solutions collected during excess-water VHTs, so that VHan(150)-1-1 was the first solution collected from test VHan(150)-1. Other glasses subjected to VHTs to generate samples for isopiestic tests and their identifiers are SRL 202U (202U) and SRL 131U (131U).

Four of the standard VHTs with Hanford-H glass were restarted when visual inspection showed very little alteration of the glass. This was done by following the same procedure used to restart the excess-water VHTs (as described above), except solution was not collected and the vessel was not rinsed. The Teflon gaskets were replaced and 0.15 or 0.25 g of demineralized water was added, depending on the test temperature. The vessel was then sealed, weighed, and placed back into the oven to continue the test. To distinguish the two exposure times of interrupted standard VHTs, an "a" was appended to the test number for the initial interval and a "b" was appended to the test number for the second interval. The matrix of VHTs is included in Table 4-1.

4.2.4 SRL 202G and Hanford-H Glasses

Samples of SRL 202G glass that had been prepared previously were used in the MCC-1 tests. The glass was formulated to represent the target composition of DWPF glasses, and the compositions are given in Table 4-2.

The Hanford-H glass was formulated by simplifying the composition of one of two glasses being considered for immobilizing the Hanford HLW stream by excluding minor components, components that are controlled under the Resource Conservation and Recovery Act (RCRA), and uranium to facilitate material handling and disposal. This is not expected to significantly affect the glass corrosion behavior. Enough reagent-grade chemicals to make about 300 g of glass were mechanically mixed, then placed in a platinum/gold crucible and melted at about 1200ºC in a laboratory furnace (in air) for about 2 hours. The molten glass was poured into a stainless steel beaker filled with water to quench the glass. The glass was recovered from the beaker and dried. It was then mechanically crushed until it passed through a 40 mesh size screen (approximately 0.4 mm). The crushed glass was placed into a platinum/gold crucible and remelted at about 1200ºC for about 2 hours. The molten glass was poured into 3 platinum/gold pans (approximately 1.5 in. x 2 in.) and 2 small platinum crucibles (approximately 5 mL), all of which had been preheated to about 1200ºC. The pans and crucibles were immediately placed into a 520ºC oven to anneal, and left at that temperature for about 2 hours. The oven was then turned off and allowed to slowly cool with the glass still inside.

The glass was removed from the pans and approximately 1-cm diameter cores were cut normal to the cast surface using a low-speed core drill. Disks approximately 1.5 mm thick were then cut from the cores using a wafering saw with a diamond blade. The faces of the disks were successively ground with 240-grit, 320-grit, 400-grit, and 600-grit silicon carbide paper. The

coring, cutting, and grinding steps were all performed with water lubrication. The resulting samples had mirror-like surfaces with only a few visible scratches. The surface finish was similar to that obtained for other glasses used in testing. A small piece of the glass was fixed in epoxy resin and a polished cross section prepared for examination with SEM to search for inclusion phases, undissolved chemicals, etc. None were found. The compositions of several areas of the glass were measured with EDS during SEM examination on an approximately 1 mm^2 scale. The compositions measured in various areas indicated that the glass was compositionally homogeneous on this scale. The EDS results are consistent with the chemical analyses discussed below.

Some of the glass remaining after the cores were taken was mechanically crushed and sieved to isolate the -100 +200 mesh size fraction for use in the PCTs. The sized glass was repeatedly rinsed with demineralized water to remove fines. A sample of the prepared glass was viewed with an SEM to confirm that the fines had been removed and that the glass was properly sized. A small amount of the sized glass was used to measure the glass composition. Two aliquots of glass were dissolved in separate mixtures of 2 mL HCl + 1 mL HNO_3 + 0.5 mL HF + 4 mL H_2O. These solutions were then diluted to 50.0 mL: Sample 1 contained 50.11 mg glass to give 1.0022 mg/L and Sample 2 contained 50.14 mg glass to give 1.0028 mg/L. The two solutions were each analyzed twice with ICP-MS. The averages of the two analyses were used to calculate the mass fractions for each sample, which were averaged to obtain the glass composition. The average mass fractions in Hanford-H glass are summarized in Table 4-2. The density of the Hanford-H glass was measured to be 2.73 g/cm^3.

The diameter and thickness of monolithic samples of SRL 202G and Hanford-H glasses prepared for use in MCC-1 tests were measured with a digital caliper. The diameter was measured at one location and the thickness was measured at two diametrically opposite locations. This was done because the sample faces were flat, but not perfectly parallel. The average thickness of diametrically opposite edges will be the same regardless of where they are measured. The diameter (d) and average thickness (h) were used to calculate the surface area (S) using the formula given in Equation 4-4:

$$S = \frac{\pi d^2}{2} + \pi d h \tag{4-4}$$

4.2.5 Leachant Solutions

Leachant solutions were made following the recipes summarized in Table 4-3. Most of these solutions are not truly pH buffers; rather, they impose pH values that do not change significantly during the test as glass dissolves. They are referred to as buffer solutions for convenience. Leachant solutions were made with reagent-grade chemicals and demineralized water generated in a laboratory filtration system. The same water source was used to generate water used in ICP/MS analyses to dilute the analytical solution and establish the instrumental limits of detection. Brine leachant solutions were made by adding NaCl and KCl to portions of leachant solutions B7 and B4 for use in tests with Hanford-H glass. These are referred to as

leachants B7B and B4B, respectively. The concentrations of NaCl and KCl represent those of highly concentrated tuff groundwater.

The concentrations of key glass components present in the leachant solutions were measured and used as background concentrations for tests with glass. The pH values of the stock buffer solutions themselves and of solutions recovered from blank tests conducted without glass were measured. The pH values of solutions from all tests with added salt were adjusted to account for the alkaline error of the glass membrane electrode by assuming that the true pH values of the brine leachants were the same as the pH values of the corresponding leachants without added salt. (Competition with Na^+ and other alkali metal ions lowers the electrode response.) That is, the pH values measured for tests with glass in B7B leachant were adjusted by the difference between the values measured for the B7 and B7B leachants. Likewise, the pH values for solutions from tests in the B4B leachant were adjusted based on the difference between the values measured for the B4 and B4B leachants.

4. 3 RESULTS

4.3.1 Results of MCC-1 Tests with SRL 202G Glass

Test solutions were analyzed with ICP-MS. The instrument was calibrated with matrix-matched solutions, and instrument performance was tracked using quality control standards. The solution concentrations of various glass components are used to determine the extent of dissolution in each test. Differences in the concentrations attained in tests conducted for different durations are used to determine the dissolution rate. The solution concentrations are used to calculate normalized mass loss values, NL(i), by using Equation 4-5:

$$NL(i) = \frac{C(i) - C^{\circ}(i)}{(S/V) \bullet f(i)} \tag{4-5}$$

where C(i) is the concentration of element i in the test solution, C^o(i) is the concentration of element i in the blank solutions, S/V is the S/V ratio of the test, and f(i) is the mass fraction of element i in the glass. Values of C(i) and C^o(i) were calculated as the products of the measured concentrations and the dilution factors for each test solution. S is the geometric surface area of the glass and V is the volume of buffer added to the test, which was calculated from the leachant mass using a solution density of 1.00 g/mL. The mass fractions of various elements were determined from the measured composition of the glass (from Table 4-2). Normalization of the solution concentrations to S/V allows direct comparison of results for different test configurations, and normalization to *f(i)* allows direct comparison of releases of different glass components. NL(i) has the units of mass glass dissolved per unit area and time.

The glass dissolution rates were determined based on the normalized boron mass loss. The boron concentrations and values of NL(B) for MCC-1 tests with SRL 202G glass are summarized in Table 4-4 for tests at 40ºC. Values of NL(B) are plotted against the test duration in Figure 4-1 for tests conducted in each buffer solution. Linear regression lines determined using Kaleidagraph software are shown in the figures. The slopes of the fit lines give the normalized dissolution rates, NR(B). Note that the y-intercepts of all plots are positive values.

This is attributed to dissolution of high-energy sites on the glass surface that result from the 600-grit finish, e.g., material at the edges of scratches. All samples were prepared to produce a surface finish that was as uniform as possible so that all samples had a similar number of high-energy sites. Dissolution of glass at these sites is assumed to occur within the first few days and to contribute equally to all test results. Dissolution is assumed to occur from a uniform surface thereafter. The initial transient dissolution of glass from high energy sites increases NL(i) values by a constant amount, as evidenced by the nonzero y-intercepts of the regression lines. The slope of a regression line gives the glass dissolution rate. (The y-intercept is not used in the determination of the rate.) These rates are then used to determine the model parameter values in Equation 4-1 by equating the slope with the dissolution rate as:

$$\frac{\Delta NL(B)}{\Delta t} = rate_G = k_E \bullet 10^{\eta \bullet pH} \bullet \exp\left(\frac{-E_a}{RT}\right) \tag{4-6}$$

Short-term MCC-1 tests were used to determine the dissolution rate because the value of k_E remains constant under these conditions. In the Defense HLW glass degradation model, the parameter k_E represents the product of the intrinsic dissolution rate constant and the chemical affinity term. The value of the chemical affinity term remains near one as long as the concentrations of dissolved glass components remain low. Test conditions were selected so that the chemical affinity term would not affect the results except possibly at the longer test durations. However, a compromise is needed between the need to maintain solution concentrations low enough to keep the value of the affinity term near zero, but high enough to be measured reliably. The need to maintain low concentrations near the analytical detection limit often results in significant scatter in the test results. Since the values of k_E and the temperature term are constant (for all tests conducted at the same temperature), differences in the rates in different pH buffer solutions are attributed to the pH term. Taking the logarithm of Equation 4-6 gives:

$$\log rate_G = \log k_E + \log(\eta \bullet pH) - \left(\frac{E_a}{\ln 10\, RT}\right) \tag{4-7}$$

A straight-line fit to the test results is needed to estimate values of η and E_a. Linear fits to the test results are shown in Figures 4-1a through 4-1f. Uncertainty bars for each value of NL(B) are plotted as ±13, 15, or 16% depending on the propagated uncertainties. No uncertainty is assigned to the abscissa value because tests were placed in the oven and removed within 30 minutes of the same time of day, and the time required for solutions to heat up to 40ºC and cool before opening were assumed to be the same. The uncertainty in NL(B) can be compared with the residual of the linear fit (the difference between the value of the data point and the fit line). In test series at pH 4.8, 9.3, and 12, the residuals were less than the uncertainty for all tests and the rate is considered to be certain. The results in other test series were scattered and not well fit. Some results were excluded as outliers to the linear trend in tests at pH 3.7 and 8.5 to provide a conservative estimate of the rate. For example, values of NL(B) are expected to increase as the test duration increases, and tests in which NL(B) decreased with increased test durations indicate that one of the results is unreliable. The trends shown by tests at other durations were used to determine if one or both of the test results in question should be excluded from the regression. In Figures 4-1a through 4-1f, solid symbols represent test results that were included in the regression shown by the solid line and open symbols represent test results that were excluded.

The regression of test series at each pH value are discussed in the following sections and the rates are summarized in Table 4-5.

40ºC pH 1.8:
Tests conducted in the pH 1.8 solutions (Figure 4-1a) show the highest extents of reaction of all pH values that were tested. Whereas tests at 70 and 90ºC showed typical parabolic behavior, the complete set of tests at 40ºC does not show any obvious time dependence. The results of the 1-day, 2-day, 5-day, and 16-day tests are the same, within the testing uncertainty, and the results of the 3-day and 7-day tests are lower and higher, respectively. The low result of the 16-day test (relative to shorter-term tests) is probably not due to solution feedback effects, because solution feedback did not become significant until about 200 g/m^2 in tests at 70 and 90ºC. The values of NL(Si) and NL(Na) in the 16-day test are also lower than expected. A reliable dissolution rate cannot be determined from these test results for comparison with the model.

40ºC pH 3.7:
Due to the scatter in the data, it is not clear from the test results at pH 3.7 if the 16-day test results are affected by solution feedback effects. In the tests at 70ºC, feedback became significant at about 12 g/m^2. The 16-day results may be affected, but this is uncertain because of the low 10-day test result. A rate of 0.508 $g/(m^2d)$ is obtained when all results are included in the regression. The dissolution rate is 0.981 $g/(m^2d)$ if both the 10-day and 16-day results are excluded (Figure 4-1b)– the 16-day result due to suspected feedback effects and the 10-day result because it is significantly lower than the 7-day result. The higher of the two rates is preferred for comparison with the model based on the lower value of the y-intercept value and fairly good fit relative to the uncertainty bars for each NL(B) value, which are drawn at 13%.

40ºC pH 4.8:
The results of tests at pH 4.8 provide a constant rate of 0.0617 $g/(m^2d)$ (Figure 4-1c) with no outlying data. The uncertainty bars for each NL(B) value are drawn at ±13%. The positive y-intercept of the fit line is attributed to dissolution of fines and high-energy surfaces.

40ºC pH 8.5:
As shown in Figure 4-1d, the glass dissolution rate is very low at this pH, and the data are scattered. The result of the 2-day test can be excluded from the regression because it is significantly higher than the 3-, 5-, and 7-day results and similar to the 10-day and 23-day results. The 16-day result is unreliable because it is significantly lower than results from tests at shorter durations. Based on the propagated uncertainty, the uncertainty bars are plotted at ±15%. Both the 2- and 16-day results differ significantly from the line fit to the other results; excluding the 2- and 16-day results gives a rate of 0.00400 $g/(m^2d)$. This is about twice the rate obtained using all the results, which is 0.00188 $g/(m^2d)$. The rate of 0.00400 $g/(m^2d)$ is used for comparison with the model.

40ºC pH 9.3:
The results of tests at pH 9.3 provide a constant rate of 0.0171 g/(m^2d) (Figure 4-1e) with no outlying data. Based on the propagated uncertainty, the uncertainty bars are plotted at ±16%.

40ºC pH 12:
The results of tests at pH 12 provide a constant rate of 1.09 g/(m^2d) (Figure 4-1f) with no outlying data. Based on the propagated uncertainty, the uncertainty bars are plotted at ±13%.

4.3.2 Results of MCC-1 Tests with Hanford-H Glass

The pH values of the test solutions were measured at room temperature using a combination electrode that was calibrated before use with NIST-traceable buffers. The pH values of the brine leachate solutions were measured directly and then adjusted to account for the effect of the brine on the electrode response. Because the sodium and potassium concentrations were nearly the same in all brine leachates, their effect on the measured pH values was assumed to be the same for all test solutions. The pH values measured for the brine leachants themselves (i.e., the stock solutions B4B and B7B) were used to determine the magnitude of the brine effect. The difference between the values measured for leachants B4 and B4B was added to the values measured for all tests conducted in leachant B4B. The values measured for leachants B4 and B4B were 9.757 and 9.473, respectively. The difference, 0.284, was added to the pH values for all tests conducted in the B4B leachant to account for the effect of the added salts on the electrode response. Likewise, the values measured for leachants B7 and B7B were 3.687 and 2.932, respectively, so 0.755 was added to the pH values for all tests conducted in the B7B leachant. The averages of the pH values for tests in B4 buffer are 9.612 at 40ºC and 9.732 at 90ºC, and 9.645 for tests in B4B buffer at 90ºC. The averages of the pH values for tests in B7 buffer are 3.649 at 40ºC and 3.690 at 90ºC, and 3.720 for tests in B7B buffer at 90ºC. This simple approach is presumed to be adequate for the present purpose of comparing the dissolution rates in solutions with and without added salt that have nearly the same pH values.

Solutions from tests in the B4 and B7 leachants at 40 and 90ºC were analyzed with ICP-MS. Solutions from tests at 90ºC were analyzed with inductively coupled plasma-atomic emission spectroscopy (ICP-AES) because the brine solutions could not be reliably measured with ICP-MS. Those analyses did not meet QA requirements for data used in TSPA model development, and the data are referred to as "non-Q." The solutions from tests at 90ºC in both sets of leachant solutions were analyzed with ICP-AES for direct comparison. The results of ICP-AES analyses are provided for corroborative use only.

The solution concentrations of various glass components were used to determine the extent of dissolution in each test, and the extents attained in tests conducted for different durations were used to determine the dissolution rate. The solution concentrations are used to calculate normalized mass loss values, NL(i), by using Equation 4-5. The mass fractions of various elements were determined from the measured composition of the Hanford-H glass (see Table 4-2). The solution concentrations of B and the values of NL(B) for MCC-1 tests with Hanford-H glass are summarized in Table 4-6. It is important to note that NL(i) has the units of mass glass dissolved per unit area and time, not mass of the component that was used to calculate the normalized mass loss. Values of NL(B) are plotted against the test duration in Figure 4-2 for

tests conducted in different buffer solutions. Uncertainty bars are drawn at 8.4% of each NL(B) value based on the propagation of uncertainties in calculating that value. Linear regression lines determined using Kaleidagraph software are shown in the plots. Note that the y-intercepts of most regressed lines are positive values, which is usually observed in MCC-1 tests and attributed to the dissolution of glass at high-energy sites that remain on samples with a 600-grit finish. All samples were prepared with a polish that was as uniform as possible so that all samples had a similar abundance of high-energy sites. Dissolution of these sites is assumed to be complete within the first few days and to contribute equally to all test results. This provides an "offset" to these test results that affects the y-intercept, but has no effect on the slope. Only the slope of the regression line is used to determine the dissolution rate. Some results were excluded as outliers to the trend or to provide a conservative estimate of the rate. The solid symbols represent test results included in the regression and the open symbols represent test results that were excluded from the regression. This is done because the trend in dissolution with time is well established for borosilicate glasses, and deviations from the trend can be attributed to uncertainties in the test execution and solution analysis. The results for each set of test conditions are discussed below.

40ºC pH 3.7:
The regressed rate at 40ºC and pH 3.7 is 0.00712 g/(m^2d) (Figure 4-2a). Although the data show slightly negative curvature, they are well fit by the line. Excluding the 28- and 35-day tests gives a slightly higher rate of 0.0102 g/(m^2d). It is not likely that these tests are affected by solution feedback, since the silica concentration is only about 2 mg/L.

40ºC pH 9.7:
The regressed rate at 40ºC and pH 9.7 excluding the value of 0 g/m^2 at 10 days is 0.00441 g/(m^2d) (Figure 4-2b). The value of NL(B) = 0 occurs because the concentration measured in the test solution was less than that in the B4 leachant. This is a result of using small differences between large values to determine the rate.

90ºC pH 3.7:
The regressed rate at 90ºC and pH 3.7 is 0.447 g/(m^2d) (Figure 4-2c). The curvature shown by the first four tests at 90ºC may suggest that they are being affected by solution feedback, but the value of the 10-day test indicates that the value for the 7-day test is anomalously low. The 7-day result was excluded from the regression. [The rate with the 7-day test included in the regression is slightly lower: 0.368 g/(m^2d).]

90ºC pH 9.7:
The regressed rate at 90ºC and pH 9.7 is 0.342 g/(m^2d) (Figure 4-2d). These results are well fit by linear regression.

90ºC pH 3.7 Brine:
The regressed rate at 90ºC and pH 3.7 in brine is 0.230 g/(m^2d) (Figure 4-2e). These results are well fit by linear regression, except the result of the 5-day test is a little high. The rate with the 5-day test included in the regression is a few percent higher: 0.236 g/(m^2d). These are non-Q results from ICP-AES analyses.

90ºC pH 9.7 Brine:
The regressed rate at 90ºC and pH 9.7 in brine excluding the 3-day result gives a rate of 0.317 g/(m^2d) (Figure 4-2f). Including the 3-day result gives a rate of 0.356 g/(m^2d). These are non-Q results from ICP-AES analyses.

Note that the plots in Figures 4-2b and 4-2d have negative y-intercepts, which suggests that the background concentration used for leachant B4 was too high. Because the same background concentration was used for all tests in each test series, this does not affect the rates determined from the NL(B) values, except for the uncertainty in tests at 40ºC due to exclusion of the 10-day result at pH 9.7.

4.3.3 Results of Product Consistency Tests with Hanford-H Glass

Product consistency tests (PCTs) were conducted to show that the chemical durability of Hanford-H glass meets the requirement for HLW glasses and comparison with the rate calculated with the model in alkaline solutions. Normalized mass losses were calculated for several elements by using Equation 4-5 with the measured concentrations and the elemental mass fractions from Table 4-2. The boron concentrations and calculated NL(B) are included in Table 4-6. The average value of NL(B) for the three tests is 0.688 g/m^2, and the average rate over the 7-day test duration is 0.688 ÷ 7 = 0.0983 g/(m^2d). The average pH value is 10.98.

4.3.4 Results of Vapor Hydration Tests with Hanford-H Glass

The results of standard VHTs were used to determine the minimum rate in alkaline solutions for the Defense HLW glass degradation model. Standard VHTs were conducted for comparison with the model, and excess-water VHTs were conducted to study the importance of glass deliquescence and advective flux on glass degradation. Two excess-water VHTs and 4 standard VHTs were conducted at both 150ºC and 200ºC. Excess-water VHTs were also conducted at 70 and 90ºC (duplicate tests), and at 40ºC (single test). A single blank test was conducted at 90ºC. The matrix of VHTs is included in Table 4-1. The extent of glass degradation was determined by the thickness of the alteration layers that formed in the standard VHTs and by the mass of boron released from the glass into the solution in the excess-water VHTs. The thickness of the layer is assumed to be proportional to its volume, which can be represented as a normalized mass loss using the density of the reacted glass (see below). The amounts of B, Na, and Si that dripped from the glass sample into the vessel bottom were measured to compare the glass dissolution rates calculated with the model.

4.3.5 Results of Measured Layer Thickness for Standard VHTs and Excess-Water VHTs with Hanford-H Glass

To measure the thickness of layers formed on VHT-reacted samples, the samples were fixed in epoxy and cut perpendicular to the sample faces to generate cross sections. The altered surface layers formed the perimeters of the cross-sections. The cross sections were mechanically polished and the thicknesses of the alteration layers formed on the two sample faces were measured with an SEM. The layer around the perimeter of the cross-sectioned sample was examined and several representative micrographs were acquired to document the layer thickness.

A typical cross section is shown in Figure 4-3. (A scale bar is drawn below the figure because the scale bar on the photomicrograph is difficult to see.) The alteration layers formed on most samples were easily distinguished from the underlying glass. The outer surfaces of most layers (adjacent to the epoxy) had a coarse-grained appearance and the interface with the underlying glass was visible due to contrast difference or separation of the layer from the glass, as seen in Figure 4-3. The sample shown in Figure 4-3 had reacted in an excess-water VHT at 150ºC for a total of 63 days with 5 solution exchanges. The striations parallel to the sample surface (these are vertical in the photomicrograph) probably result from changes in the solution chemistry that occur during the exchanges. The bright regions near the center of the layer at the bottom of the photomicrograph are enriched in iron relative to the layer and glass. The enrichment must have occurred during the test, since similar regions were not detected within the underlying glass.

The layer thickness was determined as the average of thicknesses measured in typically 9 to 12 locations about the perimeter. The thickness was determined by using an architect's scale to measure both the thickness of the layer on the SEM photomicrograph and the length of the scale bar provided on the SEM photomicrograph. The layer thickness in micrometers was calculated by multiplying the layer thickness measured using the architect's scale by the length of the SEM scale bar in micrometers, then dividing that product by the length of the SEM scale bar measured with the architect's scale. For example, the thickness of the layer at the top of the image in Figure 4-3 was measured to be 54-fiftieths of an inch and the length of the scale bar was measured to be 55-fiftieths of an inch. The scale bar represents 21 μm, so the layer thickness is (54/50 in.) x (21 μm) ÷ (55/50 in.) = 20.6 μm. Note that the same methodology was used to verify the calibration of the SEM by using a NIST magnification standard. The thicknesses of the layer at the top, middle, and bottom of each photomicrograph were measured and the average layer thickness determined for each sample. The averages and standard deviations of the measured layer thicknesses are summarized in Table 4-7.

The results of standard VHTs are plotted in Figure 4-4. For a given test duration, the layers formed on samples reacted in tests at 200ºC were thicker than layers formed on samples in tests at 150ºC. In contrast, the layers formed on samples in excess-water VHTs at 150ºC were thicker than those formed in tests at 200ºC after the same test duration (see Table 4-7). The layer thickness represents the balance between the penetration of water into the glass (the layer/glass interface) and dissolution of the layer (the outer surface of the layer). Dissolution of the outer surface is negligible in standard VHTs because the solution is static, but can be more extensive in excess-water VHTs because of refluxing. The amount of silicon released into solution in excess-water VHTs provides a measure of how much of the layer dissolved during the test.

The difference between layer thicknesses in standard and excess-water VHTs at each temperature is attributed to differences in the compositions of the solutions formed on the samples during the tests. Highly concentrated solutions are generated in the standard VHTs because dissolved glass components are confined to the solution condensed on the sample and the volume of that solution is fixed. In standard VHTs conducted with many glasses, alteration phases that consumed silica formed and lead to an increase in the dissolution rate. However, alteration phases that consume dissolved silica did not form in the standard VHTs with Hanford-H glass conducted in this study.

Due to the limited volume of water contacting glass under standard VHT conditions, the transformation of glass to alteration phases occurs essentially *in situ*, and glass is replaced by alteration phases (primarily clays) nearly isovolumetrically. Therefore, the volume of alteration phases is nearly equal to the volume of glass that has reacted. For the small amounts of glass that are altered in these tests, the thickness of the alteration layer is proportional to its volume, which can be related to the amount of reacted glass using the glass density. The normalized mass loss can be calculated by simply dividing the layer thickness by the density of the glass:

$$layer\ thickness, \mu m \bullet \left(density, \frac{g}{cm^3} \right) \bullet \left(\frac{1\ cm^3}{1 \mu m \bullet m^2} \right) = normalized\ mass\ loss, \left(\frac{g}{m^2} \right) \quad (4\text{-}8)$$

Similarly, the normalized dissolution rate can be calculated from the change in layer thickness with reaction time. This allows for comparison with normalized mass loss values calculated with measured solution concentrations in other tests. The results of the standard VHTs conducted at 200ºC do not show obvious time dependence, but upper bounding rates can be determined with lines drawn from the origin and converted to normalized mass loss using Equation 4-8 with a glass density of 2.73 g/cm^3. The limiting rates for the layer thicknesses plotted in Figure 4-4 are calculated to be 0.021 μm/d x 2.73 g/cm^3 = 0.057 g/(m^{2}d) at 150ºC and 0.20 μm/d x 2.73 g/cm^3 = 0.55 g/(m^{2}d) at 200ºC.

4.3.6 Results of Solution Analyses for Excess-Water VHTs with Hanford-H Glass

The excess-water VHTs were designed to provide a measure of the amounts of various glass components that can be flushed from the surface during the test due to the reflux of water. The concentrations of B and Si were measured in successive samplings and used to calculate NL(B) and NL(Si) for each sampling interval. The cumulative release of B was used to determine the degradation rate of the samples. The interval and cumulative values of NL(B) and NL(Si) are summarized in Table 4-8. Values of NL(B) are higher than values of NL(Si) for each sampling. This is commonly observed in immersion tests with borosilicate glasses and occurs because B is more easily freed from the glass than Si in alkaline solutions, and because not all of the Si released from the glass matrix enters solution. Most Si released from the glass in VHTs is incorporated into alteration phases (e.g., the alteration layer), whereas little, if any, B is incorporated into alteration phases. As was done for immersion tests, the release of B was used to determine the glass dissolution rate in the excess-water VHTs. The cumulative NL(B) values are plotted against the cumulative test duration for tests at 200, 150, 90, and 70ºC in Figures 4-5a through 4-7d, respectively. The results of tests at 40ºC are shown in Figure 4-5e, but the boron concentrations were not distinguishable from background levels in the blank test run at 90ºC, so the rate determined from the 40ºC results is considered to be an upper bound.

The results of tests at 40, 70, and 90ºC are well fit by linear regressions. The data for duplicate tests at 150 and 200ºC are both well represented by power law functions, as shown in the plots, although the mechanism responsible for the observed time dependence is not known. Changes in the reflux rates could occur due to changes in the RH as the solution concentrations in water on the test specimens and in the bottom of the vessel evolve. This could affect both the water condensation rate and solution drip rate. The observed rollover could also be due to the formation of thick alteration layers that act as diffusion barriers. Other experiments are needed

to understand the reflux dynamics in the excess-water VHTs and the advection rates that could occur in the disposal system. To facilitate comparisons with other tests, the results of tests at 150 and 200ºC through 28 days were regressed linearly to provide bounding rates prior to the rollover. The regressed slopes for the combined results of duplicate tests at 70, 90, 150, and 200ºC are 0.0135, 0.138, 1.36, and 0.657 g/(m^2d), respectively. These rates can be compared with each other, with the rates measured under other test conditions, and with the rates calculated with the Defense HLW glass degradation model. The release rates of boron in these tests are affected by both the dissolution rate of the glass and the reflux rate of water at each temperature. Although the dissolution rates of borosilicate glasses are known to increase with temperature, more boron was released in excess-water VHTs at 150ºC than at 200ºC. From the linear fit to the short-term results, the initial difference in rates between 150ºC and 200ºC is a factor of 2 *decrease*. The rates measured at 70, 90, and 150ºC *increase* by about a factor of ten.

The solution pH values provide further insight into the glass degradation rates. The solution pH increases primarily due to dealkalization reactions. Although the dealkalization reactions are mechanistically independent of the hydrolysis reactions through which matrix degradation occurs, the dealkalization and hydrolysis reactions are linked through the solution pH. An increase in pH due to dealkalization reactions will increase the rates of hydrolysis reactions. The pH of the solution in the bottom of the vessel was measured. The pH of that solution is probably lower than that of the solution contacting the glass. The compositions of the solutions on the samples will depend on the relative rates of water vapor condensation, which lowers the concentrations, and glass dissolution, which increases the concentrations. The solution concentrations in the vessel bottom depend on the relative rates of solution dripping from the samples and water evaporating, both of which tend to increase solution concentrations. Refluxing will tend to equalize the compositions of the solutions on the glass and in the vessel bottom, and the accumulation of B in the solution in the vessel bottom is assumed to be representative of its release rate from the glass.

The average pH values for those solutions sampled in the excess-water VHTs that were used to determine the rate are summarized in Table 4-9. The average pH value for the solutions from tests at 150ºC is 1.41 units higher than that for tests at 200ºC. The higher pH values both indicate that the degradation rate is higher at 150ºC and act to further increase the rate as corrosion proceeds. Although the reactions that occur as glass degrades are all thermally activated and the rates of individual reactions increase with temperature, the glass degradation rate is complicated by solution feedback effects that counteract the effects of temperature and pH. The effects of solution feedback are represented by the chemical affinity term, which is included as a component of k_E in the model rate equation. In the excess-water VHTs, differences in the reflux conditions at different temperatures probably affect the chemical affinity and glass degradation rate. The effects of reflux on the dissolution rate are not considered explicitly in the model, but may be presumed to be bounded by the range of values of k_E.

Finally, the rates determined from solution analysis and measurement of the layer thickness can be compared for excess-water VHTs conducted at 150 and 200ºC. The relative amounts of boron and silicon released into solution in excess-water VHTs provide an estimate of how much layer dissolved during the test. It can be assumed that all of the boron but none of the silicon is totally depleted from the layer, and that the difference in the layer thicknesses

calculated from NL(B) and NL(Si) represents the remaining layer. For example, in test VHan(150)-1, the cumulative values of NL(B) and NL(Si) are 62.0 and 21.6 g/m^2, respectively (see Table 4-8 entries for final interval VHan(150)-1-6). Using these values in Equation 4-8 gives thicknesses of 62.0 $g/m^2 \div 2.73\ g/cm^3 = 22.7\ \mu m$ and 21.6 $g/m^2 \div 2.73\ g/cm^3 = 7.9\ \mu m$, a difference of 14.8 μm. This is in good agreement with the measured layer thicknesses of the two samples in test VHan(150)-1, which are 14.3 and 19.2 μm (see Table 4-7), an average of 16.8 μm. For the other tests, the layer thickness are calculated to be 17.0 μm and measured to be 21.3 μm for VHan(150)-2; calculated to be 10.7 μm and measured to be 9.4 μm for VHan(200)-1; and calculated to be 10.1 μm and measured to be 9.6 μm for VHan(200)-2.

Table 4-1. Matrix of Tests

Test Number	Temp., °C	Nominal Leachant pH	Duration, Days	Test Number	Temp., °C	Nominal Leachant pH	Duration, Days
MCC-1 Tests with SRL 202G Glass							
GB1-40-1	40	1.3	1	GB3-40-4	40	8.5	7
GB1-40-2	40	1.3	2	GB3-40-5	40	8.5	10
GB1-40-3	40	1.3	3	GB3-40-6	40	8.5	16
GB1-40-4	40	1.3	5	GB3-40-7	40	8.5	23
GB1-40-5	40	1.3	7	GB4-40-1	40	9.4	2
GB1-40-6	40	1.3	16	GB4-40-2	40	9.4	3
GB7-40-1	40	3.5	2	GB4-40-3	40	9.4	5
GB7-40-2	40	3.5	3	GB4-40-4	40	9.4	7
GB7-40-3	40	3.5	5	GB4-40-5	40	9.4	10
GB7-40-4	40	3.5	7	GB6-40-1	40	12	1
GB7-40-5	40	3.5	10	GB6-40-2	40	12	2
GB7-40-6	40	3.5	16	GB6-40-3	40	12	3
GB2-40-1	40	5.0	2	GB6-40-4	40	12	5
GB2-40-2	40	5.0	3	GB6-40-5	40	12	7
GB2-40-3	40	5.0	5	GB7-40-B1	40	3.5	10
GB2-40-4	40	5.0	7	GB2-40-B1	40	5.0	10
GB2-40-5	40	5.0	10	GB3-40-B1	40	8.5	10
GB3-40-1	40	8.5	2	GB4-40-B1	40	9.4	10
GB3-40-2	40	8.5	3	GB6-40-B1	40	12	10
GB3-40-3	40	8.5	5				
MCC-1 Tests with Hanford-H Glass							
HB4-40-1	40	3.7	17	HB7-40-1	40	9.6	17
HB4-40-2	40	3.7	21	HB7-40-2	40	9.6	21
HB4-40-3	40	3.7	10	HB7-40-3	40	9.6	10
HB4-40-4	40	3.7	28	HB7-40-4	40	9.6	28
HB4-40-5	40	3.7	35	HB7-40-5	40	9.6	35
HB4-90-1	90	3.7	2	HB7-90-1	90	9.6	2
HB4-90-2	90	3.7	3	HB7-90-2	90	9.6	3
HB4-90-3	90	3.7	5	HB7-90-3	90	9.6	5
HB4-90-4	90	3.7	7	HB7-90-4	90	9.6	7
HB4-90-5	90	3.7	10	HB7-90-5	90	9.6	10
MCC-1 Tests with Hanford-H Glass in Brine Solutions							
HB4B-90-1	90	3.7	2	HB7B-90-2	90	9.6	3
HB4B-90-2	90	3.7	3	HB7B-90-3	90	9.6	5
HB4B-90-3	90	3.7	5	HB7B-90-4	90	9.6	7
HB4B-90-4	90	3.7	7	HB7B-90-5	90	9.6	10
HB4B-90-5	90	3.7	10	HB4B-90-B1	90	3.7	3
HB7B-90-1	90	9.6	2	HB7B-90-B1	90	9.6	3
Product Consistency Tests with Hanford-H Glass							
PHanH-1	90		7	PHanH-B1	90		7
PHanH-2	90		7	PHanH-B2	90		7
PHanH-3	90		7				

Table 4-1. (contd.)

Test Number	Temp., ºC	Duration, Days	Test Number	Temp., ºC	Duration, Days
Excess-Water Vapor Hydration Tests with Hanford-H Glass					
VHan(40)-1-1	40	7 (7)[a]	VHan(90)-BL-5	90	28 (119)
VHan(40)-1-2	40	26 (33)	VHan(90)-BL-6	90	24 (143)
VHan(40)-1-3	40	30 (63)	VHan(150)-1-1	150	7 (7)
VHan(40)-1-4	40	28 (91)	VHan(150)-1-2	150	7 (14)
VHan(40)-1-5	40	28 (119)	VHan(150)-1-3	150	7 (21)
VHan(40)-1-6	40	24 (143)	VHan(150)-1-4	150	7 (28)
VHan(70)-1-1	70	14 (14)	VHan(150)-1-5	150	14 (42)
VHan(70)-1-2	70	16 (30)	VHan(150)-1-6	150	22 (63)
VHan(70)-2-1	70	14 (14)	VHan(150)-2-1	150	7 (7)
VHan(70)-2-2	70	16 (30)	VHan(150)-2-2	150	7 (14)
VHan(90)-1-1	90	7 (7)	VHan(150)-2-3	150	7 (21)
VHan(90)-1-2	90	26 (33)	VHan(150)-2-4	150	7 (28)
VHan(90)-1-3	90	30 (63)	VHan(150)-2-5	150	14 (42)
VHan(90)-1-4	90	28 (91)	VHan(150)-2-6	150	22 (63)
VHan(90)-1-5	90	28 (119)	VHan(200)-1-1	200	7 (7)
VHan(90)-1-6	90	24 (143)	VHan(200)-1-2	200	7 (14)
VHan(90)-2-1	90	7 (7)	VHan(200)-1-3	200	7 (21)
VHan(90)-2-2	90	26 (33)	VHan(200)-1-4	200	7 (28)
VHan(90)-2-3	90	30 (63)	VHan(200)-1-5	200	14 (42)
VHan(90)-2-4	90	28 (91)	VHan(200)-1-6	200	22 (63)
VHan(90)-2-5	90	28 (119)	VHan(200)-2-1	200	7 (7)
VHan(90)-2-6	90	24 (143)	VHan(200)-2-2	200	7 (14)
VHan(90)-BL-1	90	7 (7)	VHan(200)-2-3	200	7 (21)
VHan(90)-Bl-2	90	26 (33)	VHan(200)-2-4	200	7 (28)
VHan(90)-BL-3	90	30 (63)	VHan(200)-2-5	200	14 (42)
VHan(90)-BL-4	90	28 (91)	VHan(200)-2-6	200	22 (63)
Standard Vapor Hydration Tests with Hanford-H Glass					
VHan(150)-3a	150	42	VHan(200)-3	200	14
VHan(150)-3b	150	84 (176)	VHan(200)-4a	200	42
VHan(150)-4a	150	28	VHan(200)-4b	200	39 (82)
VHan(150)-4b	150	133 (161)	VHan(200)-5	200	66
VHan(150)-5	150	81	VHan(200)-6a	200	28
VHan(150)-6	150	66	VHan(200)-6b	200	40 (83)

[a]Values in parentheses are cumulative test durations.

Table 4-2. Glass Compositions, Mass Fraction

Element	SRL 202G	Hanford-H	Element	SRL 202G	Hanford-H
Al	0.0307	0.0132	Mo	0.000072	
B	0.0321	0.0268	Na	0.114	0.0576
Ba	0.00027		Nd	0.00011	
Ca	0.00768	0.00929	Ni	0.0075	0.00190
Cr	0.00283		P	0.00140	0.00190
Cu	0.000964		Pb	0.00037	
Fe	0.0648	0.0381	Si	0.208	0.210
K	0.0274		Sr	0.00014	0.0240
La	0.00014		Ti	0.00076	
Li	0.0160	0.0220	U	0.0134	
Mg	0.0102		Zn	0.00011	0.0146
Mn	0.00977	0.0127	Zr	0.00060	0.0376

Table 4-3. Nominal Buffer Compositions and pH Values

Index	Nominal pH	Nominal Composition[a]	Batched Chemicals
B1	1.3	0.05 m KCl + 0.05 m HNO_3	3.7254 g KCl 3.1550 g 70% HNO_3 993.5 g demineralized water
B7	3.5	0.05 KHpH + 0.005 m HNO_3	10.2662 g KHpH 0.4711 g 70% HNO_3 999.5 g demineralized water
B7B	3.5[b]	0.05 KHpH + 0.005 m HNO_3 + 3.3 m NaCl + 0.30 m KCl	150.04 g B7 leachant 28.98 g NaCl 3.38 g KCl
B2	5.0	0.0095 KHpH + 0.00266 m $LiOH \bullet H_2O$	1.9412 g KHpH 0.1117 g $LiOH \bullet H_2O$ 998.0 g demineralized water
B3	8.5	0.025 m tris+ 0.008 m HNO_3	3.0358 g tris 0.8008 g 70% HNO_3 996.3 g demineralized water
B4	9.3	0.05 m tris + 0.0038 m HNO_3	6.0568 g tris 0.3443 g 70% HNO_3 993.8 g demineralized water
B4B	9.3[b]	0.05 m tris + 0.0038 m HNO_3 + 3.3 m NaCl + 0.30 m KCl	149.97 g B4 29.05 g NaCl 3.39 g KCl
B5	10.0	0.00144 m $LiOH \bullet H_2O$ + 0.00117 m HNO_3	0.0627 g $LiOH \bullet H_2O$ 1.007 g 70% HNO_3 1000.0 g demineralized water
B6	12.0	0.00505 m LiCl + 0.0107 m $LiOH \bullet H_2O$	0.214 g LiCl 0.449 g $LiOH \bullet H_2O$ 999.35 g demineralized water

[a]KHpH = potassium hydrogen phthalate and tris = trishydroxymethyl aminomethane.
[b]Assumed value.

Table 4-4. Measured Boron Concentrations and NL(B) for Tests with SRL 202G Glass at 40ºC

Test Number	Duration, Days	pH	B, µg/L	NL(B), g/m^2
B1-40-7-B1	10	1.53	10.1	--
GB1-40-1	1	1.86	29500	92.0
GB1-40-2	2	1.79	28500	80.9
GB1-40-3	3	1.69	22900	71.7
GB1-40-4	5	1.75	28700	89.9
GB1-40-5	7	1.76	37500	117
GB1-40-6	16	1.78	27200	84.9
B7-40-7-B1	10	3.64	15.4	--
GB7-40-1	2	3.68	1490	4.62
GB7-40-2	3	3.64	1240	3.86
GB7-40-3	5	3.76	2060	6.42
GB7-40-4	7	3.75	2900	9.05
GB7-40-5	10	3.70	2310	7.20
GB7-40-6	16	3.75	3750	11.7
B2-40-7-B1	10	4.75	8.21	--
GB2-40-1	2	4.79	183	0.542
GB2-40-2	3	4.80	213	0.634
GB2-40-3	5	4.81	219	0.654
GB2-40-4	7	4.81	295	0.891
GB2-40-5	10	4.80	339	1.03
B3-40-7-B1	10	8.46	5.51	--
GB3-40-1	2	8.44	76.0	0.221
GB3-40-2	3	8.44	63.5	0.167
GB3-40-3	5	8.46	60.2	0.157
GB3-40-4	7	8.46	65.3	0.173
GB3-40-5	10	8.46	79.0	0.216
GB3-40-6	16	8.58	59.7	0.155
GB3-40-7	23	8.69	86.5	0.238
B4-40-7-B1	10	9.28	10.7	--
GB4-40-1	2	9.28	43.1	0.103
GB4-40-2	3	9.26	43.3	0.104
GB4-40-3	5	9.27	59.0	0.153
GB4-40-4	7	9.25	72.1	0.194
GB4-40-5	10	9.27	83.3	0.229
B6-40-7-B1	10	11.98	15.8	--
GB6-40-1	1	11.98	414	1.26
GB6-40-2	2	11.98	715	2.20
GB6-40-3	3	11.98	1330	4.14
GB6-40-4	5	11.96	1960	6.11
GB6-40-5	7	11.97	2450	7.65

Table 4-5. Summary of Rates Regressed from Tests at 40ºC with SRL 202G Glass

Nominal pH	Data Regressed	Rate, g/(m^2d)	log(rate)	R^2
3.7	Excluding 10-day and 16-day results	0.981	-0.00833	0.890
4.8	All results	0.0617	-1.21	0.952
8.5	Excluding 2-day and 16-day results	0.00400	-2.40	0.816
9.3	All results	0.0171	-1.77	0.975
12.0	All results	1.09	0.0374	0.978

Table 4-6. Boron Concentrations and NL(B) for MCC-1 Tests and PCTs with Hanford-H Glass

Test Number	Duration, Days	B, µg/L	NL(B), g/m^2		Test Number	Duration, Days	B, µg/L	NL(B), g/m^2
MCC-1 Tests (Q)					MCC-1 Tests in Brine Leachants (non-Q)			
HB4-40-1	17	82.0	0.00786		HB4B-90-1	2	351	1.60
HB4-40-2	21	89.9	0.0371		HB4B-90-2	3	281	1.23
HB4-40-3	10	64.7	0		HB4B-90-3	5	501	2.40
HB4-40-4	28	96.4	0.0617		HB4B-90-4	7	681	3.35
HB4-40-5	35	104	0.0908		HB4B-90-5	10	811	4.06
HB7-40-1	17	129	0.186		HB7B-90-1	2	300	1.33
HB7-40-2	21	146	0.250		HB7B-90-2	3	340	1.55
HB7-40-3	10	115	0.134		HB7B-90-3	5	540	2.62
HB7-40-4	28	153	0.276		HB7B-90-4	7	520	2.51
HB7-40-5	35	162	0.310		HB7B-90-5	10	651	3.21
					Blank Tests (non-Q)			
HB4-90-1	2	176	0.514					
HB4-90-2	3	236	0.838		HB4B-90-B1	3	<50	--
HB4-90-3	5	297	1.15		HB7B-90-B1	3	<50	--
HB4-90-4	7	411	1.76		B4B leachant[c]	--	<50	--
HB4-90-5	10	710	3.37		B7B leachant[c]	--	<50	--
					PCTs (Q)			
HB7-90-1	2	382	1.61					
HB7-90-2	3	463	2.05					
HB7-90-3	5	503	2.26		PHanH-1	7	36100	0.676
HB7-90-4	7	531	2.40		PHanH-2	7	36500	0.686
HB7-90-5	10	1051	5.18		PHanH-3	7	37500	0.701
B4 leachant[a]	--	79.7	--		PHanH-B1	7	19.7	--
B7 leachant[a]	--	79.2	--		PHanH-B2	7	13.1	--
B4 leachant[b]	--	<50	--					
B7 leachant[b]	--	<50	--					

[a]Analyzed with 40ºC tests; used as background concentration for leachant.
[b]Analyzed with 90ºC MCC-1 test solutions; 50 µg/L used as background concentration for leachant.
[c]Analyzed with 90ºC MCC-1 test solutions; 50 µg/L used as background concentration for brine leachant.

Table 4-7. Layer Thicknesses for VHT Samples of Hanford-H Glass

		Sample A		Sample B	
Test No.	Duration, Days	Sample No.	Thickness, μm	Sample No.	Thickness, μm
Excess-Water VHTs					
VHan(150)-1	66[a]	H41	14.3 ± 2.6	H42	19.2 ± 1.1
VHan(150)-2	66[a]	H43	20.1 ± 1.9	H44	22.5 ± 2.3
VHan(200)-1	66[a]	H37	9.6 ± 0.8	H38	9.2 ± 0.5
VHan(200)-2	66[a]	H39	10.2 ± 0.6	H40	8.9 ± 0.9
Standard VHTs					
VHan(150)-3	126[a]	H45	2.2 ± 0.5	H60	2.4 ± 0.3
VHan(150)-4	161[a]	H59	not measured	H52	not measured
VHan(150)-5	81	H48	1.4 ± 0.1	H57	1.2 ± 0.1
VHan(150)-6	66	H50	1.4 ± 0.3	H58	1.3 ± 0.1
VHan(200)-3	14	H49	2.1 ± 0.2	H53	2.7 ± 0.5
VHan(200)-4	82[a]	H46	3.7 ± 0.6	H54	3.8 ± 0.5
VHan(200)-5	66	H47	2.4 ± 0.4	H55	3.3 ± 0.5
VHan(200)-6	81[a]	H51	2.1[b]	H56	not measured

[a]Cumulative duration.
[b]Average of two measurements.

Table 4-8. B and Si Concentrations and Calculated NL(i) for Excess-water VHTs with Hanford-H Glass

Test Number	Interval, Days	Cumulative Time, Days	B, mg/L	Interval NL(B), g/m^2	Cumulative NL(B), g/m^2	Si, mg/L	Interval NL(Si), g/m^2	Cumulative NL(Si), g/m^2
VHan(40)-1-1	7	7	0.103	0.0331	0.0331	3.36	0.137	0.137
VHan(40)-1-2	26	33	0.0942	0.0300	0.0629	0.412	0.0168	0.153
VHan(40)-1-3	30	63	0.104	0.0334	0.0965	0.280	0.0114	0.165
VHan(40)-1-4	28	91	0.0634	0.0203	0.117	0.150	0.0061	0.171
VHan(40)-1-5	28	119	0.0601	0.0192	0.136	0.262	0.0107	0.182
VHan(40)-1-6	24	143	0.0835	0.0266	0.162	0.240	0.00975	0.191
VHan(70)-1-1	14	14	0.671	0.197	0.197	1.10	0.323	0.323
VHan(70)-1-2	16	30	0.865	0.256	0.454	1.28	0.379	0.703
VHan(70)-2-1	14	14	0.651	0.185	0.185	2.25	0.640	0.640
VHan(70)-2-2	16	30	0.617	0.176	0.361	1.08	0.308	0.948
VHan(90)-1-1	7	7	1.36	0.440	0.440	6.45	0.267	0.27
VHan(90)-1-2	26	33	10.6	3.41	3.85	19.0	0.783	1.05
VHan(90)-1-3	30	63	12.7	4.11	7.97	22.1	0.915	1.97
VHan(90)-1-4	28	91	13.1	4.27	12.26	21.2	0.881	2.86
VHan(90)-1-5	28	119	11.6	3.76	15.95	23.0	0.949	3.79
VHan(90)-1-6	24	143	10.3	3.32	19.27	13.6	0.562	4.35
VHan(90)-2-1	7	7	1.06	0.349	0.349	8.96	0.376	0.376
VHan(90)-2-2	26	33	11.8	3.87	4.22	23.4	0.984	1.36
VHan(90)-2-3	30	63	12.9	4.27	8.54	43.6	1.85	3.22
VHan(90)-2-4	28	91	10.7	3.51	11.96	13.7	0.577	3.77
VHan(90)-2-5	28	119	12.9	4.29	16.4	41.0	1.74	5.55
VHan(90)-2-6	24	143	7.84	2.60	18.9	15.5	0.654	6.18
VHan(150)-1-1	7	7	49.7	13.1	13.1	74.5	2.52	2.52
VHan(150)-1-2	7	14	44.6	11.8	24.9	78.7	2.66	5.18
VHan(150)-1-3	7	21	37.7	9.93	34.8	198	6.67	11.8
VHan(150)-1-4	7	28	29.3	7.76	42.7	86.9	2.93	14.8
VHan(150)-1-5	14	42	38.0	10.1	53.1	101	3.43	18.3
VHan(150)-1-6	22	63	32.1	8.61	62.0	93.0	3.18	21.6
VHan(150)-2-1	7	7	50.8	13.1	13.1	81.9	2.70	2.70
VHan(150)-2-2	7	14	43.9	11.4	24.5	104	3.43	6.14
VHan(150)-2-3	7	21	33.8	8.69	33.1	82.7	2.72	8.82
VHan(150)-2-4	7	28	27.7	7.12	40.2	54.9	1.80	10.6
VHan(150)-2-5	14	42	40.5	10.6	51.6	130	4.34	15.2
VHan(150)-2-6	22	63	80.3	20.5	70.8	298	9.72	24.5
VHan(200)-1-1	7	7	31.4	8.45	8.45	16.4	0.564	0.56
VHan(200)-1-2	7	14	24.9	6.77	15.3	25.9	0.899	1.47
VHan(200)-1-3	7	21	22.1	5.96	21.2	37.3	1.29	2.74
VHan(200)-1-4	7	28	11.1	2.99	24.1	2.64	0.0907	2.83
VHan(200)-1-5	14	42	16.8	4.53	28.6	43.2	1.48	4.31
VHan(200)-1-6	22	63	20.4	5.48	34.0	14.8	0.507	4.80
VHan(200)-2-1	7	7	37.6	10.3	10.3	22.7	0.789	0.789
VHan(200)-2-2	7	14	18.6	5.09	15.4	10.3	0.359	1.15
VHan(200)-2-3	7	21	12.5	3.46	18.9	16.1	0.565	1.72
VHan(200)-2-4	7	28	12.6	3.45	22.2	24.7	0.862	2.57
VHan(200)-2-5	14	42	20.8	5.65	27.8	46.7	1.62	4.18
VHan(200)-2-6	22	63	23.8	6.46	34.2	68.5	2.37	6.54

Table 4-9. Summary of Degradation Rates for Hanford-H Glass Based on NL(B)

pH	Temp., °C	Test Type	Degradation Rate, g/(m^{2}d)			
			Measured	Maximum from Model	Mean from Model	Minimum from Model
3.7	40	MCC-1 test	7.12×10^{-3}	1.19	0.396	8.68×10^{-4}
9.7	40	MCC-1 test	4.41×10^{-3}	7.36×10^{-3} [a]	2.46×10^{-3}	5.87×10^{-6}
3.7	90	MCC-1 test	0.447	6.12	2.04	4.48×10^{-3}
9.7	90	MCC-1 test	0.342	0.238[b]	0.0796	1.93×10^{-4}
10.98	90	PCT	0.0983	0.982	0.328	7.98×10^{-4}
7.32	40	Excess-Water VHT	$<1 \times 10^{-3}$	0.0204	6.80×10^{-4}	1.49×10^{-5}
7.50	70	Excess-Water VHT	0.0135	0.0513	0.0171	3.79×10^{-5}
9.45	90	Excess-Water VHT	0.138	0.184	0.0614	1.49×10^{-4}
10.32	150	Excess-Water VHT	1.90[c]	11.9	3.99	9.70×10^{-3}
8.91	200	Excess-Water VHT	1.33[c]	19.5	6.52	0.0158
12[d]	150	Standard VHT	<0.057	79.3	26.5	0.0645
12[d]	200	Standard VHT	<0.55	631	211	0.513

[a] Forward rate = 0.0239 g/(m^{2}d).
[b] Forward rate = 0.920 g/(m^{2}d).
[c] Maximum rate from average of 7-day results.
[d] pH in all standard VHTs is assumed to be 12.

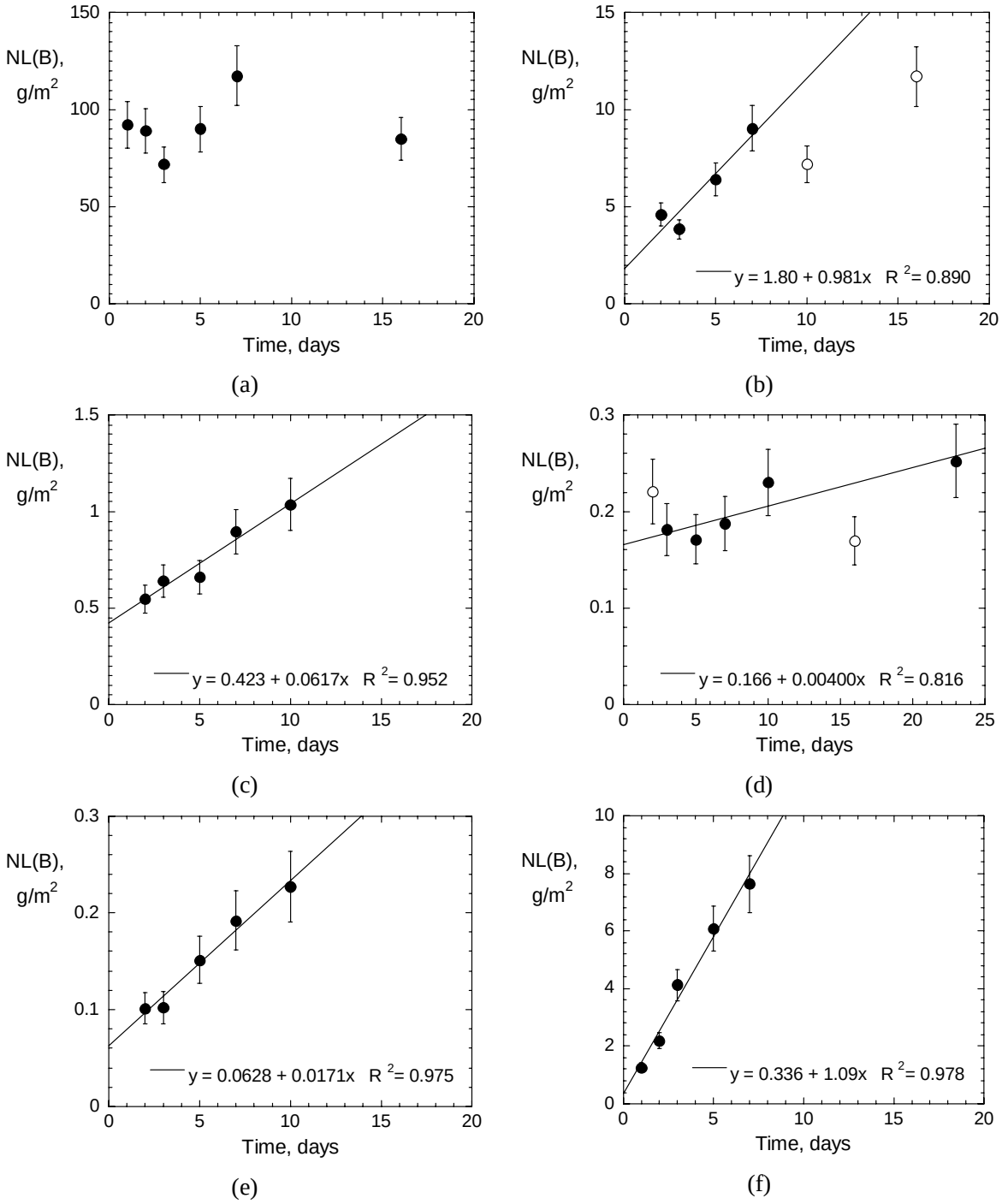

Fig. 4-1. Results of MCC-1 Tests Conducted with SRL 202G Glass in pH Buffers at 40ºC: (a) pH 1.8, (b) pH 3.7, (c) pH 4.8, (d) pH 8.5, (e) pH 9.3, and (f) pH 12. Lines show linear regression fit to data. Solid symbols included in regression and open symbols excluded from regression.

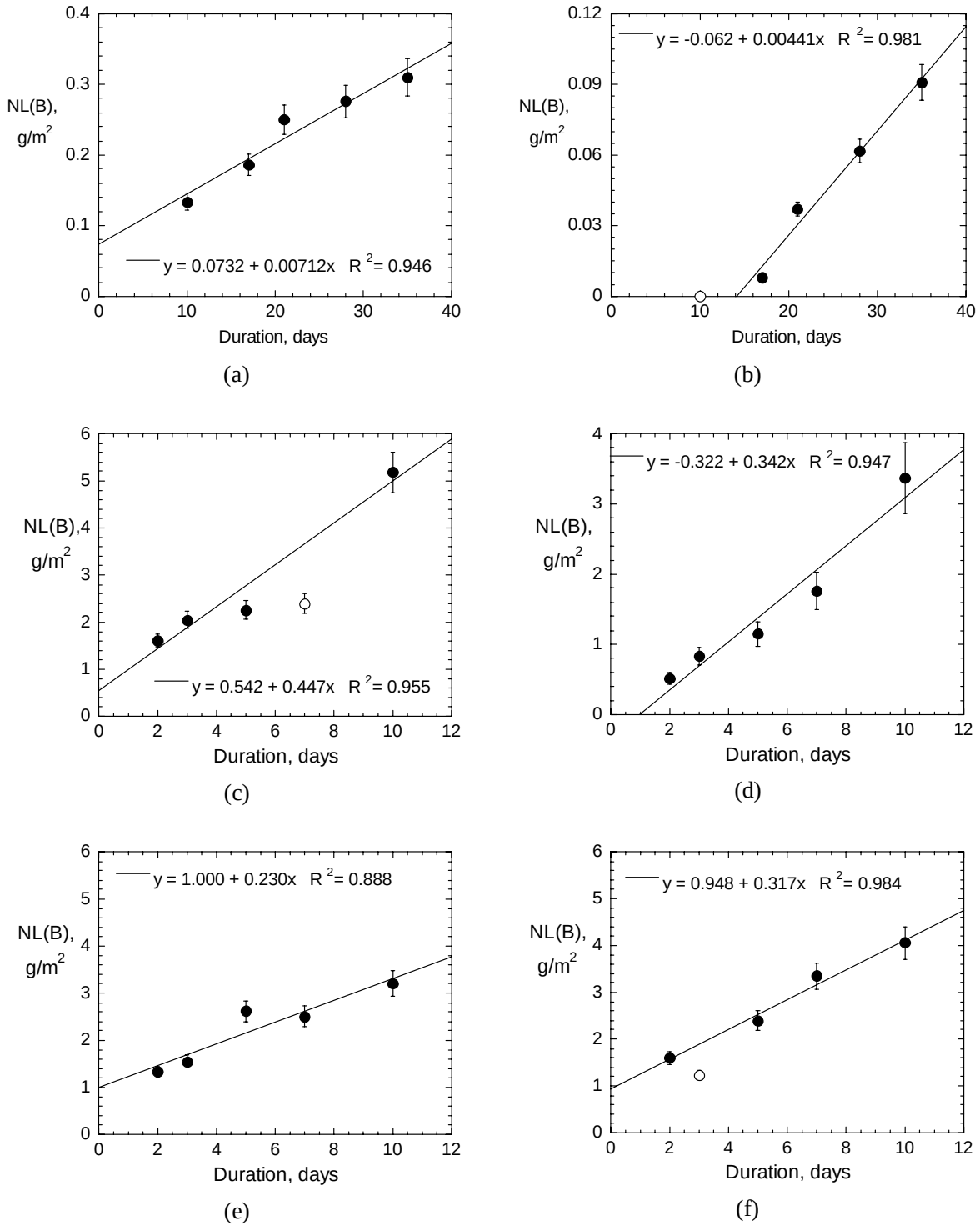

Fig. 4-2. Results of MCC-1 Tests Conducted with Hanford-H Glass in pH Buffers at (a) 40ºC at pH 3.7, (b) 40ºC at pH 9.7, (c) 90ºC at pH 3.7, (d) 90ºC at pH 9.7, (e) 90ºC at pH 3.7 in Brine Leachant (non-Q results), and (f) 90ºC at pH 9.7 in Brine Leachant (non-Q results). Lines show linear regression fit to data. Open symbols were excluded from the regression.

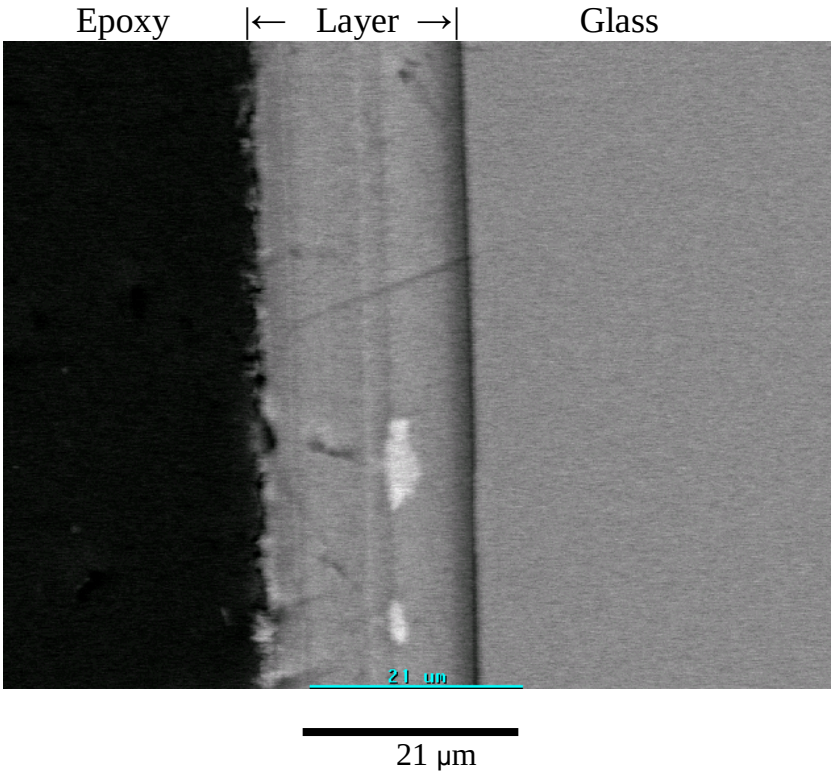

Fig. 4-3. Photomicrograph of Cross-Section of Sample H44 from Test VHanH(150)-2.

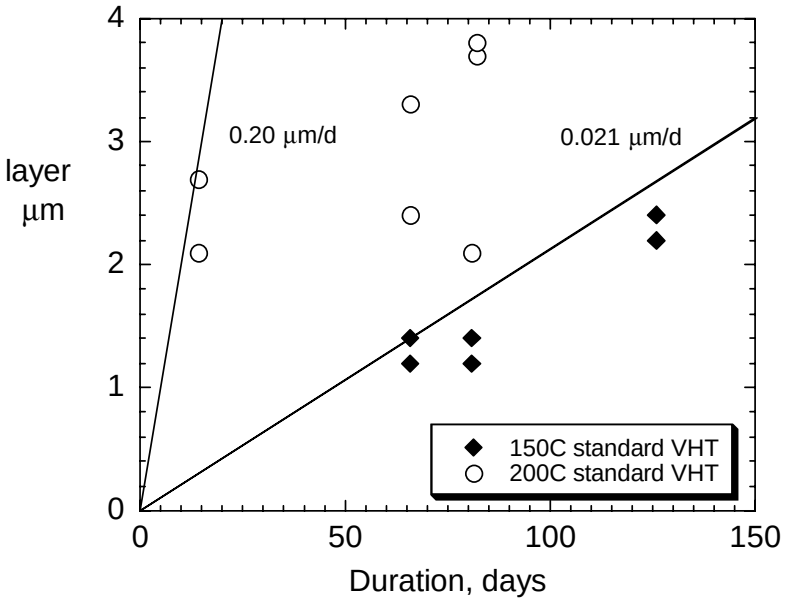

Fig. 4-4. Measured Layer Thicknesses for Samples from Standard VHTs Conducted at 150 and 200ºC. Lines show upper limit degradation rate for each temperature.

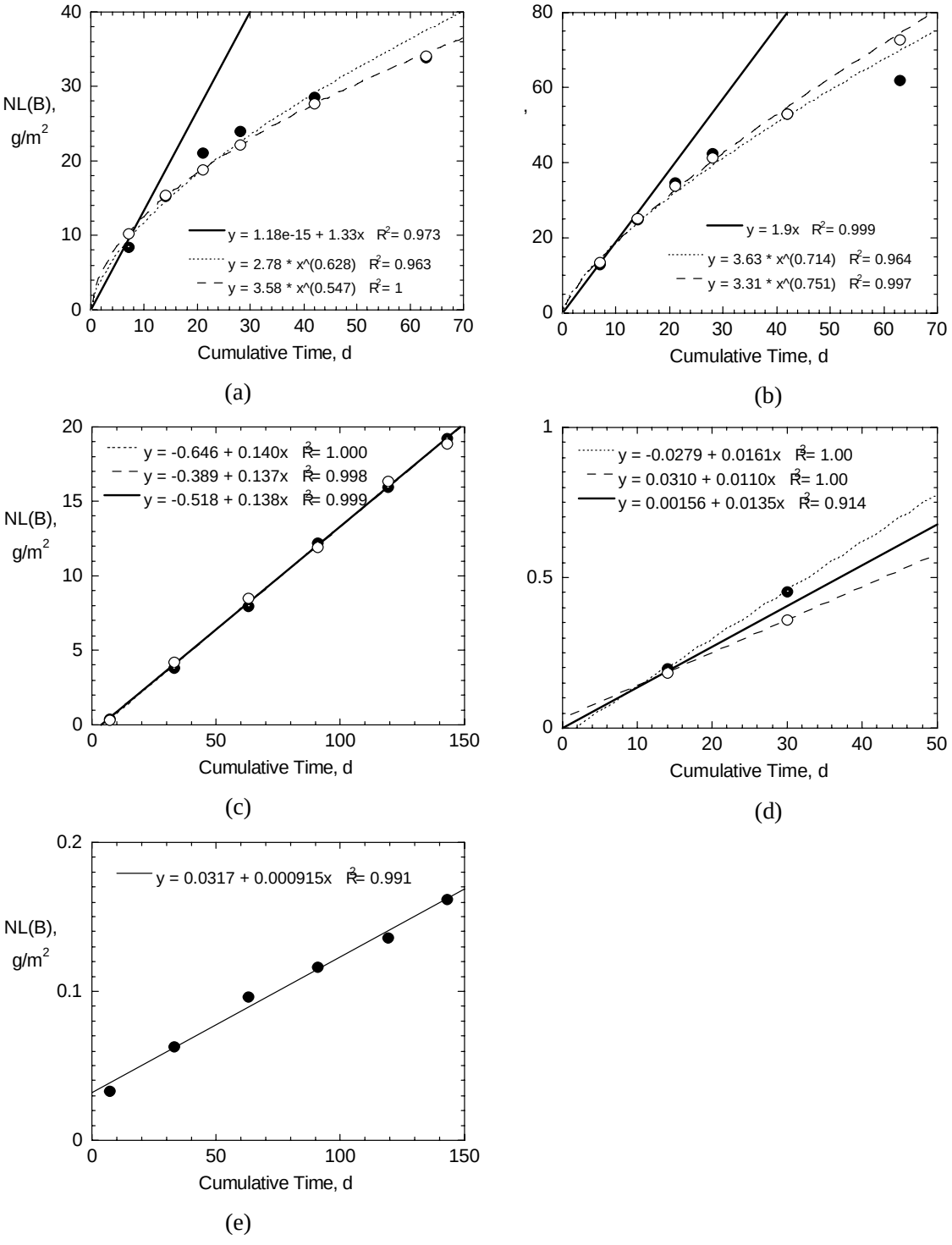

Fig. 4-5. Degradation of Hanford-H Glass in Excess-Water VHTs: NL(B) at (a) 200ºC, (b) 150ºC, (c) 90ºC, (d) 70ºC, and (e) 40ºC. Equations give linear rates for tests at 150 and 200ºC through 7 days for averages of duplicate tests (solid lines) and power law fits for each test (dashed and dotted lines). Equations for tests at 90, 70, and 40ºC give linear rates fit to all durations (solid lines give the average rates for the duplicate tests at 70 and 90ºC, dashed and dotted lines for fits to individual tests).

4.4 DISCUSSION

4.4.1. Consistency of MCC-1 Tests with SRL 202G Glass with pH and Temperature Dependencies in Defense HLW Glass Degradation Model

The consistency of these test results with the Defense HLW glass degradation model is not determined using Equation 4-1 because the values of k_E used in the model include solution feedback effects that are purposefully minimized in these tests. Instead, the test results are compared with the results of tests at 70 and 90ºC that were used to determine the model parameters for the pH and temperature dependencies. First, the rates measured in tests at 70 and 90ºC were extrapolated to 40ºC using the model parameters in the Defense HLW glass degradation model to determine if the 40ºC test results are consistent with the modeled rates. This was done as follows. The equations of the lines that were fit to the rates measured in tests at 70 and 90ºC in the model (BSC 2004, Section 6.5.4.1, Equations 14a-14d) are given in Equations 4-9a - 4-9d, where the term "pH" is the pH value measured at room temperature.

70ºC acidic leg:	$\log_{10} \text{rate}_G = 2.34 - 0.49 \times \text{pH}$	(4-9a)
90ºC acidic leg:	$\log_{10} \text{rate}_G = 2.60 - 0.49 \times \text{pH}$	(4-9b)
70ºC alkaline leg:	$\log_{10} \text{rate}_G = -5.12 + 0.49 \times \text{pH}$	(4-9c)
90ºC alkaline leg:	$\log_{10} \text{rate}_G = -4.54 + 0.49 \times \text{pH}$	(4-9d)

The dependence of the rate on the temperature is contained in the constant term in each equation (i.e., the first terms on the right-hand side of each equation). For the Defense HLW glass degradation model, the ratio of the rates calculated with Equations 4-9a and 4-9b at the same pH were used to determine the temperature dependence of the acidic leg. The rates calculated at pH 0 were used to determine the value of E_a =31 kJ/mol for the acidic leg. Similarly, the value of E_a for the alkaline leg was calculated to be 69 kJ/mol using the rates calculated with Equations 4-9c and 4-9d at pH 14. To extrapolate the rate expression to 40ºC, Equation 4-3 can be rearranged as shown in Equations 4-10a and 4-10b.

$$\frac{rate_2}{rate_1} = \exp\left[\frac{E_a}{R}\left(\frac{1}{T_1} - \frac{1}{T_2}\right)\right] \tag{4-10a}$$

$$rate_2 = rate_1 \bullet \exp\left[\frac{E_a}{R}\left(\frac{1}{T_1} - \frac{1}{T_2}\right)\right] \tag{4-10b}$$

For the acidic leg, rate_2 is the rate at 40ºC and pH 0 and E_a = 31 kJ/mol. For the alkaline leg, rate_2 is the rate at 40ºC and pH 14 and E_a = 69 kJ/mol. The rates at 90ºC at pH 0 and 14 are used as rate_1 for the acidic and alkaline legs, respectively. From Equation 4-9b, the value of $\log_{10}$ rate at 90ºC pH 0 is 2.60; the rate is 398 g/(m^2d). Substituting the values rate_1 = 398 g/(m^2d), E_a = 31 kJ/mol, T_1 = 363 K, T_2 = 313 K, and R = 0.008314 kJ/(mol•K) into Equation 4-10b gives:

$$rate_{40°C\ acidic} = 398 \bullet \exp\left[\frac{31}{0.008314}\left(\frac{1}{363} - \frac{1}{313}\right)\right] = 77.1\ g/(m^2 d) \tag{4-11a}$$

The rate at 40ºC and pH 0 for the acidic leg is 77.1 g/(m^2d); $\log_{10}$ rate = 1.887. Similarly, from Equation 4-9d, the value of $\log_{10}$ rate at 90ºC and pH 14 is 2.32; the rate is 209 g/(m^2d). For the alkaline leg, substituting the values $rate_1$ = 209 g/(m^2d), E_a = 69 kJ/mol, T_1 = 363 K, T_2 = 313 K, and R = 0.008314 kJ/(mol•K) into Equation 4-10b gives:

$$rate_{40°C\ alkaline} = 209 \bullet \exp\left[\frac{69}{0.008314}\left(\frac{1}{363} - \frac{1}{313}\right)\right] = 5.42\ g/(m^2 d) \qquad (4\text{-}11b)$$

The rate at 40ºC and pH 14 for the alkaline leg is 5.42 g/(m^2d); $\log_{10}$ rate = 0.734 g/(m^2d). In the Defense HLW glass degradation model, the same pH dependence is used for all temperatures. Model equations for the pH dependence at 40ºC having the same form as the expressions in Equation 4-9 were determined from the rates calculated in Equations 4-11a and 4-11b and the pH dependencies used in the model. The equation for the acidic leg at 40ºC having a slope of -0.49 and a log $rate_G$ of 1.887 at pH 0 from the model is:

$$\text{40ºC acidic leg:} \qquad \log rate_G = 1.887 - 0.49 \times pH \qquad (4\text{-}12a)$$

The equation for the alkaline leg at 40ºC with a slope of 0.49 and a log $rate_G$ of 0.734 at pH 14 is:

$$\text{40ºC alkaline leg:} \qquad \log rate_G = -6.126 + 0.49 \times pH \qquad (4\text{-}12b)$$

Equations 4-12a and 4-12b give the equations for the rates for the acidic and alkaline legs at 40ºC extrapolated from the Defense HLW glass degradation model appropriately compared with the MCC-1 test results. Figure 4-6a shows a composite plot of the rates measured in MCC-1 tests at 40, 70, and 90ºC (symbols) and the model rates based on regression to data at 70 and 90ºC (the lines for Equations 4-9a – 4-9d) and extrapolated to 40ºC (the lines for Equations 4-12a and 4-12b). For clarity, lines showing the model rates are plotted only above where they intersect.

We emphasize that these lines differ from the model rate because the effect of k_E on the rate is neglected. Figure 4-6a represents the dissolution rates in the absence of solution feedback effects. The effects of solution feedback will shift the lines to lower rates, but will not change the slope or the relative differences in rates at different temperatures.

Figure 4-6a shows that the rates determined from tests at 40ºC (square symbols) are consistent with the forward model rates (dotted lines) for both the acidic and alkaline legs. They are consistent with the V-shaped pH dependence of tests conducted at higher temperatures, and the measured rates are similar to the forward model rates at most pH values. It must be emphasized that the rates measured at 40ºC were not used to determine the lines drawn to represent the model rates at 40ºC; those lines show extrapolation of the model to 40ºC. The scatter of the 40ºC test results about the model rates is similar to the scatter of the 70ºC and 90ºC results about the model rates at those temperatures, although the differences at lower rates appear to be larger than those at higher rates on the semi-log plot. For example, the rate measured at pH 11.98, which is 1.09 g/(m^2d), is only about 2 times the model rate of 0.55 g/(m^2d). The 40ºC

tests are consistent with the pH and temperature dependences used in the Defense HLW glass degradation model.

Instead of comparing the rates measured at 40ºC with the existing model coefficients, they can be used with the rates measured at 90ºC to determine "refined" activation energies for dissolution in acidic and alkaline solutions for comparison with the values used in the model. A line with slope -0.49 regressed to the rates measured at pH 3.7, pH 4.8, and pH 8.5 has the equation:

$$\text{Measured 40ºC acidic leg:} \qquad \log \text{rate}_G = 1.570 - 0.49 \times \text{pH} \tag{4-13a}$$

and a line of slope 0.49 regressed to the rates measured at pH 8.5, pH 9.3, and pH 12 has the equation:

$$\text{Measured 40ºC alkaline leg:} \qquad \log \text{rate}_G = -6.245 + 0.49 \times \text{pH} \tag{4-13b}$$

(The rate measured at pH 8.5 is near the minimum of the V and used for both legs.) The rate calculated with Equation 4-13a at pH 0 is log rate_G = 1.570; rate = 37.15 g/(m^2d). Substituting this rate into Equation 4-3, along with the rate of 398 g/(m^2d) at 90ºC gives:

$$E_a = \frac{\ln\left(\frac{398}{37.15}\right) \bullet 0.008314}{\frac{1}{313} - \frac{1}{363}} = 44.78\, kJ/mol \tag{4-14a}$$

The rate calculated with Equations 4-13b at pH 14 is log rate_G = 0.6200; rate = 4.169 g/(m^2d). Substituting this rate into Equation 4-3, along with the rate of 209 g/(m^2d) at 90ºC gives:

$$E_a = \frac{\ln\left(\frac{209}{4.169}\right) \bullet 0.008314}{\frac{1}{313} - \frac{1}{363}} = 73.96\, kJ/mol \tag{4-14b}$$

Substituting these activation energies and the rates at 90ºC into Equation 4-10b to calculate rates at 70ºC gives 167.5 and 50.07 g/(m^2d) at pH 0 and pH 14, respectively. The corresponding rate expressions at 70ºC are:

$$\text{70ºC acidic leg:} \qquad \log \text{rate}_G = 2.224 - 0.49 \times \text{pH} \tag{4-15a}$$

and

$$\text{70ºC alkaline leg:} \qquad \log \text{rate}_G = -5.161 + 0.49 \times \text{pH} \tag{4-15b}$$

Figure 4-6b shows the test data and model rates at 40, 70, and 90ºC based on regression of the 40 and 90ºC results and interpolation at 70ºC.

4.4.2 Comparison of MCC-1 Test Results with Hanford-H Glass with pH and Temperature Dependence in Defense HLW Glass Degradation Model

It is not meaningful to compare the rates measured in these MCC-1 tests directly with the rates calculated with the HLW glass degradation model because the model takes into account solution feedback effects that are minimized by using the MCC-1 test method. Instead, the results are compared with the tests used to determine the model dependence temperature and pH. The results of tests with Hanford-H glass are compared with the model using the separate equations determined to model reaction in acidic and alkaline solutions. Since tests were conducted at only 1 pH value on the acidic leg and 1 pH value on the alkaline leg, the pH dependence for dissolution of Hanford-H glass cannot be determined from these test results. Any differences between the pH dependencies of Hanford-H glass dissolution and those used in the model will be convoluted with differences in the temperature dependencies. From the temperature dependence in the model, the ratio of rates at 40ºC and 90ºC can be calculated using Equation 4-10a with the appropriate value of E_a for acidic or alkaline solutions:

$$\frac{rate_2}{rate_1} = \exp\left[\frac{E_a}{R}\left(\frac{1}{T_1} - \frac{1}{T_2}\right)\right] \tag{4-10a}$$

Using the model values E_a = 31 kJ/mol for acidic solutions and E_a = 69 kJ/mol for alkaline solutions gives ratios of 5.16 and 38.6, respectively. The measured rates at pH 3.7 are 0.447 g/(m^2d) at 90ºC and 0.00712 g/(m^2d) at 40ºC, a ratio of $rate_{90}/rate_{40}$ = 62.8. This is about 12 times higher than the ratio from the model. The measured rates at pH 9.7 are 0.342 g/(m^2d) at 90ºC and 0.00441 g/(m^2d) at 40ºC, a ratio of 77.6, which is about 2 times higher than the ratio from the model. The activation energy can be estimated from the rates measured at two temperatures using Equation. 4-3:

$$E_a = \frac{\ln\left(\frac{rate_2}{rate_1}\right) \bullet R}{\left(\frac{1}{T_1} - \frac{1}{T_2}\right)} \tag{4-3}$$

Substituting the ratio of rates from tests at pH 3.7 into Equation 4-3 with T_1 = 313 K, T_2 = 363 K, and R = 0.008314 kJ/(mol•K) gives:

$$E_a = \frac{\ln(62.8) \bullet 0.008314}{\left(\frac{1}{313} - \frac{1}{363}\right)} = 78.2\, kJ/mol\,. \tag{4-16a}$$

Substituting the ratio of rates from tests at pH 9.7 into Equation 4-3 gives:

$$E_a = \frac{\ln(77.6) \bullet 0.008314}{\left(\frac{1}{313} - \frac{1}{363}\right)} = 82.2\, kJ / mol\,. \qquad (4\text{-}16b)$$

The activation energies calculated from the test results are both higher than the values used in the model, which are 31 and 69 kJ/mol for the acidic and alkaline legs, respectively. Note that direct comparison of the activation energies from Equations 4-16a and 4-16b with those used in the model presumes that the pH dependencies for Hanford-H glass are the same as those for SRL 202G glass, which has not been established.

4.4.3 Dissolution of Hanford-H Glass in Brine Solutions

The results of tests at 90ºC in the B7 and B4 leachants are compared with corresponding tests in the B7B and B4B leachants in Figures 4-7a and 4-7b to evaluate the effect of the added salt on the glass dissolution rate. The results from analysis with ICP-AES are plotted; these are non-Q results. In the acidic B7 leachants, the dissolution rate is lower in the leachant with added salt (dashed line). It should be noted that the difference is due to the result of the 10-day test without salt, which may be a high outlier but cannot be rejected. The results for shorter duration tests are indistinguishable within experimental uncertainty. The dissolution rates in the alkaline B4 leachants with and without added salt are very similar. These results indicate that the presence of dissolved salt has little impact on the glass dissolution rate. Note that the y-intercepts of lines fit to the results of tests in the B4 and B4 brine leachants differ by about 1 g/m^2. This may be due to differences in the solution pH values that are not completely taken into account by the pH adjustment method that was used.

4.4.4 Comparison of PCT Results with Defense HLW Glass Degradation Model

In development of the Defense HLW glass degradation model, values of k_E were determined by substituting the rate, pH, and temperature from 7-day PCT into Equation 4-1, which can be expressed in logarithmic terms as in Equation 4-8b and rearranged as:

$$\log k_E = \log rate - (\eta \bullet pH) + \left(\frac{E_a}{\ln 10\, RT}\right) \qquad (4\text{-}17a)$$

Because the PCT solutions were alkaline, the values of η and E_a for the alkaline leg were used to determine k_E for comparison with the range used in the model. The mean plus two standard deviations of values of k_E determined for several reference waste glasses was used as the maximum value for calculating the dissolution rate in alkaline solutions. The results of PCTs with Hanford-H glass can be compared with the model by substituting the values log rate = -1.01 and pH = 10.98 with the coefficients η = 0.49 and E_a = 69 kJ/mol, R = 0.008314 kJ/(mol•K), and T = 363 K into Equation 4-7:

$$\log k_E = -1.01 - (0.49 \bullet 10.98) + \left(\frac{69}{\ln 10 \bullet 0.008314 \bullet 363}\right) = 3.54 \qquad (4\text{-}17b)$$

k_E = 3.47 x 10^3 g/(m^2d). This is within the range of values log k_E = 3.574 ± 0.485 that was determined for reference waste glasses, and is well below the maximum value for alkaline solutions that is used in the model, which is log k_E = 4.54; k_E = 3.47 x 10^4 g/(m^2d). The mean rate calculated with the model (from Equation 4-2c) at 90ºC and pH 10.98 is 0.328 g/(m^2d), which bounds the rate of 0.0983 g/(m^2d) measured for Hanford-H glass.

4.4.5 Comparison of Excess-Water VHT Results with Temperature Dependence in Defense HLW Glass Degradation Model

Table 4-9 includes the maximum, minimum, and mean rates calculated with the model for the temperature and pH values attained in the tests using Equations 4-2a, 4-2b, and 4-2c. Glass dissolution is calculated by the model to be about 1.6 times faster at 200ºC than at 150ºC (for both the maximum and mean rates), but boron was measured to be released from Hanford-H glass about 2 times *faster at 150ºC than at 200ºC*. The rate is predicted to be about 26 times higher at 150ºC than at 90ºC, but the measured rate is only about 10 times higher at 150ºC than at 90ºC. The rate is predicted to be about 3.5 times higher at 90ºC than at 70ºC, but the measured rate is about 10 times faster at 90ºC than at 70ºC. The effects of temperature and pH are not sufficient to explain the differences in the measured rates. We hypothesize that this is because different chemical affinities result from the different reflux conditions in tests at different temperatures. Different values of k_E are needed to represent the solution conditions achieved in tests at different temperatures. From the relative rates discussed above, the degree of saturation of the solution condensed on the glass appears to increase with the test temperature: the measured rates are 26%, 75%, 11%, and 3% of the maximum rates. This implies that the effective value of k_E decreases as the temperature increases from 90ºC to 150ºC to 200ºC, and the effect of the affinity term moderates the accelerating effect of temperature. The greater than expected difference between the rates at 70 and 90ºC is probably due to a lower water vapor condensation rate at the low water vapor pressure at 70ºC.

Visual examination of the vapor-reacted samples revealed that few alteration phases had formed on the samples in the standard or excess-water VHTs. This suggests that the reaction did not progress to the point where the formation of alteration phases consumed silicic acid to cause an increase in the glass dissolution rate under either standard or excess-water conditions, at any temperature, or after any test duration. This is corroborated by the observation that the layers formed in the excess-water VHTs were significantly thicker than those formed in standard VHTs at the same temperature. This implies that the solutions generated on samples in excess-water VHTs were maintained more dilute than those generated in the standard VHTs. It is hypothesized that refluxing in the excess-water tests removed glass components from the surface film by dripping and continually diluted the solution on the glass as water vapor condensed in the film. The more dilute solutions maintained in the excess-water VHTs would provide less solution feedback than the solutions generated in the standard VHTs, and so provide less of a slowing effect on glass dissolution. In the standard VHTs, the slowing effect of solution feedback dominated the reactions. In the excess-water VHTs, the reflux diminished the effect of solution feedback at all temperatures, but more so at 70 and 90ºC than at 150 and 200ºC. Other test methods are needed to quantify the effects of reflux on the glass dissolution rate.

4.4.6 Summary of Test Results and Comparison with Defense HLW Glass Degradation Model

The dissolution rates measured for Hanford-H glass using various test methods are summarized in Table 4-9. The maximum, mean, and minimum rates calculated with the Defense HLW glass degradation model using Equations 4-2a, 4-2c, and 4-2b, respectively, at the same temperature and pH values are included in the table. The MCC-1 tests provide a measure of the rate in the absence of significant solution feedback effects. The Defense HLW glass degradation model excludes feedback effects for the acidic leg, but includes feedback effects for the alkaline leg. As part of the development of the model, dissolution rates were measured in alkaline solutions in the absence of solution feedback effects and a parameter value k_0 = 1.38 x 10^5 g/(m^2d) was determined to calculate the forward rate in alkaline solutions:

$$forward\ \ rate_{alkaline} = 1.38\times10^{5} \bullet 10^{0.49\bullet pH} \bullet \exp\left(\frac{-69}{0.008314\times T}\right) \qquad (4\text{-}19)$$

Equation 4-19 can be used to calculate the forward rates at pH 9.7 for comparison with the dissolution rates measured in MCC-1 tests with Hanford-H glass. The calculated rates at pH 9.7 are 0.0239 g/(m^2d) and 0.920 g/(m^2d) at 40 and 90ºC, respectively. These rates bound the rates measured for Hanford-H glass at pH 9.7. The model does not include feedback effects on the acidic leg, and comparison of the measured rates with the maximum rates calculated with the model (Equation 4-2a) is appropriate. The maximum model rates bound the rates measured for Hanford-H glass at pH 3.7 for both temperatures.

Both the maximum and mean rates calculated with the model (Equations 4-2a and 4-2c) at 90ºC and pH 10.98 (which is the measured pH) bound the rate measured in the PCT. The value of k_E extracted from the PCT results of Hanford-H glass is almost identical to the mean value determined from PCT with 9 reference glasses, which was used to establish the maximum rates calculated with the model. The minimum rate of the Defense HLW Glass Degradation Model for alkaline solutions was calibrated using the results of standard VHTs. The degradation rate in humid air at 90ºC was extrapolated from the results of tests at higher temperatures, because degradation was not detected at 90ºC by analysis of the alteration layer. The rate at 90ºC used in the model was 2.5 x 10^{-3} g/(m^2d). This is about 55 times lower than the rate measured in excess-water VHTs at 90ºC, which is 0.138 g/(m^2d). The feedback effects that slow dissolution in static films to very low rates under standard VHT conditions are overcome by refluxing in the excess-water VHTs.

The pH values of the solutions condensed on the glass samples in standard VHTs are assumed to be 12 at all temperatures (BSC 2004). The maximum, mean, and minimum rates calculated for degradation at 150ºC and pH 12 using the model are 79.3, 26.5, and 0.0645 g/(m^2d), respectively. The corresponding rates at 200ºC and pH 12 are 631, 211, and 0.513 g/(m^2d), respectively. The bounding rates measured with standard VHTs with Hanford-H glass are consistent with the minimum rates from the model, which were determined based on standard VHTs with other glasses. The rates based on the release of B in the excess-water VHTs represent an important water-contact scenario in the repository, namely, exposure to saturated water vapor. The rates measured in those tests are affected by the rates at which water vapor

condenses on the glass (via deliquescence), glass dissolves, and water drips off the glass. As summarized in Table 4-9, the maximum rates calculated with the Defense HLW glass degradation model bound the rates measured in both the standard and excess-water VHTs over a range of temperatures and pH values.

Comparison of the results of MCC-1 tests at pH 9.7, PCTs, and excess-water VHTs at 90ºC provides insight into the effects of the affinity term and reflux on the dissolution rates. The linearity of the MCC-1 test results (see Figure 4-2d) indicates that solution feedback remained negligible through the 10-day test period. Based on the lower dissolution rates, the solutions in excess-water VHTs and PCTs provided increasing levels of solution feedback. The effects of the small differences in the solution pH values can be deconvoluted from the measured rates using the pH dependence term in the model for alkaline solutions. The difference in the pH values in the excess-water VHTs and MCC-1 tests is 9.7 – 9.5 = 0.2 units, which has a modeled effect on the rate of $10^{0.49 \times 0.2} = 1.25$ times. Adjusting the rate measured in the excess-water VHT to pH 9.7 gives 1.25 x 0.138 = 0.173 g/(m^2d) for the excess-water VHT at 90ºC. The difference in the pH values in the PCTs and MCC-1 tests is 9.7 – 10.98 = -1.3 units, which has a factor of $10^{0.49 \times (-1.3)} = 0.231$ effect on the rate. Adjusting the rate measured in the PCTs to pH 9.7 gives 0.231 x 0.0983 = 0.0227 g/(m^2d). Dividing the rates for the PCTs and excess-water VHTs adjusted to pH 9.7 by the rate in the MCC-1 test provides an estimate of the values of k_E in those tests: $k_E = 0.0227 \pm 0.342 = 0.0664$ for the PCT and $k_E = 0.173 \pm 0.342 = 0.506$ for the excess-water VHTs. The difference in k_E reflects the lower chemical affinity in the PCT solutions, and indicates that the solutions on the samples in the excess-water VHTs were maintained more dilute than the PCT solutions by the reflux process. The relevance of the PCT solutions is that they were expected to be similar to those attained at long reaction progress under disposal conditions in model development. This indicates that besides providing an important pathway for the accumulation of water in a breached waste package at repository-relevant temperatures, deliquescence will allow dissolution to proceed at higher rates at repository-relevant temperatures and humidities. Further work is needed to quantify the relationship between the glass dissolution rate, temperature, RH, and water accumulation to develop a model for use in TSPA. The results of scoping tests conducted to address the importance of deliquescence are discussed in Section 5.0 of this report.

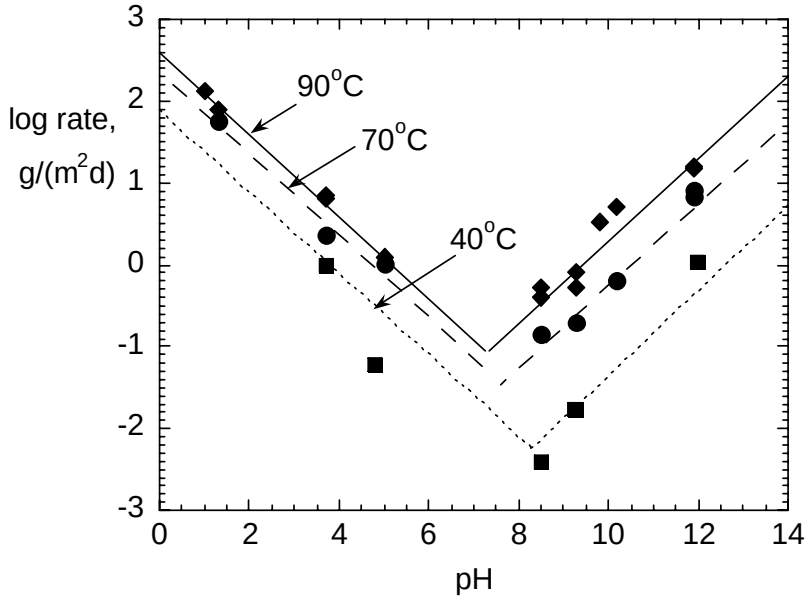

(a)

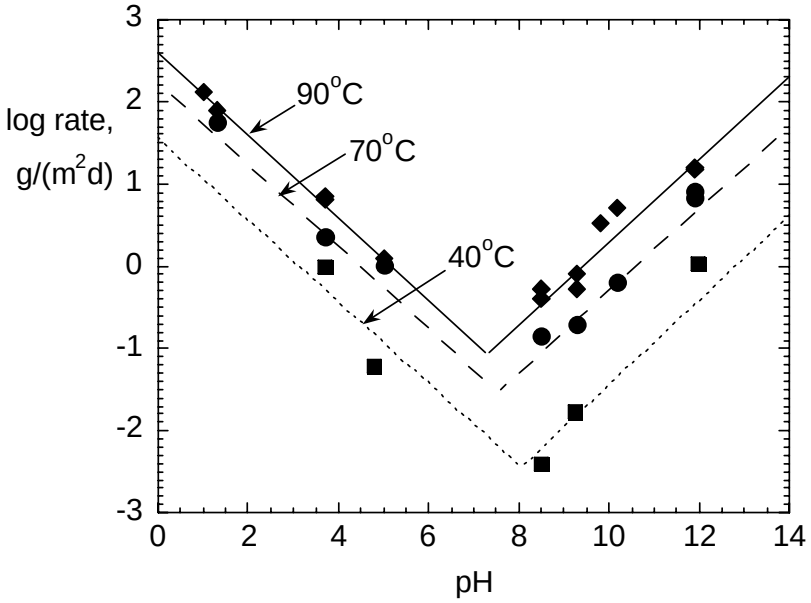

(b)

Fig. 4-6. Measured Rates for SRL 202G Glass vs. Modeled Rates Based on (a) Regression to 70 and 90ºC Results and Extrapolation to 40ºC and (b) Regression to 40 and 90ºC Results and Interpolation to 70ºC: Rates at 40ºC (■), 70ºC (●), and 90ºC (◆).

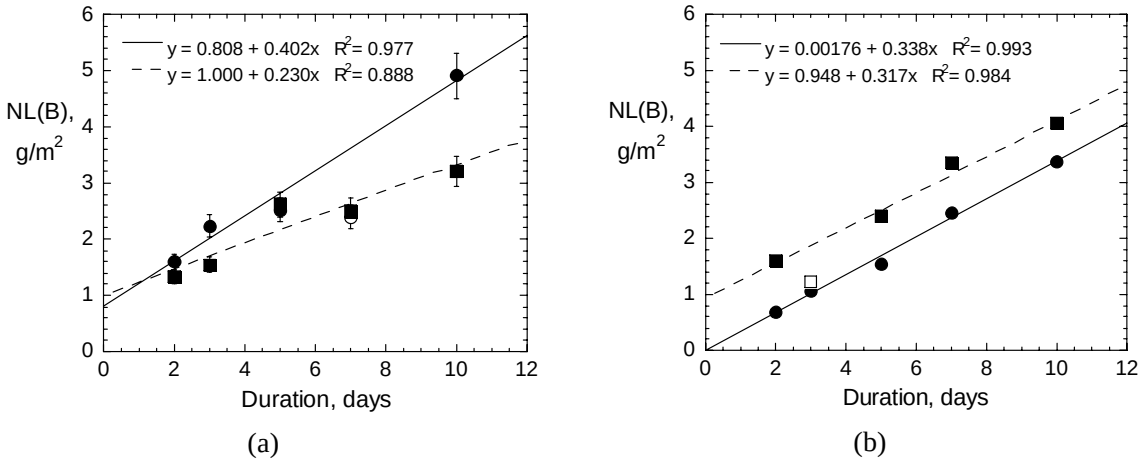

Fig. 4-7. Comparison of Tests in Leachants without Added Salt (● and solid lines) and with Added Salt (■ and dashed lines) at 90ºC and (a) pH 3.7 and (b) pH 9.7. Open symbols were excluded from regression. The non-Q ICP-AES results for test solutions with and without added salt are plotted.

4.5. REFERENCES

ASTM 2002a. *Standard Test Method for Static Leaching of Monolithic Waste Forms for Disposal of Radioactive Waste*. Annual Book of ASTM Standards, **12.01**, West Conshohocken, Pennsylvania: American Society for Testing and Materials.

ASTM 2002b. *Standard Test Methods for Determining Chemical Durability of Nuclear Waste Glasses: The Product Consistency Test (PCT)* Standard C1285-02, Annual Book of ASTM Standards, **12.01**, West Conshohocken, Pennsylvania: American Society for Testing and Materials.

BSC 2004. *Defense HLW Glass Degradation Model*. ANL-EBS-MD-000016, Rev. 01 ICN 01.

Ebert, W.L. (2003). "Data Report for MCC-1 Tests and PCTs with SRL 202G Glass." Memo from W.L. Ebert to File, July 24, 2003, with attachment. ACC: MOL.20030728.0214: MOL.20030728.0215.

Marples, J.A.C., Lutze, W., Kawanishi, M., and Van Iseghem, P. (1990). "A Comparison of the Behaviour of Vitrified HLW in Repositories in Salt, Clay and Granite: Part II: Results." *Scientific Basis for Nuclear Waste Management XIII, Symposium held November 27-30, 1989, Boston, Massachusetts*. (Edited by V.M. Oversby and P.W. Brown.) **176,** 275-282. Pittsburgh, Pennsylvania: Materials Research Society.

5.0 DELIQUESCENCE ASSOCIATED WITH GLASS CORROSION (W. Ebert)

5.1 BACKGROUND

Deliquescence is the process by which a solid takes up moisture from the atmosphere to form a solution. The driving force for deliquescence is the lowering of the chemical potential of water sorbed on a solid by the generation of a solution relative to vapor. The uptake of moisture from the atmosphere can occur due to the deliquescence of the glass itself and, more significantly, its corrosion products. The initial dealkalization reactions that occur when glass is contacted by water result in alkaline brine solutions that will absorb water from humid air as long as the vapor pressure of the atmosphere exceeds the equilibrium water vapor pressure of the solution. With the unlimited availability of moist air in the open repository design, deliquescence could result in the accumulation of enough water in a breached waste package to provide an advective flow of radionuclides out of the waste package under unsaturated conditions. Deliquescence will act to maintain a concentration gradient for vapor transport through breaches in the codisposal waste package containers, which will depend on the RH outside the package and deliquescence RH of the glass corrosion products. The scoping experiments described in this report are intended to evaluate the potential for water accumulation due to deliquescence and estimate the deliquescence relative humidities of various waste glass corrosion products. These data will aid in the design of subsequent experiments and calculations to quantify water condensation rates for various breach geometries that could occur over long disposal times.

The tests were conducted following the Test Plan for Defense HLW Glass Testing at Argonne National Laboratory (ANL) (ANL-TP-04-003, Rev. 00) under the Technical Work Plan for Waste Form Degradation Testing (TWP-WIS-MD-000008, Rev. 03). The tests were conducted under the ANL Quality Assurance Plan for Technical Activities in Support of the Yucca Mountain Project (YMP/G-3A-001, currently at Rev. 05). Data were compiled and analyzed using the Microsoft Office version XP of Microsoft EXCEL. Simple statistical computations (e.g., the calculation of mean values and standard deviations) were performed using the routines provided with EXCEL. Data plots were generated using KaleidaGraph software (Version 3.6, Abelbeck Software) and linear regression routines provided within that commercial software application. The transcriptions, calculations, plots, and regressions were checked by an independent technical reviewer.

5.2 PROCEDURES

5.2.1 Isopiestic Test Method

Isopiestic tests were conducted to measure the relative humidities at which water vapor will condense onto various vapor-hydrated surrogate HLW glasses, into solutions with dissolved glass components, and onto the salts generated by evaporating those solutions. (The evaporite solids are referred to as “evaporated salts” or “salts” in this report for convenience; the phase compositions of the salts were not analyzed.) The RH at which deliquescence first occurs is referred to as the deliquescent RH. The uptake (or loss) of water from reacted glasses, test solutions, and evaporated salts exposed to atmospheres with known water vapor pressures was

measured by the change in mass of containers with those specimens. Various fixed water vapor pressures were established using saturated salt solutions that generate known relative humidities. Test solutions, evaporated salts, and reacted glasses were sealed in containers with the saturated salt solutions for periods long enough to allow a measurable transfer of water between the saturated salt solution and the test materials. Although the term "isopiestic" refers to equilibration of the chemical potential of water in the vapor and solution phases, these tests were not allowed to proceed to equilibrium. Instead, they were conducted for a short duration to determine if vapor pressures of test materials were higher or lower than those of saturated salt solutions, which are known, to identify relative humidities at which the test materials did and did not take up water.

The isopiestic tests were conducted by placing the bottles bearing test solutions, evaporated salts, or vapor-hydrated glasses and a beaker with a saturated salt solution or demineralized water in a sealable plastic container. A test (or run) refers to exposing the test samples to the humidity generated by the saturated salt solution for a particular duration. Tests were conducted using commercially available plastic containers that were sealed using Viton O-rings and pinch clamps. (Polycarbonate vacuum test containers supplied by Bel-Art were used as containers for all isopiestic tests.) The mass of each test material was measured before and after exposure to the humidity generated by the salt solution to determine the mass change. The change in mass of the beaker with the salt solution was also determined. The mass changes indicated how much water was transferred between the test samples and the saturated salt solutions and whether the vapor pressure of the test material was higher (if water was lost) or lower (if water was gained) than that of the saturated salt solution. The masses of the loaded test containers were also measured before and after each exposure to detect any gross loss (or gain) of water vapor. Most of the tests were conducted in an incubator oven with air convection. The air temperature in the incubator was measured with a NIST-traceable thermometer.

Demineralized water was used to provide a RH of 100% and saturated salt solutions were used to provide lower relative humidities. The saturated salt solutions were made by adding reagent-grade NH_4Cl, NaCl, KCl, or KNO_3 to demineralized water in excess of their known solubilities so that undissolved salt was visible in the beaker. This ensured that the solutions remained saturated even after they took up water from the test samples. The relative humidities of these saturated salt solutions are known at several temperatures (Greenspan 1977). The relative humidities at the initial and final temperatures for each test series were calculated using the regressed equations, and the average of the calculated values was used as the RH for those tests. The regressed equations are:

KNO_3: $\%RH = 96.3 + 0.0106\,t - 0.00483\,t^2 + 2.67E\text{-}5\,t^3 \quad (R^2 = 1.00)$ (5-1a)

KCl: $\%RH = 88.6 - 0.195\,t - 0.000929\,t^2 \quad (R^2 = 1.00)$ (5-1b)

NH_4Cl: $\%RH = 82.0 - 0.148\,t + 0.000799\,t^2\ 1\ 1.33E\text{-}5\,t^3 \quad (R^2 = 1.00)$ (5-1c)

NaCl: $\%RH = 75.6 + 0.0283\,t - 0.0283\,t^2 + 2.67E\text{-}5\,t^3 \quad (R^2 = 0998)$ (5-1d)

where t is the temperature in ºC, and R^2 gives the square of the regression coefficient. These equations were used to calculate the RH at measured test temperatures.

5.2.2 Test Specimens

Isopiestic tests were conducted with several glasses under various test conditions to generate solutions having a range of chemistries and glass corrosion products. The glasses included Environmental Assessment (EA) glass provided by the Savannah River Technology Center, West Valley Reference Glass 6 (WV ref 6) provided by The Catholic University of America, and SRL 202U, SRL 131U, and Hanford-H glasses made at ANL. These glasses had been obtained or prepared for use in previous tests conducted at ANL. Solutions of dissolved glass were generated using the product consistency test (PCT) method, in which crushed glass was immersed in demineralized water. The glass reacted to generate fairly concentrated solutions under the PCT conditions. Different glasses and different glass/water ratios were used to generate a range of solution chemistries. For completeness, the solution concentrations of key glass components were measured with inductively coupled plasma mass spectrometry (ICP-MS) and the solution pH was measured with a combination electrode. However, these data are not part of the isopiestic test results and are not used in calculations. Aliquots of some PCT solutions were transferred to four bottles for use in separate isopiestic tests, which are designated using the test number with a suffix A, B, C, and D. This allowed the various test solutions to be exposed to four different humidities in parallel tests.

Samples of corroded glass were generated using the standard VHT method, in which monolithic samples were reacted in water vapor at elevated temperatures. The VHTs were conducted with one monolithic sample of SRL 202U glass and SRL 131U glass in each test vessel. These are designated using the letter B for SRL 202U glass and P for SRL 131U glass followed by the VHT test number. Tests with vapor-hydrated SRL 202U and SRL 131U glass were conducted because these samples provided more corrosion products than the vapor-hydrated Hanford-H glass samples. All of the monolithic samples were about 1 cm in diameter and about 1 mm thick and had a surface area of about 1.9 cm^2. The matrix of PCTs and VHTs used to generate solutions and specimens for isopiestic tests is given in Table 5-1. The samples used in isopiestic tests are identified by the tests in which they were generated. Alteration layers of clay and precipitated mineral phases formed on all VHT samples.

Three other glass samples were used in isopiestic tests. Sample H59 is Hanford-H glass that was vapor-hydrated at 150ºC for 161 days without any visible alteration. Samples of Hanford-H glass and SRL 202U glass that were previously prepared for VHTs but retained as archives were also tested. These samples were used as test controls to compare the deliquescence of the glass itself with that of its corrosion products. Since a measurable mass change was not expected in tests with the unreacted glass, the tests provided a measure of the precision of the mass determination.

The initial series of isopiestic tests was conducted with the PCT solutions contained in 30 mL solution bottles. These bottles have a 21-mm diameter opening and are about 58 mm deep. The geometry of the bottle probably limited the water accumulation rates in all tests, but allowed direct comparison of tests conducted with different solutions and at different relative humidities

because all the bottles had the same geometry. The bottle masses were measured to the nearest 0.01 g prior to receiving the test solutions, and isopiestic tests with the PCT solutions were measured to the nearest 0.01 g.

The test solutions were subsequently evaporated to dryness, and isopiestic tests were conducted with the evaporated salts. The solutions were evaporated by placing the uncapped solution bottles in a 90ºC oven for several hours until the salts were visibly dry. The same samples were used in several isopiestic tests at different relative humidities and dried again after each test. As results below will indicate, most samples were dried to slightly different masses between tests. However, the differences in starting mass are negligible relative to the water uptake in most cases. The results of tests with the evaporated salts are compared on a per dry mass salt per day basis.

All of the vapor-hydrated samples were visibly corroded with a similar abundance of precipitated mineral phases overlying a clay alteration layer on all samples. The Teflon thread was clipped to remove the samples from the steel rod after the VHT was completed. The Teflon thread around the sample was left intact to avoid disturbing the alteration phases. The vapor-hydrated and unreacted glass samples were placed in separate tared plastic cups for isopiestic testing. The cups had an opening of about 1 inch on the top and were about 0.7 inches deep. Control tests were conducted using unreacted Hanford-H glass (with a Teflon thread) and unreacted SRL 202U glass (without a Teflon thread).

5.3 RESULTS

5.3.1 Results of Isopiestic Tests with PCT Solutions

The compositions of the PCT solutions generated for use in isopiestic tests are given in Table 5-2. Several isopiestic tests were conducted with the solutions from PCTs Pdel-EA-1 and Pdel-WV6. The first tests (Run I) were conducted with the test solutions in separate test containers with saturated KCl solutions (RH = 83.4% at 25ºC). Water was lost from the PCT solutions and gained by the KCl solutions in both tests. This indicates that the vapor pressures of both PCT solutions are greater than 83.4%. Subsequent tests (Run II) were conducted with the same PCT solutions and saturated KNO_3 solutions (RH = 93.6% at 25ºC). (Small amounts of demineralized water were added to the PCT solutions between runs I and IIa and runs IIb and III to replace the water that had been transferred during the previous run.) Water was transferred from the PCT solution to the KNO_3 solution in both tests, which indicated the vapor pressures of both PCT solutions were greater than 93.6%. However, the transfer rate to the saturated KNO_3 solution was about half of that measured for transfer to the KCl solution. A difference in water-transfer rates is expected since the difference in vapor pressures between the PCT and saturated KCl solutions is greater than that between the PCT and saturated KNO_3 solutions. The PCT solutions were exposed to the KNO_3 solutions for an additional 7 days in Run IIb. The transfer rates from the PCT solutions to the KNO_3 solutions were essentially the same as for the first exposure, which indicated the tests were repeatable and none of the solutions had vapor pressures near that of the saturated salt solution. It may be significant that the rate of loss from Pdel-WV6 is about 2 times higher than from Pdel-EA-1 for Runs I, IIa, and IIb. This suggests

that the vapor pressure of Pdel-WV6 is higher than that of Pdel-EA-1, which is expected based on the solution chemistries.

A third test (Run III) with the Pdel-EA-1 and Pdel-WV6 solutions was conducted with demineralized water. These tests showed loss of water from both the PCT solutions and the demineralized water sources due to leakage from the desiccator. Although this renders these tests unquantitative, the observation that the losses from both PCT solutions and demineralized water were similar suggests they have similar vapor pressures.

Aliquots of the other PCT solutions were transferred to separate bottles for isopiestic tests with KCl (Run IV) and KNO_3 (Run IV). For each run, 6 PCT solutions were simultaneously exposed to the RH fixed by the saturated salt solution in each of two test containers. Water was lost by all PCT solutions, and more water was lost in tests with KCl (83.4% RH) than in tests with KNO_3 (93.6% RH). A small amount of water was also lost from the KNO_3 solution, probably when the container was being weighed. All containers were left uncovered while solution bottles were weighed, and measurable amounts of the saturated solutions of KCl, KNO_3 and demineralized water evaporated while being weighed. The total loss from the PCT solutions in Run IV was 1.49 g, which is in good agreement with the sum of the masses gained by the KCl solution and the total mass lost from the test container (1.35 g and 0.25 g, respectively). The total loss from the PCT and KNO_3 solutions in Run V was 0.200 g, which is about the same as the total loss from the test container. In both Runs IV and V, similar amounts of water were lost by all PCT solutions.

The results as mass loss per mass starting solution per day are summarized in Table 5-3 and plotted in Figure 5-1. The water loss is normalized to the starting mass because the vapor pressure depends on the solution composition. The rates of water loss do not appear to be correlated with the amounts of dissolved solids in the different solutions, except significantly more water was lost from the WV6 solution than from the other solutions. The WV6 solution was the least concentrated of the solutions that were tested (see Table 5-2).

5.3.2 Results of Isopiestic Tests with Evaporated PCT Salts

Several isopiestic tests were conducted with the residual salts produced by evaporating the PCT solutions from tests with SRL 202U, Hanford-H, and EA glass. Isopiestic tests were conducted with several evaporated salt and vapor-reacted glass samples in each test container with a saturated salt solution. Four tests were conducted simultaneously in separate test containers, each with a different saturated salt solution. Demineralized water was placed in each test container for the last run. The evaporated salts and vapor-reacted glasses were dried for several hours in a 90ºC oven between runs and reweighed. The test containers were placed in an incubator with air circulation for the entire test duration. The air temperature in the incubator was measured immediately prior to placing the test containers in the incubator and immediately before removing the test containers with a NIST-traceable thermometer that was left in the incubator throughout the test period. Results for tests with the vapor-reacted glasses and unreacted control tests are discussed separately in the next section. For each run, the RH fixed by each saturated salt solution at the initial and final temperatures was calculated using Equations5-1a through 5-1d, and the average was used as the RH for that run. The water uptake

rates are summarized in Table 5-4 and plotted in Figures 5-2a through 5-2d for the four runs. The uptake rates for all samples increased with the RH. Note that the results of tests with the $MgCl_2$ are included in Figure 5-2d for completeness, although the RH of those tests is not known because the solution was not saturated during the test. Figure 5-2e shows the compiled uptake rates for the evaporated salts from different PCTs for aliquots A, B, C, and D. The average uptake rates are plotted in cases of replicate measurements at a particular RH. The reproducibilities of the replicate tests can be assessed by comparing Figures 5-2a through 5-2d. The uptake rates increase with the RH for the salts from PCTs with all glasses. Note that the differences in uptake rates at 78.6% RH and 100% RH were generally less than a factor of 10.

5.3.3 Results of Isopiestic Tests with Vapor-Hydrated Glasses

The VHTs Vdel-BP-2 (samples B2 and P2) and Vdel-BP -4 (samples B4 and P4) were terminated after 15 days. VHTs Vdel-BP-1 (samples B1 and P1) and Vdel-BP-3 (samples B3 and P3) were terminated after 20 days. Visual inspection of the reacted samples indicated that all were covered with a clay alteration layer that was overlain with precipitated mineral phases. The alteration and abundance of precipitated phases were not quantified, but appeared to be similar for all samples and similar to those identified in previous tests, including analicme, gyrolite, and weeksite (Ebert and Bates 1993). One or more vapor-hydrated glass samples were included in the isopiestic tests with the PCT solutions or evaporated salts. Drying the vapor-hydrated samples at 90ºC caused some of the alteration phases to spall from the samples. These were left in the sample cup for subsequent isopiestic tests. This may have resulted in a small increase in the surface area of alteration phases for each subsequent run. The rates of water uptake in tests with the different samples are summarized in Table 5-5 and plotted in Figure 5-3. Not all samples were exposed to all relative humidities. The mass of alteration phases formed on some samples was estimated by shaking the dried samples in the sample vials after the tests were completed to knock most of the layer off of the glass, then weighing the remaining glass core. The masses of alteration phases on samples B1, B2, P2, and P4 were estimated in this manner. The layers could not be knocked off of samples P1 or B4, and samples B3 and P3 were completely fragmented after the isopiestic tests (due to oven drying between tests). The mass of alteration phases was estimated by subtracting the mass of the glass core from the initial mass of the sample. The rates as g water/(g alteration phases•d) are given in parentheses in Table 5-5.

As was seen with the evaporated salt samples, the greatest water uptake occurs at 100% RH and decreases as the RH decreases. The uptake rates are similar for samples of vapor-hydrated SRL 202U and SRL 131U. The uptake rates on a per mass alteration phase per time basis was less than the uptake rates of the evaporated salts at the same RH, with the possible exception of tests at 75% RH, where the fractional uptake of some vapor-hydrated samples was higher than that of the evaporated salts. No uptake was detected on the vapor-hydrated Hanford-H glass (sample H59) or either sample of unreacted glass. This indicates the uptake on the other samples was by the alteration phases. It should be noted that water sorption is known to occur on unreacted waste glass (Ebert et al. 1991), but the amounts sorbed in these tests are below the detection limit. A more sensitive method is needed to study water sorption on unreacted glass than that employed in these tests. However, the readily measurable deliquescence of reacted glass at room temperature indicates the importance of this process in the repository.

Table 5-1. Matrix for Tests Used to Generate Test Samples for Isopiestic Tests

Test Number	Temperature, °C	Duration, Days	Glass	Glass/water, g/g	Isopiestic Test Sample Numbers
Product Consistency Tests Used for Isopiestic Test Samples					
Pdel-WV6	90	7	WV ref 6	1/10	Pdel-WV6
Pdel-EA	90	7	EA	1/10	Pdel-EA1
Pdel-202U-1	90	7	SRL 202U	1/10	Pdel-202U-1A, -1B, -1C, and -1D
Pdel-HanH-1	90	7	Hanford-H	1/10	Pdel-HanH-1A, -1B, -1C, and -1D
Pdel-EA-2	90	7	EA	1/10	Pdel-EA-2A, -2B, -2C, and -2D
Pdel-EA-3	90	7	EA	1/10	Pdel-EA-3A, -3B, -3C, and -3D
Pdel-EA-4	90	7	EA	2/10	Pdel-EA-4A, -4B, -4C, and -4D
Pdel-EA-5	90	7	EA	3/10	Pdel-EA-5A, -5B, -5C, and -5D
Standard Vapor Hydration Tests Used for Isopiestic Test Samples					
Vdel-BP-1	200	20	SRL 202U and SRL 131U	---	Vdel-B1 and Vdel-P1[a]
Vdel-BP-2	200	15	SRL 202U and SRL 131U	---	Vdel-B2 and Vdel-P2
Vdel-BP-3	200	20	SRL 202U and SRL 131U	---	Vdel-B3 and Vdel-P3
Vdel-BP-4	200	15	SRL 202U and SRL 131U	---	Vdel-B4 and Vdel-P4

Table 5-2. PCT Solutions Used in Isopiestic Tests

Sample Number	pH	Concentration, mg/L								
		Al	B	Ca	Fe	Li	Mg	Na	Si	Total
Pdel-EA-1	10.55	<1.5	783	1.58	0.969	198	<0.11	2240	130	3353
Pdel-WV6-1	12.42	5.36	16.5	0.461	5.03	6.8	0.389	23.1	36.5	94.3
Pdel-202U-1	10.05	3.17	10.4	0.996	3.00	9.31	<0.04	498	68.9	593.8
Pdel-HanH-1	10.37	<0.08	37.4	1.09	0.540	29.5	<0.04	484	121	673.5
Pdel-EA-2	10.86	<0.08	117	1.62	0.327	63.2	<0.04	1060	274	1516
Pdel-EA-3	11.41	<0.08	412	2.51	0.246	118	<0.04	1700	518	2751
Pdel-EA-4	11.40	<0.08	933	3.17	0.211	192	<0.04	2900	918	4946
Pdel-EA-5	11.39	0.198	1280	3.52	0.187	244	<0.04	3730	1090	6348

Table 5-3. Mass Changes of PCT Solutions, g Change/(g solution•d)

PCT Solution	83% RH	94% RH	100% RH
EA-1	-0.0154	-0.0073	-0.00849
WV6	-0.0361	-0.0172	-0.00868
202U-1	-0.0160	-0.0078	not measured
HanH-1	-0.0150	-0.0067	not measured
EA-2	-0.0130	-0.0061	not measured
EA-3	-0.0130	-0.0072	not measured
EA-4	-0.0120	-0.0077	not measured
EA-5	-0.0140	-0.0072	not measured

Table 5-4. Water Uptake by PCT Salts, g Water/(g salt/day)

Test Number	Relative Humidity				
		78.6% (Run VIII)	84.1% (Run VI)	93.2% (Run(VII)	100.0% (Run IX)
Pdel-202U-1A		0.2039	0.2264	0.4437	2.6442
Pdel-HanH-1A		0.1481	0.1882	0.3764	1.5471
Pdel-EA-2A		0.1667	0.2500	0.4097	1.1819
Pdel-EA-3A		0.1210	0.2135	0.8068	0.8561
Pdel-EA-4A		0.1117	0.2429	0.3343	0.6365
Pdel-EA-5A		0.1235	0.2685	0.3323	0.6258
	75.3% (Run VIII)		84.1% (Run VII)	93.2% (Run VI)	100.0% (Run IX)
Pdel-202U-1B	0.0169		0.2119	0.5105	2.7143
Pdel-HanH-1B	0.0160		0.1933	0.4465	2.1244
Pdel-EA-2B	0.0071		0.2265	0.5376	1.4995
Pdel-EA-3B	0.0091		0.1586	0.4109	1.5399
Pdel-EA-4B	0.0035		0.1607	0.3740	0.7084
Pdel-EA-5B	0.0026		0.1628	0.3693	0.6509
	75.2% (Run VI)	78.4% (Run VII)		93.5% (Run VIII)	100.0% (Run IX)
Pdel-202U-1C	0	0.1367		0.3838	2.3643
Pdel-HanH-1C	-0.0017	0.1143		0.3204	1.8000
Pdel-EA-2C	-0.0027	0.1258		0.2500	0.9970
Pdel-EA-3C	-0.0017	0.1141		0.1817	0.6370
Pdel-EA-4C	-0.0019	0.1407		0.2029	0.5949
Pdel-EA-5C	-0.0016	0.1519		0.2090	0.6064
	75.2% (Run VII)		84.3% (Run VIII)		100.0% (Run IX)
Pdel-202U-1D	0.0017		0.6772		2.7467
Pdel-HanH-1D	-0.0030		0.5522		2.0889
Pdel-EA-2D	-0.0019		0.4896		1.6761
Pdel-EA-3D	-0.0022		0.3668		1.0968
Pdel-EA-4D	-0.0041		0.3732		1.1407
Pdel-EA-5D	-0.0005		0.3731		1.1267

Table 5-5. Water Uptake by VHT Samples, g water/day[a]

Test Number	Relative Humidity				
	75.3%	78.6%	84.3%	93.2%	100.0%
Vdel sample B1		0.0013 (0.0212)		0.0030 (0.0482)	0.0145 (0.2365)
Vdel sample P1		0.0006		0.0017	0.0106
Vdel sample B2	0.0003 (0.0079)		0.0011 (0.0347)		
Vdel sample P2	0.0002 (0.0069)		0.0011 (0.0398)		
Vdel sample B3		0.0003		0.0020	0.0083
Vdel sample P3		0.0023		0.0060	0.0223
Vdel sample B4	0.0003		0.0016	0.0029	0.0108
Vdel sample P4	0.0002 (0.0053)		0.0012 (0.0391)		0.0075 (0.2523)

[a]Values in parentheses give rates as g water/(g alteration phases • d) based on the masses of alteration phases removed from the sample after isopiestic tests were completed.

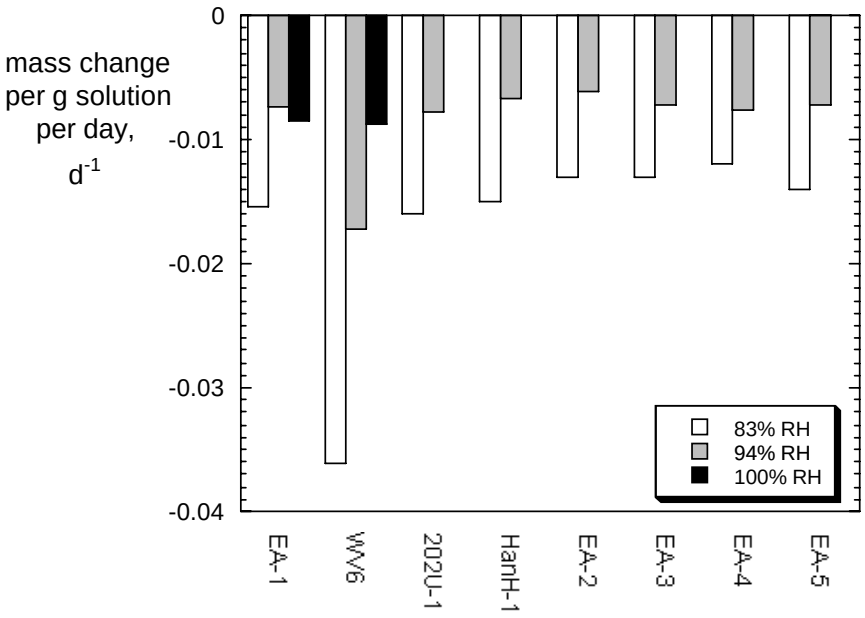

Fig. 5-1. Water Loss from PCT Solutions in Isopiestic Tests with Saturated Solutions of KCl (83% RH) and KNO_3 (94% RH) and with Demineralized Water (100% RH).

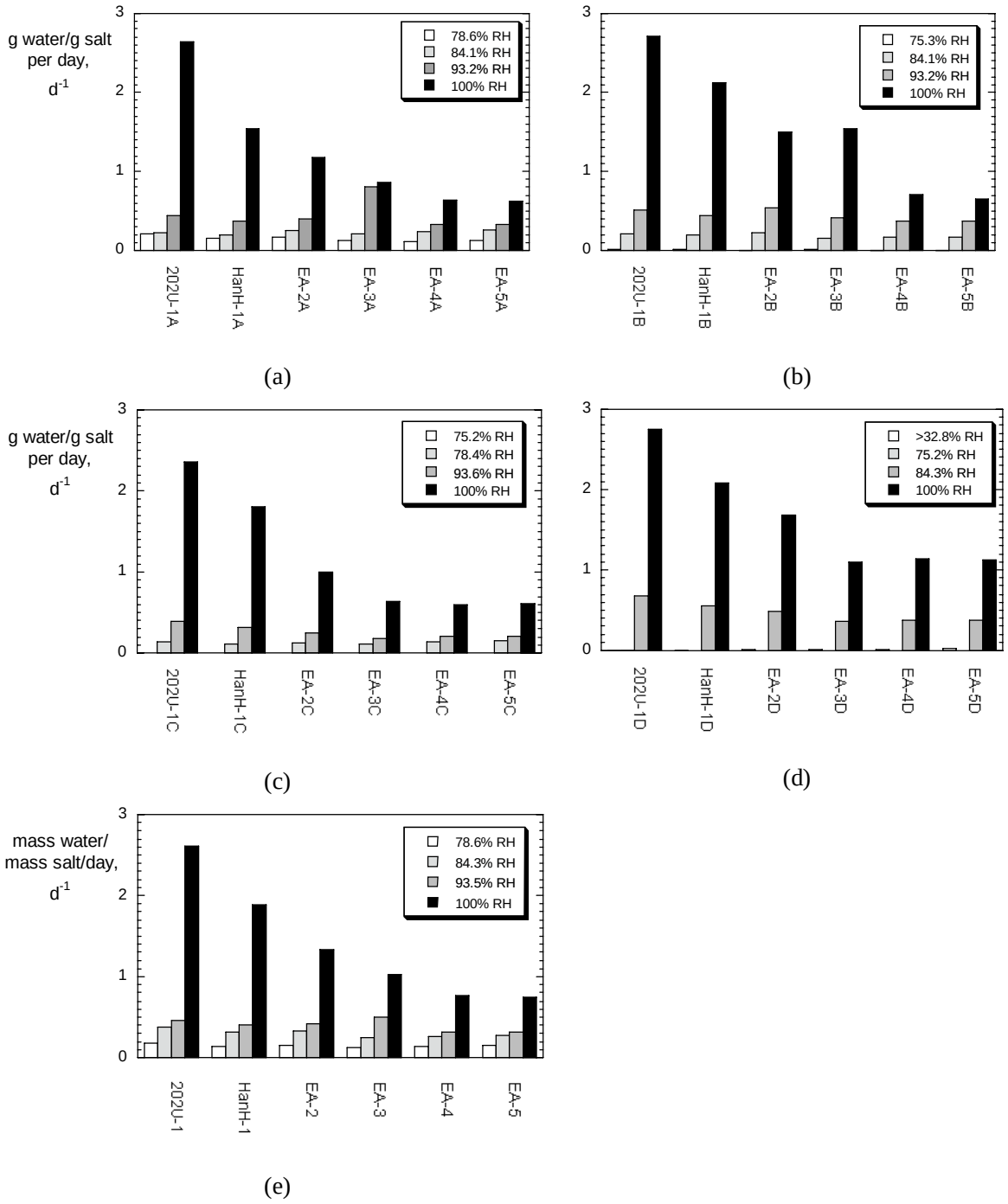

Fig. 5-2. Water Uptake Rates for Salts from Evaporated PCT Solutions at Various Humidities: (a) Series A, (b) Series B, (c) Series C, and (d) Series D, and (e) Average of Samples A, B, C, and D.

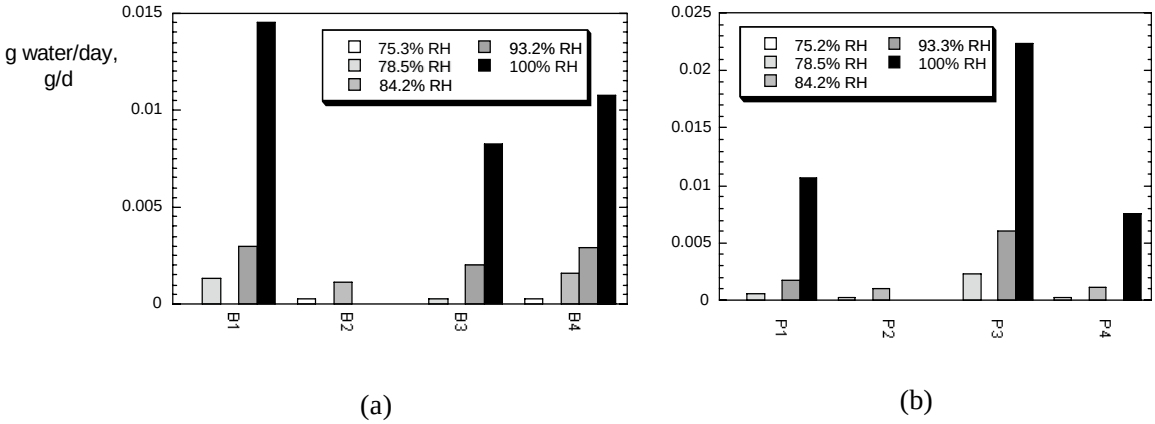

(a) (b)

Fig. 5-3. Water Uptake Rates for Vapor-Hydrated Glass at Various Relative Humidities for (a) SRL 202U Glass and (b) SRL 131U Glass.

5.4 DISCUSSION

The test samples studied for the initial isopiestic tests were selected to span the range of HLW glass deliquescence expected in the repository over long times. The PCT solutions represent the dilute solutions that could be generated when various HLW glasses corrode in condensed water vapor or seepage waters evaporate. The residual solids from evaporated PCT solutions simulate the soluble soils that will be generated as glass corrodes upon contact by water. The vapor-hydrated glass samples provide the assemblage of mineral phases that may eventually form on glass exposed to humid air. The isopiestic tests measure the potential of these solids to take up water from humid air. The salts that were formed by evaporating PCT solutions and the alteration phases that formed on vapor-hydrated glasses both took up water at relative humidities expected in the repository after long disposal times. Water uptake by these solids was detected within a few days at humidities above 78% RH using a fairly insensitive method. Water uptake probably also occurs at lower humidities, albeit more slowly. The average uptake rates for the evaporated salts were 1.4 d^{-1} at 100% RH, 0.38 d^{-1} at 93% RH, 0.30 d^{-1} at 84% RH, and 0.14 d^{-1} at 79% RH; the unit for the uptake rates is (g water)/(g salt•d). The average water uptake rates for the alteration phases on the vapor-hydrated samples were 0.24 d^{-1} at 100% RH, 0.048 d^{-1} at 93% RH, 0.038 d^{-1} at 84% RH, 0.021 d^{-1} at 79% RH, and 0.007 d^{-1} at 75% RH. While these were measured at about 25ºC, similar uptake rates are expected at higher temperatures, although this needs to be verified.

These results indicate that deliquescence may be an important process that will cause water to accumulate and perhaps contribute to radionuclide transport for codisposal waste packages exposed to humid air. Based on the results of isopiestic tests with the PCT solutions themselves, the water accumulation rate will decrease to a low value as the brine solution is diluted. This is consistent with the observation that the vapor pressures of simple salt solutions generally increase as the salt concentrations decrease (e.g., Pearce and Nelson 1932). Additional tests are needed to relate the water accumulation rate to the ionic strength of the solutions generated as HLW glasses dissolve.

5.5 REFERENCES

Ebert, W.L, Hoburg, R.F., and Bates, J.K. (1991). "The Sorption of Water on Obsidian and a Nuclear Waste Glass." *Physics and Chemistry of Glasses*, **32**(4), 133-137. Sheffield, England: Society of Glass Technology.

Ebert, W.L. and Bates, J.K. (1993). "A Comparison of Glass Reaction at High and Low Glass Surface/Solution Volume." *Nuclear Technology,* **104,** 372-384. Hinsdale, Illinois: American Nuclear Society.

Greenspan, L. (1977). "Humidity Fixed Points of Binary Saturated Aqueous Solutions." *Journal of Research of the National Bureau of Standards-A.* Physics and Chemistry **81A**(1) January-February 1977, 89-96.

Pearce, J.N., and Nelson, A.F. (1932). "The Vapor Pressures of Aqueous Solutions of Lithium Nitrate and the Activity Coefficients of Some Alkali Salts in Solutions of High Concentration at 25C." *Journal of the American Chemical Society*, **54**, 3544-3554.

ACKNOWLEGEMENTS

This research is funded by the U.S. Department of Energy (DOE), Office of Civilian Radioactive Waste Management, Yucca Mountain Program under contract number W-31-109-ENG-38. Use of the Advanced Photon Source was supported by the DOE's Office of Energy Research, Basic Energy Sciences. We also thank Dr. A. Jeremy Kropf for assistance with the XAS instrumentation.

Distribution for ANL-05/08

Internal (Printed and Electronic Copies):

J. C. Cunnane (12)
W. L. Ebert (5)
R. J. Finch
J. A. Fortner
J. L. Jerden
M. T. Peters
M. J. Steindler

Internal (Electronic Copy Only):

M. R. Hale, TIS
D. Lewis
D. J. Graziano
G. F. Vandegrift
M. C. Regalbuto
A. J. Bakel
D. B. Chamberlain
N. L. Dietz
M. M. Goldberg
M. Kaminski
C. J. Mertz
Y. Tsai
V. S. Sullivan
M. A. Williamson

External (Electronic Copies Only):
M. A. Buckley, ANL Library-E
P. A. Bernot, Bechtel SAIC Co.
N. C. Painter, Bechtel SAIC Co.
V. Pasupathi, Bechtel SAIC Co.
D. W. Thomas, Bechtel SAIC Co.

Chemical Engineering Division Review Committee Members:
H. U. Anderson, University of Missouri-Rolla, Rolla, MO
C. L. Hussey, University of Mississippi, Oxford, MS
M. V. Koch, University of Washington, Seattle, WA
V. P. Roan, Jr., University of Florida, Gainesville, FL
J. R. Selman, Illinois Institute of Technology, Chicago, IL
J. S. Tulenko, University of Florida, Gainesville, FL